# CZECH TECHNICAL UNIVERSITY IN PRAGUE

Faculty of Civil Engineering

Department of Materials Engineering and Chemistry

Habilitation thesis

2021

Ing. Václav Kočí, Ph.D.

# Correction of Systematic Errors of Calorimetric Measurements Using Computational Modelling

## Korekce systematických chyb kalorimetrických měření prostřednictvím počítačového modelování

# Acknowledgments:

I would like to thank my colleagues who have given me valuable comments, suggestions and advices during writing this thesis. My deepest gratitude is expressed especially to Prof. Robert Černý and Assoc. Prof. Jiří Maděra for their support.

I would like to acknowledge the financial support provided by the Czech Science Foundation grants No. P105/12/G059, 17-01365S and 18-03997S.

Last but not the least, I would like to thank my family – Lucie and Matěj – for their patience and time spent on writing instead of being together.

## Abstract:

The habilitation thesis deals with a utilization of computational modelling for an elimination of systematic errors that accompany calorimetric measurements. An isothermal heat flow calorimeter (IC) and a differential scanning calorimeter (DSC) are selected for the investigations, suffering with thermal inertia and a signal delay that together affect the experimental outputs.

Computational models of both devices are constructed at first, being calibrated following principles of experimental calibration procedures for the particular devices. The validation of the IC model performed on an independent heating scheme shows a very good agreement, yielding $R^2 = 0.9998$. The validation of the DSC model is performed on an aluminum standard undergoing a melting process while a maximum difference at the peak top less than 0.297 $\mathrm{mW \cdot mg^{-1}}$ is found when compared to experimental data. Subsequently, $\alpha$-$\beta$ quartz transition is modelled, revealing a good agreement with both the measured data and the results of independent experiments reported by several other investigators. Both models can be therefore considered to be able to separate or quantify particular heat evolving/consuming mechanisms in both devices-materials systems. Therefore, contrary to the empirical calibrations, they can identify exactly the physical sources of measurement uncertainties. The raw experimental data provided by the calorimeters can be then corrected in a straightforward way and the systematic errors can be eliminated.

The capabilities of the IC model are demonstrated for the heat evolution in lime hydrate-water- and Portland cement-water systems, where the computational assessment makes it possible to reconstruct heat absorbed by the calorimeter in the early-age of hydration. The corrected hydration heat power peaks, being extracted from the samples directly, then reach seven to twelve times higher values than the experimental measurements. The high level of agreement of the original experimental data with its computational representation, $R^2 = 0.9984$ for the lime hydrate-water system and $R^2 = 0.9992$ for the Portland cement-water system, confirms an overall good accuracy of the model.

An influence of sample mass and heating rate on results provided by the DSC is corrected by means of a detailed modeling of thermal phenomena in the calorimeter-sample system using the DSC model. It is able to extract pure data related to the sample itself that is free of distortions. In a practical application of the model, lime hydrate samples of various mass are analyzed at first experimentally while several different heating rates are used, and the influence of varying parameters on the obtained outputs is recorded. The experimental data are then reconstructed using computational modeling of thermal phenomena in the calorimeter-sample system. The corrected specific heat power values are found to be up to 9% higher and can be attributed to the heat capacity of inner parts of the device that consume a part of the heat. The highest agreement between experimental and computational outputs is achieved when a sample filling one half of the crucible’s volume is heated at 7 $\mathrm{K\cdot min^{-1}}$. Such a parameter choice shows a low temperature shift (<5 °C) and the specific heat power difference is only 0.09 $\mathrm{mW\cdot mg^{-1}}$ (3.4 %).

Generally, the capability of the developed computational method to correct intrinsic distortions, which are characteristic for specific calorimetric techniques, such as the heat consumption by device components and signal delay, makes good prerequisites for its further applications in physics, chemistry, and engineering.

**Keywords:** *calorimetric measurements, computational modelling, systematic errors, thermal inertia, signal delay.*

## Anotace:

Habilitační práce se zabývá využitím počítačového modelování pro odstranění systematických chyb kalorimetrických měření. V práci jsou analyzovány vybrané druhy zařízení, jmenovitě izotermální kalorimetr (IC) a diferenční skenovací kalorimetr (DSC), vyznačující se jistou mírou tepelné setrvačnosti, která vede ke zkreslení naměřených výsledků v důsledku zpoždění výstupního signálu.

V první fázi práce jsou vytvořeny modely obou kalorimetrů, které jsou následně zkalibrovány dle postupů shodných s experimentálními kalibračními procedurami pro jednotlivá zařízení. Následně je provedena validace jednotlivých modelů. IC model je validován pomocí nezávislého tepelného schématu, kdy při srovnání s experimentálním výstupem dosahuje vysoké shody $R^2 = 0.9998$. DSC model je validován dvoufázově. Nejprve pomocí hliníkového standardu procházejícího procesem tání, přičemž srovnání experimentálního a vypočteného tepelného toku ukazuje maximální odchylku v rámci nejistoty měření (0.297 $\mathrm{mW \cdot mg^{-1}}$). Ve druhé fázi je modelována fázová přeměna křemene ($\alpha$-$\beta$), která ukazuje vysokou shodu jak s experimentálními daty, tak s nezávislými měřeními publikovaných jinými výzkumníky. Oba vytvořené modely tak mohou být považovány za schopné oddělit a kvantifikovat jednotlivé tepelné procesy probíhající uvnitř kalorimetrů a mohou tak, na rozdíl od experimentálních měření, identifikovat přesný zdroj nejistot měření. Zpracováním naměřených experimentálních dat pomocí vyvinutých modelů tak lze dosáhnout jejich očištění od systematických chyb.

Možnosti IC modelu jsou předvedeny na analýze vývinu hydratačního tepla vápenného hydrátu a Portlandského cementu, kde byl počítačový model schopen rekonstruovat teplo absorbované kalorimetrem v rané fázi hydratace. Opravený hydratační peak, extrahovaný přímo ze vzorků, poté dosahoval sedmi až dvanácti násobku naměřených hodnot. Srovnání výstupů na termočláncích, ukazující shodu $R^2 = 0.9984$ pro vápenný hydrát a $R^2 = 0.9992$ pro Portlandský cement, poté potvrdilo vysokou přesnost modelu.

DSC model je použit pro odstranění vlivu velikosti vzorku a rychlosti ohřevu na naměřené výsledky. Podobně, jako v předchozím případě, i zde je model schopný extrahovat data nikoli z místa umístění termočlánku, ale přímo ze vzorku. Aplikovatelnost modelu byla demonstrována na vápenném hydrátu. Experimentální data pro jednotlivé uspořádání byla analyzována modelem a byly stanoveny odpovídající křivky tepelného toku, které byly až o 9% vyšší díky korekci vnitřní tepelné setrvačnosti přístroje. Srovnáním experimentálních a počítačových výstupů bylo zjištěno, že nejvyšší shody je dosaženo pro takové uspořádání, kdy je vzorek vyplňující polovinu objemu kelímku zahříván rychlostí 7 K·min$^{-1}$. V tomto případě je teplotní posun křivek nižší než 5 °C a rozdíl specifického tepelného toku činí pouze 0.09 mW·mg$^{-1}$ (3.4%).

Obecně lze shrnout, že možnosti počítačových modelů korigovat zkreslení výsledků (spotřeba tepla, zpoždění výstupního signálu) vytváří dobré předpoklady pro jejich další využití na poli fyziky, chemie či materiálového inženýrství.

**Klíčová slova:** *kalorimetrické měření, počítačové modelování, systematické chyby, tepelná setrvačnost, zpoždění signálu.*

# Table of contents

# 1 Introduction

Calorimetry is a scientific discipline that deals with a measurement of changes in state variables of a body to derive the heat transfer associated with physical changes, chemical reactions or phase changes. The term calorimetry is composed of the Latin word *calor* which means *heat* and the Greek word *metron* which means *measure*. Therefore, it can be understood as *heat measuring*. Being the first who recognized a distinction between heat and temperature, the Scottish physician Joseph Black is considered to be the founder of the calorimetric science (Laidler, 1995). Devices used to perform calorimetric measurements are called calorimeters.

## 1.1 History of calorimetry

The history of calorimeters is dated back to the 18th century when Joseph Black introduced an idea of latent heat which subsequently resulted in the construction of the first calorimeter of the water-ice type.

A couple of years later, in 1780, Antoine Lavoisier involved in his experiments the first-ever animal calorimeter, a device used to measure heat production (Buchholz and Schoeller, 2004). It was on a double-shelled basis. The inner shell was filled with ice, while the outer shell of the calorimeter was covered with snow, which melted to maintain a constant temperature of 0 °C around the inner shell. There was a wire cage in the core of the inner shell, housing a guinea pig. As the ice melted from the heat produced by the guinea pig, the water flowed out of the calorimeter and was collected and weighed. Each kilogram of melted ice water represented 80 kcal heat given off by the animal. Lavoisier noted that, in 10 h, the guinea pig melted 0.37 kg of ice, thus producing 29.6 kcal of heat. Based on that he concluded that respiratory gas exchange is a combustion similarly to a candle burning. After two years, in 1782, Lavoisier and Laplace introduced another calorimeter on the ice basis. In this case, the apparatus was used to quantify the heat released from chemical reactions by means of ice melting, similarly like in the previous case.

The calorimeters introduced by Lavoisier and Laplace, however, were quite primitive. Regarding to an unclear understanding of differences between temperature and heat, that was typical for this period of science, it is not surprising that appropriate equipment for the measurement of heat changes was not available. Their devices were therefore largely ignored by their colleagues, chemists in particular. The main credit for the development of modern techniques of calorimetry is attributed to Pierre Eugène Berthelot, a French chemist, who was interested in heat measurements and constructed the first modern-like calorimeter. He also defined and described the terms exo- and endothermic reactions.

Since that time, the calorimetry has made a huge progress. Various types of more or less sophisticated calorimeters are used in most of scientific disciplines to describe heat phenomena. Pharmacy, chemistry, materials engineering, food engineering or nuclear engineering belong among examples in that respect, exploiting the principles of calorimetric measurements.

## 1.2 Types of calorimeters

There are several types of calorimeters being distinguished according to various points of view, such as their construction, source of heat or the way how boundary conditions are treated during measurements. The basic types of calorimeters are described in following subsections.

### 1.2.1 Adiabatic calorimeters

Adiabatic calorimeters are mostly used for a description of runaway reactions. Within this reactions, any heat generated by the sample tested causes the sample to increase in temperature, thus fueling the reaction. It is important to realize, that the adiabatic condition is very difficult to maintain as some amount of heat is always lost through the sample holder. These losses must be then corrected, mostly by an introduction of a mathematical correction factor that distinguishes the thermal masses of the sample and the holder by means of expressing their ratio (so called phi-factor).

Within the building materials engineering, an application of adiabatic calorimeters has been reported e.g. by Moon et al. (2018) who used it for an investigation of an influence of blast furnace slag on hydration heat of concrete. They used an adiabatic calorimeter Tokyo Riko ACM-120HA made by Gunma, Japan. The device was designed to compensate the heat loss during the measurement, which was achieved by controlling the temperature of the specimen container to be the same as the temperature at the center of the specimen.

Huo et al. (2018) developed a semi-adiabatic calorimeter that complied with the standard GB/T 12959-2008 “Test methods for heat of hydration of cement.” They used it to measure temperature profiles of a cement-slurry system and subsequent calculation of hydration heat of this system. They noticed that the heat dissipation constant of the developed semi-adiabatic test apparatus was

166.014 J·h$^{-1}$·C$^{-1}$ which is less than the value of the international standard 167 J·h$^{-1}$·C$^{-1}$.

### 1.2.2 Isothermal heat flow calorimeters

An isothermal heat flow calorimeter is designed to measure the heat by making a heat balance over the reactor wall of a jacketed reactor. The measured data can be then used to characterize, optimize and understand process parameters such as heat of reaction, heat capacity, rate of heat production or heat transfer properties. In the shell or jacket of the reactor, a uniform temperature is maintained, which can be mostly adjusted in order to control the temperature of the reactor contents. The most important terms of the heat balance are showed in Eq. (1.1)

$$Q_{\mathrm{r}} + Q_{\mathrm{f}} + Q_{\mathrm{accu}} + Q_{\mathrm{loss}} = 0 \tag{1.1}$$

where $Q_{\mathrm{f}}$ denotes the heat flow through the reactor wall, $Q_{\mathrm{r}}$ the heat flow due to the reaction, $Q_{\mathrm{accu}}$ the heat flow accumulated in the reaction mass and $Q_{\mathrm{loss}}$ the heat flow to the environment. In order to compute the term of interest, $Q_{\mathrm{r}}$, all the other terms of Eq. (1.1) must be known. The heat flow through the reactor wall, $Q_{\mathrm{f}}$, is computed according to Eq. (1.2)

$$Q_{\mathrm{f}} = U \cdot A\left(T_{\mathrm{r}} - T_{\mathrm{j}}\right), \tag{1.2}$$

where $U$ denotes the heat transfer coefficient, $A$ the transfer area, $T_{\mathrm{r}}$ the temperature of the reaction mass and $T_{\mathrm{j}}$ the jacket temperature. The term $Q_{\mathrm{accu}}$ can be computed according to Eq. (1.3)

$$Q_{\mathrm{accu}} = m \cdot c_{\mathrm{p}} \mathrm{d}T_{\mathrm{r}} / \mathrm{d}t, \tag{1.3}$$

where $m$ denotes the reaction mass, $c_{\mathrm{p}}$ the specific heat of the reaction mass, and $\mathrm{d}T_{\mathrm{r}}/\mathrm{d}t$ the derivative of the reaction temperature over time.

For a high-sensitive instrument, the different terms of Eq. (1.1) must also be measured with high sensitivity. From Eq. (1.2) it follows that an accurate measurement of the temperature difference is required for an accurate determination of the heat flow $Q_{\mathrm{f}}$. The option of reducing $U \cdot A$, in order to avoid the necessity of an accurate temperature difference measurement, is not attractive, since the $U \cdot A$ value determines how much heat the calorimeter can exchange and how fast the reactor contents can be heated or cooled (Marison et al., 1998).

An practical application of heat flow calorimeters was demonstrated e.g. by Liu et al. (2019) who used it for a description of early-age hydration kinetics of cemented paste backfill.

Also a Calvet-type calorimeters can be classified as a subcategory of heat flow calorimeters. Being typical with their three-dimensional radial arrangement of heat flux sensors, the sensitivity of the calorimeters is not affected by the crucible or the flow rate. The heat flux sensors are introduced mostly by means of various thermopiles of high thermal conductivity, that contain thermocouples connected in series. Surrounding the vessels, they ensure that major part of heat is transmitted through the thermopiles which increases the accuracy.

In case of Calvet-type calorimeters, a precise calibration plays an essential role for their further applications. The calibration procedure exploiting standard materials is therefore often omitted, being substituted by a specific electrical calibration that eliminates all the standard shortages. This type of calibration is also called the Joule effect.

### 1.2.3 Bomb calorimeters

A bomb calorimeter is a type of calorimeter that operates in a constant-volume mode. Being mostly used to measure the heat of combustion of ongoing reactions, the construction of the apparatus must be large-pressure resistant. It consists of a cup with the sample, water and oxygen being placed in a steel bomb. Stainless steel is used for this purpose as it prevents reactions typical with a volume change. Electrical energy is used to ignite the fuel which heats up the surrounding air to expand and escape through a tube that leads out of the calorimeter. The tube is surrounded by water that is heated up by the releasing air. Based on the temperature change of the water, one can determine the energy content of the fuel investigated.

The recent development of the devices resulted in their pressurization, usually at tens of atmospheres. A sample of known mass is used together with a small amount of water that ensures a saturation of the internal atmosphere, resulting in a production of liquid water only. Therefore, a calculation of vaporization enthalpy is not needed anymore. After the ignition, the combustion is initiated, releasing a heat that flows through the container and heats up the whole (closed) system and the water surrounding the bomb. Knowing the heat capacity and the temperature increase of the water, one can calculate the energy released. It is also important to consider other factors affecting the results such as energy of the electrical input for the ignition, acid production or the burning fuse. Therefore, the corresponding corrections must be made.

A bomb calorimeter was used e.g. by Carpenter and Janssens (2005) to assess the combustibility of selected materials pointing out the shortages of the building codes by comparing the results with those obtained using a cone calorimeter. Sarier and Onder (2007) used a bomb calorimeter to determine thermal behavior of polyurethane foams containing phase change materials. Overdeep and Weihs (2015) developed a bomb calorimeter of a high-sensitivity for an investigation of reactive metallic foils to measure heat generated from intermetallic formation reactions and the subsequent partial combustion of nanocomposite metallic foils.

### 1.2.4 Constant-pressure calorimeters

Heat measurements using simple calorimeters, like the coffee cup ones, belong to examples of constant pressure calorimetry, since the pressure (atmospheric) remains unchanged during the process. The coffee cup calorimeters consist of two cups and a lid that allows insertion of a rod (for stirring) and a thermometer. The inner cup contains water of a known mass that is supposed to absorb the reaction heat. The main function of the outer cup is to ensure a thermal insulation of the system.

Specific heat capacity at constant pressure, $c_\mathrm{p}$, as the most commonly measured quantity, can be expressed as

$$c_\mathrm{p} = \frac{m \cdot \Delta H}{M \cdot \Delta T}, \tag{1.4}$$

where $m$ is mass of solvent, $\Delta H$ is enthalpy of solution, $M$ is molar mass of solvent and $\Delta T$ is change of temperature. Constant-pressure calorimetry is mostly used in determining the changes in enthalpy occurring in solution. Under these conditions the change in enthalpy equals the heat.

### 1.2.5 Differential scanning calorimeters

Differential scanning calorimetry (DSC) is a measuring technique that is based on an observation of different amounts of heat used to increase the temperature of the sample and the reference. The temperature increase, that is a sample exposed to, can be linear or it follows a preset function. Based on the known value of the heat capacity of the reference, one can determine various thermal properties of the sample as a function of temperature.

The principles of DSC measurements are based on a fact, that when a sample undergoes a physical, chemical or other transformation such as phase transitions, oxidation, reduction, combustion, crystallization etc., some heat is either released or consumed in more extent than in the reference crucible which is inert. The type of heat flow depends on whether the process is exothermic or endothermic. Melting (a transformation from solid to liquid), for instance, is an endothermic process that consumes heat. Therefore, in order to reach the same temperature increase like the reference, more heat is required. Analogously, solidification or crystallization, typical examples of an exothermic processes, go along with a certain heat release which means, less heat is required to reach the same temperature increase as the reference. The particular heat flows in the sample and the reference are then compared, providing a background for an evaluation and a sample characterization. Beside the aforementioned processes like melting, solidification or crystallization, the sensitivity of DSC devises together with their principles of measurements enables to quantify also processes such as dehydroxylation, glass transition, oxidation, sintering or thermal decomposition. Several studies published refer also to determination of other material properties such as heat of fusion (Sundararajan et al., 2018; Zhang et al., 1999), phase change enthalpy (Delroisse et al., 2018), melting temperature (Velez et al., 2015), heat transport (Alok and Das, 2019; Zhang et al., 1999) or heat storage (Brutting et al., 2016; Zhang et al., 1999) parameters.

# 2 Main Objectives of the Thesis

Despite various types of calorimeters and their constructions described in the previous subsections, they always must face problems related to the accuracy of data produced. The origins of these inaccuracies are different, being mostly connected to a measurement of temperature or other quantities describing ongoing processes inside the calorimeters.

Since the temperature sensors (thermocouples) cannot be usually introduced into samples directly, it might take some time to heat to be transported from the source to the sensors. If an obstacle is present between the heat source and the thermocouple, typically crucible walls, it amplifies the inaccuracy as it consumes some part of heat as well as it redistributes it. Additionally, the materials of thermal sensors, being mostly made of combinations of various metals, are characteristic with their high value of thermal conductivity. Dealing with building materials, the thermal conductivity of the sensors is significantly higher than the thermal conductivity of the samples. The presence of the thermocouples might therefore take some part of heat and contribute to a distortion of the temperature field inside the calorimeter-sample system.

There are several methods how this issues can be treated. A precise experimental calibration of a device represents an initial step how to minimize the systematic errors. Calibration standards of known properties or electrical calibration inserts (Joule's heat) are mostly used for this purpose. Employing of correction factors is the simplest way how minimize these errors even more, being typical for adiabatic calorimeters. Mathematical corrections represent another way of the errors minimizations. Application of the deconvolution method or Tian's equation belong among the most typical examples in that respect. Unfortunately, these methods have not been always successful or the correction error provided has not been high enough. Hence other techniques are being sought.

Probably the most sophisticated and most precise technique for minimization or even elimination of the systematic errors is a utilization of computational modelling that is able to create an exact replica of given calorimeter-sample system. This approach then enables fitting the ongoing processes in the sample that produce the same outputs on the thermocouples like in the real experiment. By means of extracting the pure data from the sample directly, one obtain a description of the ongoing thermal process being free of any distortion related to the heat consumption or redistribution.

The main objective of this thesis is to present a computational technique, that is able to reduce systematic errors of calorimetric measurements. To complete the main objective, following subtasks have to be met:

- selection of representative calorimeters,
- description of the devices including their specifics,
- construction, calibration and validation of computational models of the calorimeters, and
- application of the computational models on practical examples.

The solution presented in this thesis is based on the author's research that has been already published in well-recognized journals in Web of Science database. The following publications, which has been peer-reviewed and accepted form the core of this thesis, which brings a general overview on the problem studied:

- V. Kočí, J. Maděra, M. Jerman, R. Černý, Computational analysis of heat transport and storage processes in large-volume isothermal heat flow calorimeter, *Applied Thermal Engineering* **121** (2017) 547-553.
- V Kočí, J. Kočí, J. Maděra, R. Černý, Assessment of fast heat evolving processes using inverse analysis of calorimetric data, *International Journal of Heat and Mass Transfer* **115** (2017) 831-838.
- V. Kočí, J. Maděra, A. Trník, R. Černý, Heat transport and storage processes in differential scanning calorimeter: Computational analysis and model validation, *International Journal of Heat and Mass Transfer* **136** (2019) 355-364.
- V. Kočí, J. Fořt, J. Maděra, L. Scheinherrová, A. Trník, R. Černý, Correction of errors in DSC measurements using detailed modeling of thermal phenomena in calorimeter-sample system, *IEEE Transactions on Instrumentations and Measurements* **69** (2020) 8178-8186.

# 3 Types of Calorimeters Investigated

Two different types of calorimeters were selected for the investigations within this thesis: an isothermal heat flow calorimeter and a differential scanning calorimeter, which represent most common types of calorimeters used nowadays. These devices are described in following subsections including their specifics and drawbacks that are treated later in this thesis.

## 3.1 Isothermal heat flow calorimeter

### 3.1.1 Description of the device

An isothermal heat flow calorimeter of the Calvet-type, which was originally designed by Tydlitát et al. (2012b), represents one of the calorimeters investigated in this thesis (see Fig. 3.1).

***Figure 3.1.*** *Isothermal heat flow calorimeter.*

While operating in isothermal or near-isothermal mode, the dimensions of the calorimeter (700 x 400 x 250 mm) and its spatial configuration allows investigation of large volume samples in the temperature range of 5-60 °C. It consists of two vessels, measuring and reference, each of them is provided with 24 thermopiles. Each thermopile contains a set of constantan/copper thermocouples and has two functions: it transfers heat and generates a thermoelectric voltage. All the thermopiles are connected in series so the thermoelectric voltage is proportional to the heat flow. The thermopiles from the reference vessel are connected in reverse series allowing an elimination of an external influence on the stability of the heat flow measurement. The vessels with thermopiles are placed inside an inner aluminum box. Between outer and inner boxes, there is a ventilated air gap with controlled temperature.

The calibration of the calorimeter is performed using Joule heat produced by a constantan wire wound on an aluminum insert of known resistance, which is shaped as the measuring vessel (see Fig. 3.2).

***Figure 3.2.*** *The aluminum calibration insert.*

### 3.1.2 Specifics of isothermal heat flow calorimeters

Isothermal heat flow calorimeters of various types are widely used in thermal science and engineering. Determination of waste heat produced by silver zinc batteries (Ubelhor et al., 2015), hydration heat development in $MgSO_4$ hydrates (Posern and Kaps, 2008), composite binders (Han et al., 2016), and low-clinker cements (Klemczak and Batog, 2016), or specific heat capacity and thermal conductivity of lithium batteries (Bazinski and Wang, 2015) can be listed as just a few characteristic examples in that respect. Most commercial devices use small measurement vessels, typically up to 10 cm$^3$, which suits well for many materials and applications. In the case of heterogeneous materials or their systems, however, large-volume calorimeters making possible handling the specimens up to 1000 – 1500 cm$^3$ can be required to monitor properly the interactions of system components (Tydlitat et al., 2012b).

Despite apparent advantages over some other calorimetric techniques, such as a straightforward calibration process and the measurement at an exactly specified temperature, making possible to obtain data well defined from the physical point of view (Tydlitat et al., 2008), the use of isothermal heat flow calorimeters may be affected by their intrinsic drawbacks, which must be taken into account in the experiments. Probably the biggest challenge that must be faced is the quantification of heat in early or very early stages of heat evolving processes. The first problem consists in the mixture preparation procedure (e.g. mixing with water) that may cause the early heat to be released already before placing the mixture into a calorimeter. However, it can be eliminated by using a proper calorimeter construction that allows mixtures to be prepared inside. Meeting this requirement, such apparatuses have been described or used, e.g., by Evju (2003) or Xu et al. (2015). The second problem is closely connected to the construction of calorimeters as well, since they may be responsible for a significant heat consumption due to their internal heat capacity. This possible inaccuracy can be neglected in case of major heat power peaks that appear after sufficiently long periods of time. In building materials engineering, for example, many cements have the major peak approximately after 10 hours (Medina et al., 2016), i.e., there is time enough to reach a thermal equilibrium. On the other hand, fast heat evolving processes are difficult to be detected precisely. The corresponding heat power peaks are usually higher than the major peaks but they are very narrow, thus the overall amount of heat is much smaller and easier to be consumed in the beginning of the measuring procedure. Calorimeters designed for large volume samples make this problem even more important, but small calorimeters must face this problem as well because of the proportionality of the device and the sample. Many researchers therefore plot their results with the initial phase being cut off (Alhozaimy et al., 2015; Bohac et al., 2017; Jansen et al., 2012).

The time-delay problem of isothermal heat flow calorimeters can easily be demonstrated by a comparison of a constant calibration pulse of known heat power with the corresponding calorimetric output. Even though these quantities are supposed to be identical, in practical experiments they are not (see Fig. 3.3) and must be corrected.

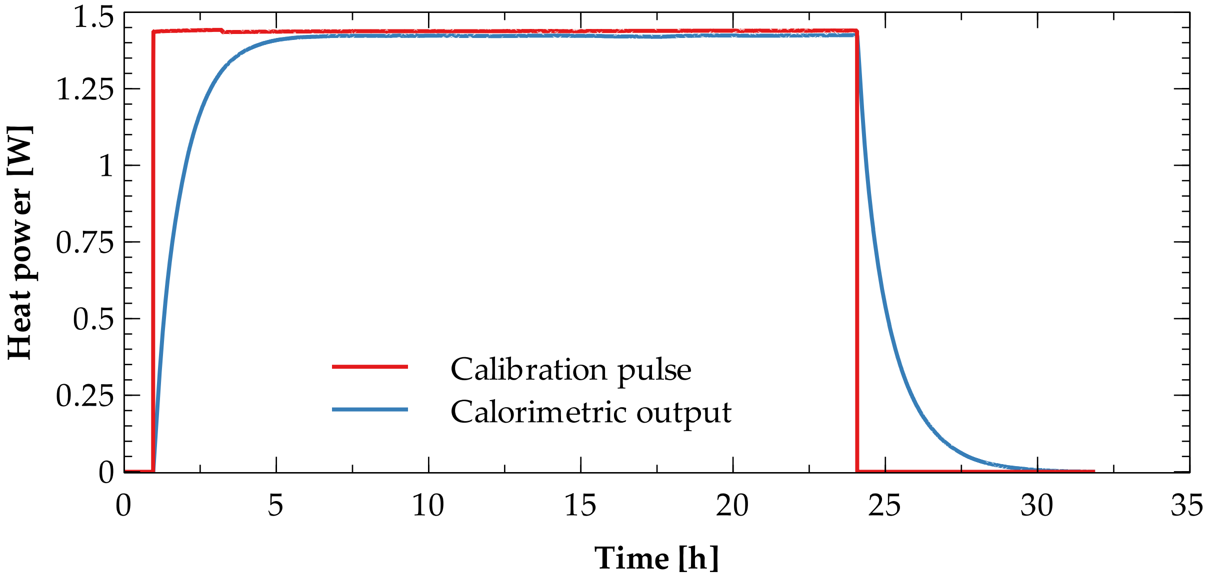

***Figure 3.3.*** *Characteristic response of the calorimeter to a rectangular heat pulse.*

Probably the most frequently used correction represents the application of Tian equation (Calvet and Prat, 1963). Gao et al. (2006) used it for the transformation of curves describing the hydration process of calcium phosphate cement. Another application of Tian equation was reported by Dumas et al. (2014) who used it for the characterization of phase change materials. Determination the time response at the calibration of their calorimetric system, García-Cuello et al. (2009) successfully exploited the Tian equation as well. However, at the study of initial hydration heat development in cementitious materials Evju (2003) pointed out a disadvantage of the application of Tian equation, as it assumes uniform temperature within the cells. It is obvious that this assumption is unrealistic, e.g., for fast reactions or thermal transfer barriers that exist inside calorimeters (Randzio and Suurkuusk, 1980). Therefore, Evju (2003) assumed two zones with uniform temperatures which led to a second-order differential equation with two time constants. As an alternative to Tian equations of any order, the deconvolution method was presented (Yamane et al., 1991) which was based on reproducing the hydration curves using numerical algorithms based on fast Fourier transform. Nevertheless, she was unable to reproduce the original rectangular calibration pulse using any of these methods. The reason can be seen in the mathematical nature of the solution which cannot handle the problem of unsmoothed curves that are typical for calibration pulses.

Another way to achieve the corrections demanded represents the computational modelling. Being found an effective tool for solving specific problems of various calorimetric methods before (Haloua et al., 2012; Choinski et al., 2016; Sen et al., 2015), the computational modelling of thermal transport and storage processes in the isothermal heat flow calorimeter is further introduced, developed and applied in following subsections.

## 3.2 Differential scanning calorimeter

### 3.2.1 Description of the device

The second device analyzed in this thesis is Labsys™ Evo DTA/DSC made by SETARAM Inc. (see Fig. 3.4a). It is suitable for demanding high temperature experiments involving mostly inorganic materials. The device is equipped with DSC sensor rod (see Fig. 3.4b), that contains two crucibles – reference and measuring.

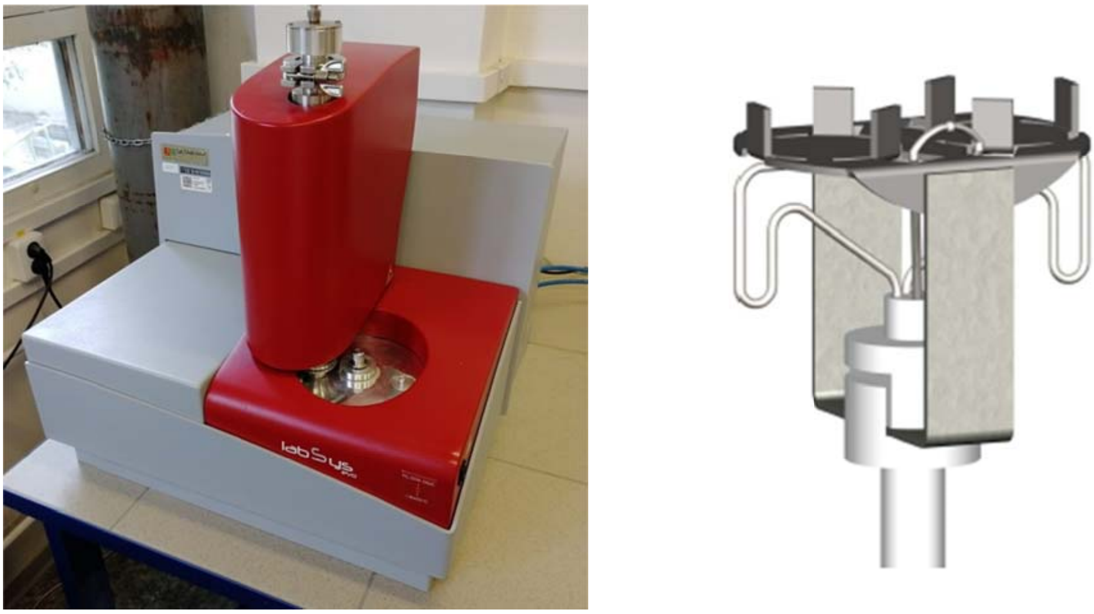

**(a)** **(b)**

***Figure 3.4.*** *Labsys Evo DTA/DSC device* ***(a)****, DSC sensor rod* ***(b)***

The principle of DSC analysis consists in measuring the voltage difference between the crucibles placed on the sensor that is subsequently converted to heat power using a calibration function. The voltage difference, being recorded by a pair of thermocouples, occurs only when a thermal process takes place in the measurement crucible. Since the measurements are performed in the furnace under high temperatures up to 1600 °C, the thermal processes can be usually ascribed to phase transition, dehydration, combustion, or decomposition of the sample tested.

The DSC rod comprises a machined metallic tray featuring two recesses for the measurement and reference crucibles and four-wire ceramic shaft accommodating the different thermocouples (measurement, reference). All the components are made of high-temperature resistant materials. The thermocouples used are of type S (Pt-Pt Rh 10%). Regarding the sensor construction, the first source of inaccuracies comes out from the position of thermocouples. Although they are supposed to record temperature of crucibles' content, they are placed on the bottom side of the plate. The signal delay which is therefore generated due to thermal inertia is then eliminated by shifting the results along the temperature axis using a constant estimated at the experimental calibration procedure.

The device can be connected to a sweeping gas circuit which protects the crucibles and the samples against oxidation. Also the sensors are protected against oxidation when the temperature exceeds 500 °C. Particular atmosphere can be also selected and imposed to cause the sample to react, if required. Within the analyses presented in this thesis, argon was used as the sweeping gas having the exchange rate of 40 $ml \cdot min^{-1}$.

### 3.2.2 Specifics of differential scanning calorimeters

Differential scanning calorimetry belongs to the most frequently used experimental techniques developed for the investigation of thermophysical properties of materials. However, despite of its wide usage, the measurement results are still often affected negatively by several phenomena, of which interpretation and elimination might be difficult for end-users, as a DSC device is commonly used as a gray box.

A signal delay (Albrecht et al., 2001) together with a gas convection inside the device (David et al., 2017) present the most obvious sources of inaccuracy which are independent of the properties of tested materials. The influence of sample size and sample heating rate is less straightforward. The signal delay originates from the position of heat flux sensors or temperature sensors which cannot be introduced into tested samples. The measured data are then not recorded directly. Since it takes some time the heat to be transferred from the sample to the sensor, a signal delay occurs. Additionally, heat capacity of the sample and internal parts of the DSC device causes heat inertia that may result in partial consumption of heat transferred between the sample and the sensor, thus a signal distortion. The data detected on the sensors are then smaller than real values on the sample. Metals and alloys (Hajra et al., 2017), or generally materials with high thermal conductivity and low specific heat capacity make this effect less important but for other material types it should be taken into account as a significant factor (Kuznik et al., 2011; Saeed, R.M. et al., 2016). Its magnitude was demonstrated, e.g., by Hasan et al. (2014), Tyagi and Buddhi (2008), or Sari and Karaipekli (2008) who reported differences in melting temperature of up to 2.1 °C and heat of fusion of up to 22.0 $kJ \cdot kg^{-1}$ for several materials.

Some disadvantages of DSC devices can be eliminated experimentally. The producers encourage the users to perform a calibration procedure using various standards (usually pure metals) of known parameters. The signal delay can then be overcome by introducing a calibration constant that is used for results shifting. However, such an approach still does not deal with the heat inertia issues resulting in the fact, that different heating rates and different sample masses produce different results when the same material is analyzed. This was reported, e.g., by Saeed et al. (2016) who studied thermal performance of selected fatty acids and concluded that the most accurate results were achieved (compared to the NIST reference data) at the heating rate of 3 $°C \cdot min^{-1}$ and the sample mass of 7.5 mg. The results of such optimization experiments cannot though be generalized and their applicability is limited to materials of which properties were determined before by some other method.

Another possibility how to moderate the negative effects of the mentioned disadvantages of DSC devices presents the utilization of computational techniques. For instance, David et al. (2017) developed an energy conservation model to quantify the influence of natural convection perturbations on DSC results in dependence on heating rate. Javdanitehran et al. (2016) introduced an iterative procedure for estimation of released energy during rapid heat-up phase that increased the precision of obtained results. Nevertheless, also the currently used computational methods, such as those described above are mostly aimed at the particular cases only and cannot be generalized. A novel method of computational modelling of thermal transport and storage processes in the differential scanning calorimeter is therefore introduced, developed and applied in following subsections.

# 4 Computational Models of Calorimetric Devices

As presented in Section 3, there are two types of calorimeters from the point of view of their operating mode. However, regardless of their dimensions, operation mode, calibration procedures or samples preparation regimes, both calorimeters investigated within this thesis exhibit several specifics that have direct influence on the results provided. Being described in details in the previous sections, these drawbacks can be effectively eliminated or at least significantly reduced using a computational modelling technique that is able to identify ongoing thermal processes to extract pure data free of systematic errors. In order to perform the computational modelling analyses, the models have to be constructed, calibrated and validated at first. These procedures for the particular calorimeters are given in following subsections.

## 4.1 Isothermal heat flow calorimeter

### 4.1.1 Model construction

Three different data sources were used for the model construction: a personal inspection of the calorimeter, data from the original publication of Tydlitát et al. (2012b) and data published in a record in the utility models database of Industrial Property Office (IPO) of the Czech Republic under document No. CZ 20426 U1. The model construction process is summarized in Fig. 4.1.

The main preprocessing work was done in GiD 13.0. The volumes corresponding to particular materials were assigned to a linear model of the calorimeter (see Fig. 4.2) using MeshEditor (Benes and Kruis, 2015) and a tetragonal mesh formed by 70883 nodes and 366544 elements was generated. Fig. 4.3 shows the 3D model of the calorimeter with assigned materials and generated mesh where the outer cup and the lids of measuring and reference vessels are uncovered for the sake of a better view of the inside of the calorimeter. The aluminum internal walls are marked with green color, the vessels are yellow, the thermopiles are purple and the calibration insert is highlighted using horizontal color stripes. The outer layer of the model was formed by an air layer which was 15 mm thick (not shown in Fig. 4.3). Taking into account its controlled temperature during the experimental measurements (25 °C), this layer served as a carrier of boundary conditions in the computational model and other outer layers such as the outer metallic coat or thermal insulation could be neglected.

Since the computational modeling assumes a transient heat transport while transport of other media is not considered, only thermal transport and accumulation parameters and basic physical properties are required. All the materials in the computational model are assumed as stationary matter. In view of the fact, thermal conductivity of air that surrounds internal parts of the calorimeter has to be used in the apparent value form. That means employment of all the heat transfer modes is necessary. Hence beside conduction also convection and radiation are taken into account. Heat transfer specifics on material interfaces are considered within the apparent value as well. Because it would be very complicated to calculate a precise value of the apparent thermal conductivity of air accommodating all the mentioned phenomena, it was set as a free parameter and its precise value was determined using a calibration procedure that is described later in this thesis.

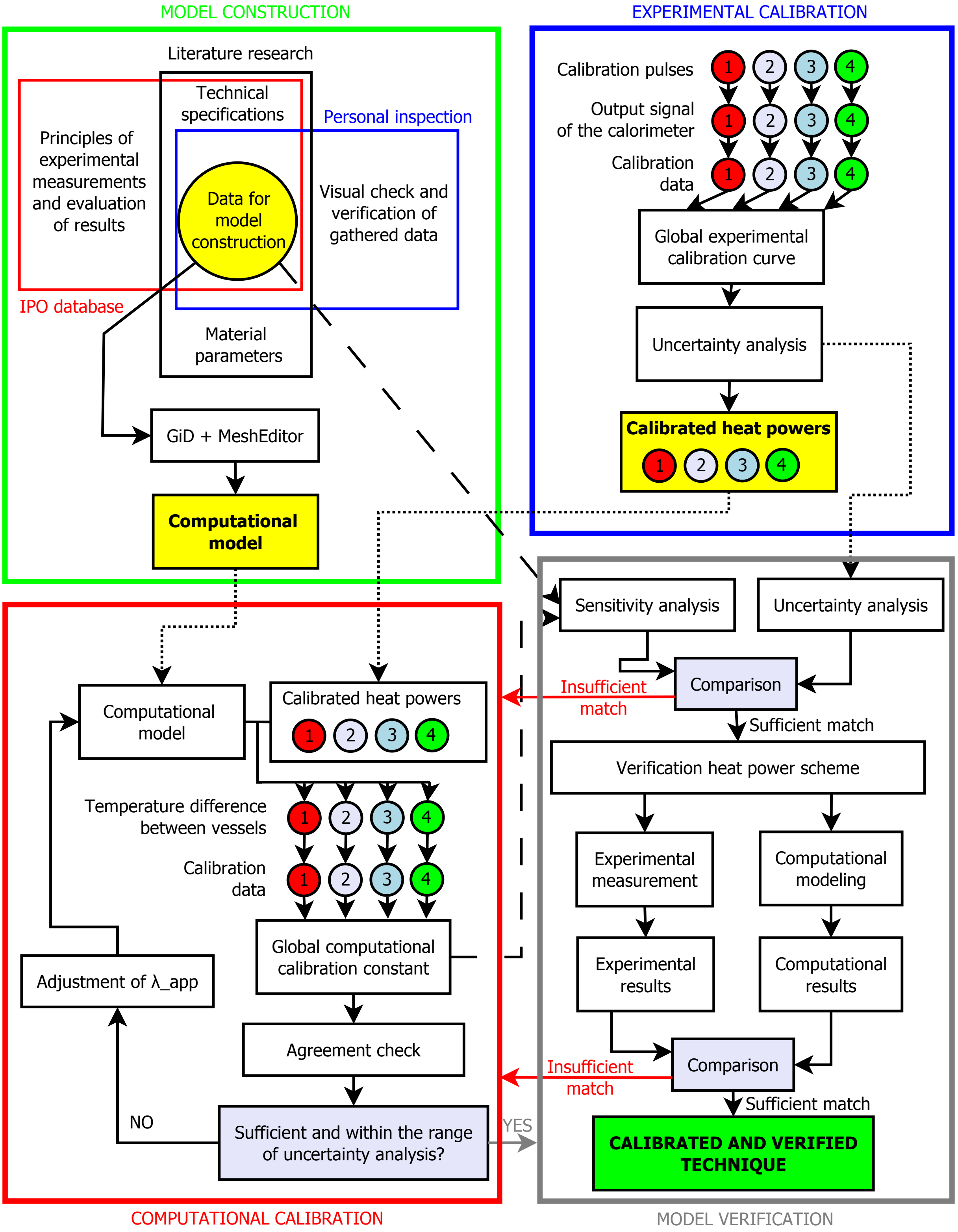

***Figure 4.1.*** *Overall scheme of model construction, calibration and validation.*

The material parameters serving as input data for the model are summarized in Tab. 4.1. The parameters of aluminum and air are generally known, the properties of thermopiles were set using homogenization techniques based on their known composition (constantan, copper and fiberglass board). Being mentioned before, the apparent thermal conductivity of the air surrounding the internal parts of the calorimeter was assumed as a free parameter and its precise value was determined using a calibration procedure that will be described later.

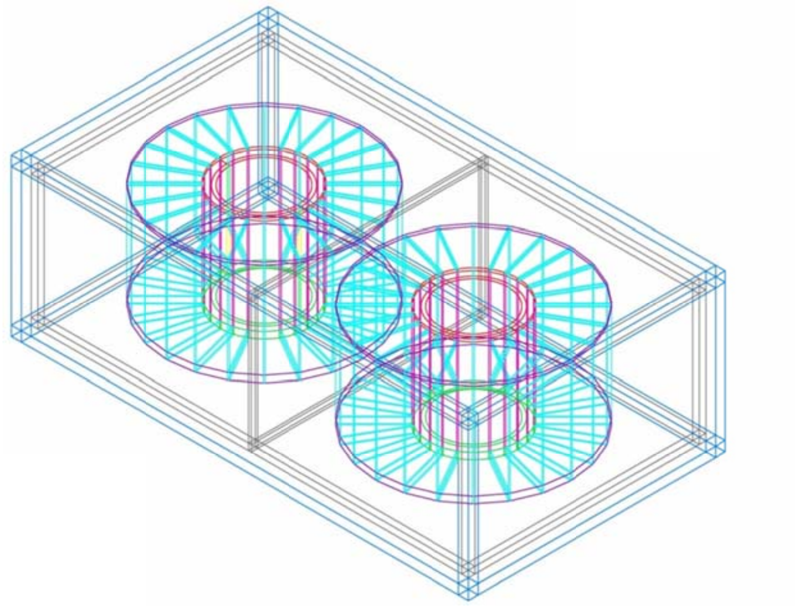

***Figure 4.2.*** *Linear model of the calorimeter.*

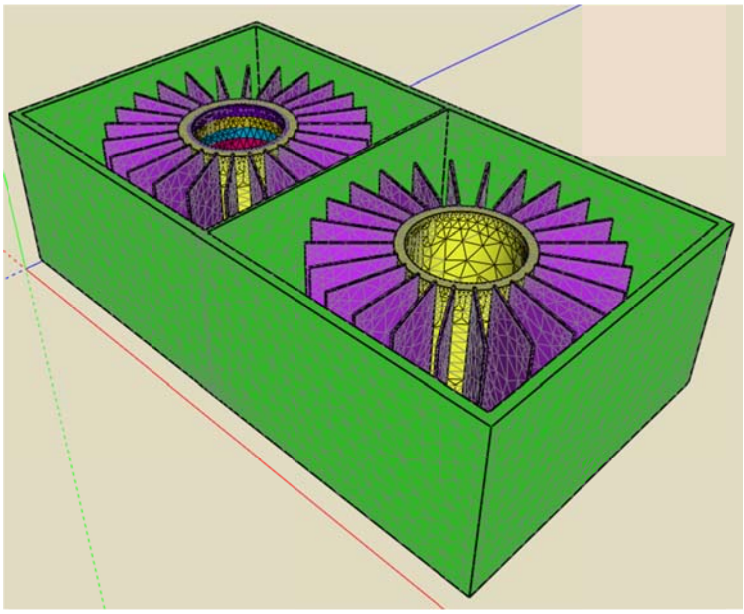

***Figure 4.3.*** *3D model of the calorimeter with assigned materials and generated mesh.*

The temperature field in the system was determined using the finite-element computer code SIFEL (Kruis et al., 2010). The evaluation of computational results was the same, in principle, as the evaluation of real experimental data. The experimental output of the calorimeter is based on a temperature difference between the vessels, while the temperatures are recorded using thermocouples (in thermopiles) on the vessels' external surface. Therefore, the temperatures in the model were recorded in the nodes where the thermopiles were connected to the vessels. Similarly to the experiment, the temperature differences (or the corresponding output voltage, respectively) were converted to the heat power using the calibration curves.

***Table 4.1.*** *Parameters of materials involved in the isothermal heat flow calorimeter.*

| Material (calorimeter part) | Bulk density [kg·m$^{-3}$] | Thermal conductivity [W·m$^{-1}$·K$^{-1}$] | Specific heat capacity [J·kg$^{-1}$·K$^{-1}$] |
|---|---|---|---|
| Aluminum (vessels, calibration insert, inner aluminum box) | 2700 | 237 | 900 |
| Constantan + copper + fiberglass (thermopiles) | 2250 | 20 | 1017 |
| Air | 1.168 | free parameter for system calibration | 1011 |

### 4.1.2 Calibration and validation procedures

The calibration procedure had two steps. In the first one, the experimental calibration of the calorimeter was performed. In the second, the calibration of the computational model was carried out and both techniques were linked. The validation of the model was done using a comparison of experimental and computational data obtained for an independent heat power function. The overall scheme of the calibration and validation procedures is shown in Fig. 4.1.

#### 4.1.2.1 Calibration of the experimental device

The calibration of the calorimeter was done for four different heat power pulses, $P_i$ [W], which were calculated from the Ohm's law, based on the known resistance of the calibration insert, $R$ [Ω], and known input voltages, $U_i$ [V]. After the steady state had been reached, the output signal was recorded. The experimental calibration curve was then constructed as a polynomial approximation of the second order with the highest $R^2$ value. The experimental data were subjected to an uncertainty analysis according to GUM (ISO/EIC 98-3, 2008), and the expanded standard uncertainty at the confidence level of 95 % was determined.

#### 4.1.2.2 Calibration of the computational model

The calibration of the model consisted in introducing a computational calibration curve and adjusting the apparent thermal conductivity of the air surrounding the internal parts of the calorimeter, $\lambda_{app}$ [W·m$^{-1}$·K$^{-1}$], as the free parameter of the model. At first, the calibrated heat powers were assigned to the volumes in the model that corresponded to the calibration insert. The temperature differences related to particular pulses were then recorded. Subsequently, the computational calibration curve converting the obtained temperature differences to heat powers was determined similarly as in the experimental calibration, using the data for all calibration pulses. An iterative procedure was used to achieve a good agreement between the experimental and computational results.

#### 4.1.2.3 Validation of the model

In the first phase of model validation, the experimental and computational data obtained in the calibration procedures were analyzed using the results of uncertainty analysis (experimental measurement) and sensitivity analysis (computational modeling). In the uncertainty analysis, the class of accuracy of the device generating the input voltage (Diametral P230R51D device, CoA = 2, ± 0.6 V), the controlled temperature of circulating air between the inner and outer coatings of the calorimeter (± 0.15 K) and the uncertainty of the experimental calibration curve presented the most important parameters. The sensitivity analysis was performed using limit values of input parameters. In the second phase, an independent heat power function (of known value) was applied in both experimental measurement and computational modeling and the results were compared.

### 4.1.3 Results of the calibration procedure

The experimental calibration was performed using four different voltages on the aluminum insert (10.18 V, 16.99 V, 20.82 V and 24.02 V) that were applied for a time period long enough to reach a steady state of the system. The corresponding output signals of the calorimeter were recorded (see Tab. 4.2) and the experimental calibration curve was constructed and depicted in Fig. 4.4.

***Table 4.2.*** *Results of experimental calibration of the isothermal heat flow calorimeter*

| Pulse number $i$ | Resistance of the insert $R$ [Ω] | Input voltage $U_i$ [V] | Heat power $P_i = U_i^2 \cdot R^{-1}$ [W] | Output signal of the calorimeter [mV] | Calibrated output signal of the calorimeter [W] |
|---|---|---|---|---|---|
| 1 | 72.1 | 10.18 | 1.437 | 9.37 | 1.465 |
| 2 | | 16.99 | 4.003 | 23.83 | 3.967 |
| 3 | | 20.82 | 6.012 | 34.17 | 5.936 |
| 4 | | 24.02 | 8.002 | 43.88 | 7.921 |

The slightly parabolic shape of the calibration curve in Fig. 4.4 can be explained by the decreasing resistance of constantan wire (in the calibration insert) with increasing temperature.

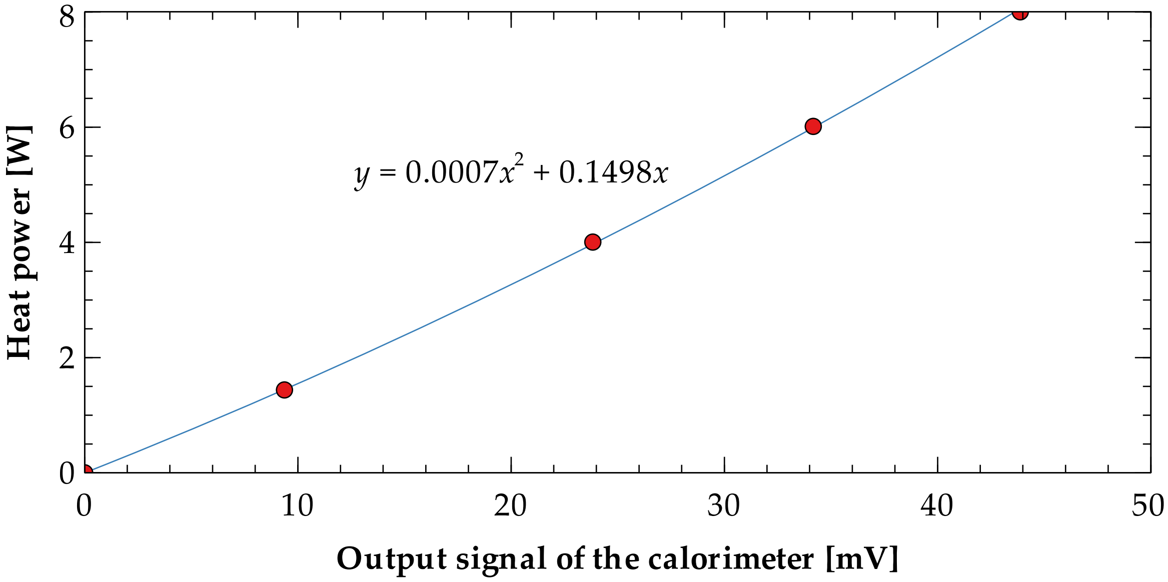

***Figure 4.4.*** *The experimental calibration curve of the isothermal heat flow calorimeter.*

The overall scheme of the experimental calibration process including the input heat pulses and calibrated outputs of the calorimeter is presented in Fig. 4.5. The uncertainty of the measurement was calculated as ± 0.1909 W; it is visualized in this figure using dotted lines.

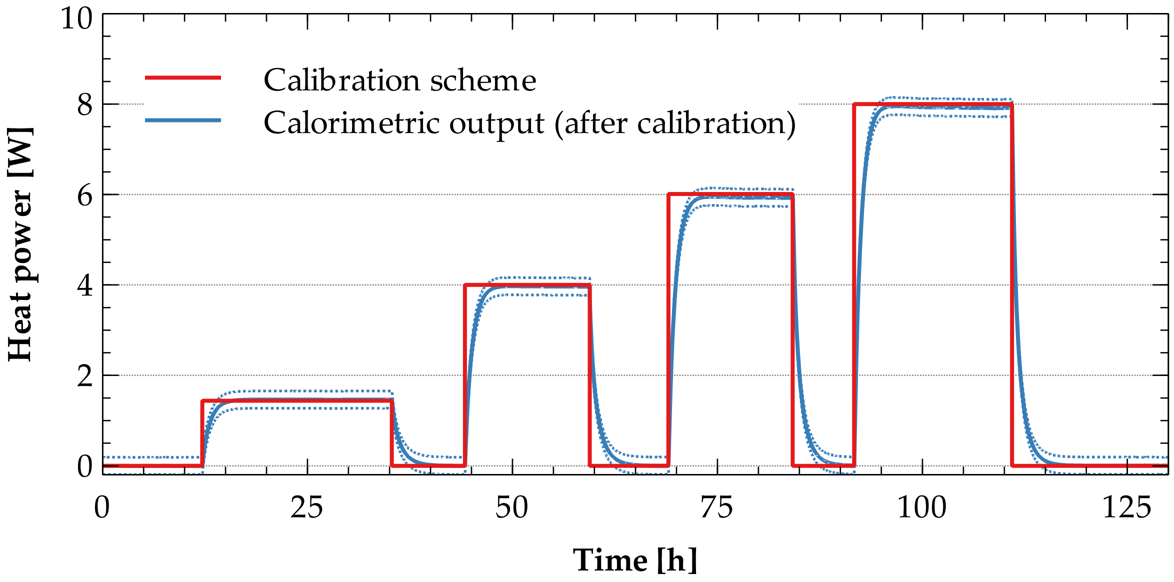

*Figure 4.5. Overall scheme of the experimental calibration process.*

The calibrated output signals of the calorimeter shown in Tab. 4.2 were used as constant input heat power pulses in the computational model. The temperature differences between the particular vessels were calculated and the computational calibration constants were determined as summarized in Tab. 4.3. Unlike experimental calibration, the calibration constants did not change significantly over the analyzed temperature difference range. Therefore, the average value of 1.204812 W·K$^{-1}$ was used in further calculations.

*Table 4.3. Results of computational calibration.*

| Pulse number | Calibration heat power [W] | Temperature difference between the vessels [K] | Computational calibration constant [W·K$^{-1}$] |
|---|---|---|---|
| 1 | 1.465 | 1.216 | 1.204846 |
| 2 | 3.967 | 3.293 | 1.204762 |
| 3 | 5.936 | 4.927 | 1.204764 |
| 4 | 7.921 | 6.574 | 1.204877 |

The apparent thermal conductivity, $\lambda_{app}$ [W·m$^{-1}$·K$^{-1}$], of the air surrounding the internal parts of the calorimeter does not have any influence on the steady-state values of temperature difference between the vessels, thus it does not have any effect on the computational calibration constant. However, it has a strong impact on the shape of computational output curves (see the demonstration examples in Fig. 4.6), as it controls the relaxation period of the system.

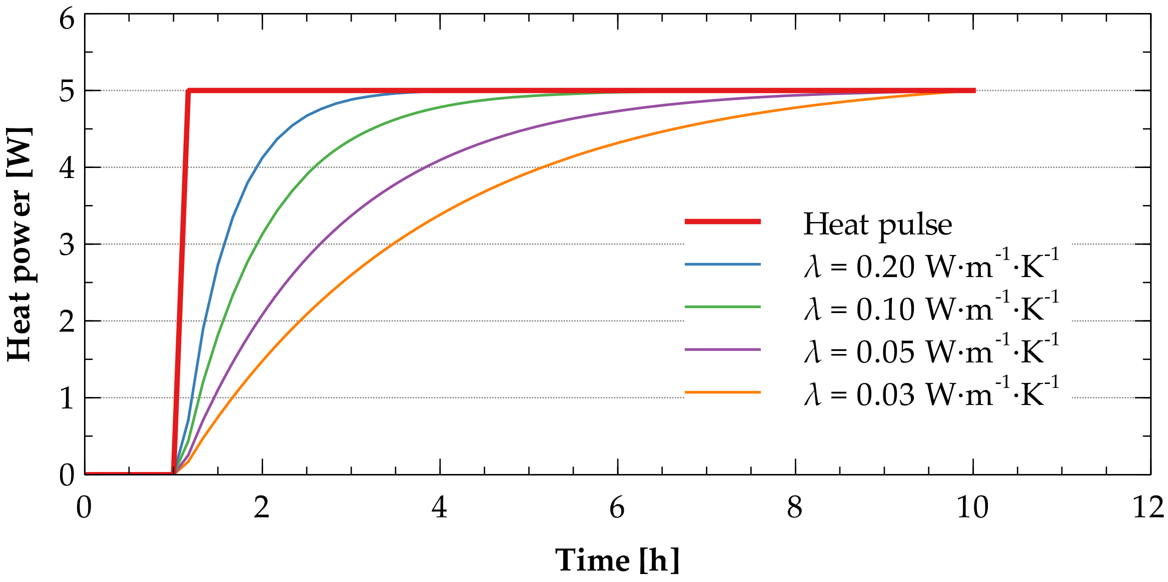

***Figure 4.6.*** *The effect of apparent thermal conductivity of the air surrounding the internal parts of the calorimeter on computational outputs.*

The best agreement between the experimental and computational outputs was achieved when $\lambda_{app}$ = 0.120 W·m$^{-1}$·K$^{-1}$ had been assumed. The comparison of experimental and computational results provided with the error ranges obtained using the uncertainty and sensitivity analyses is given in Fig. 4.7, showing a very good agreement.

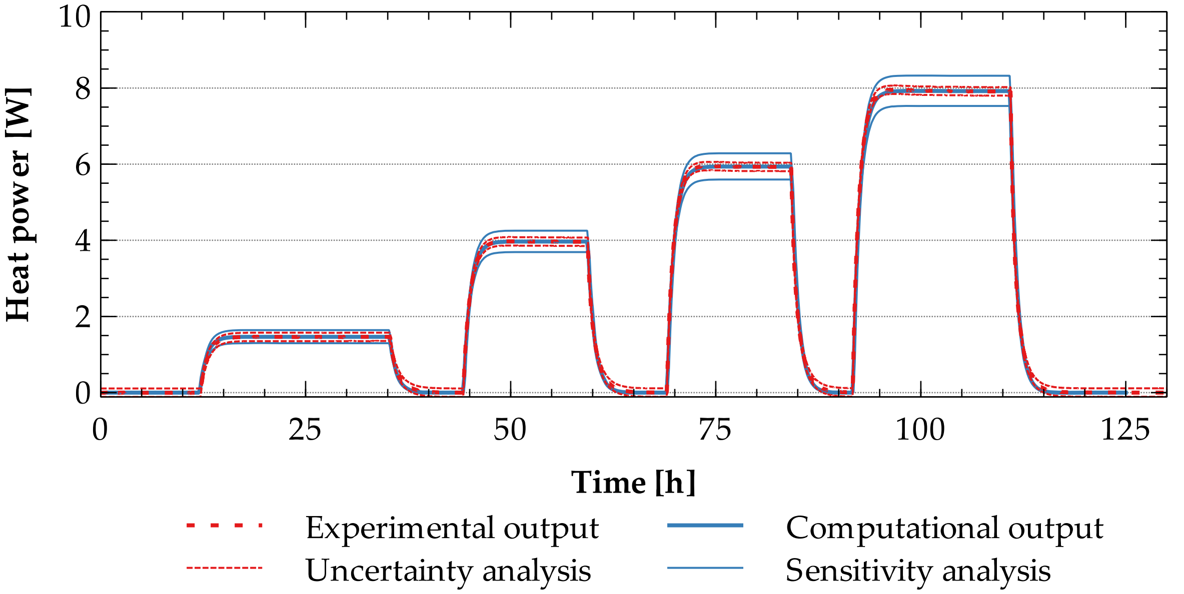

***Figure 4.7.*** *Comparison of experimental and computational outputs at the calibration process.*

### 4.1.4 Results of the validation procedure

The model validation was performed using a heat power function that was independent on the calibration scheme used before. The experimental and computational outputs were produced, using the previously determined calibration parameters. The results of the validation procedure are given in Fig. 4.8. An excellent match between the experimental and computational outputs ($R^2$ = 0.9998) is apparent, confirming the realistic performance of the computational model and giving it good prerequisites for practical applications.

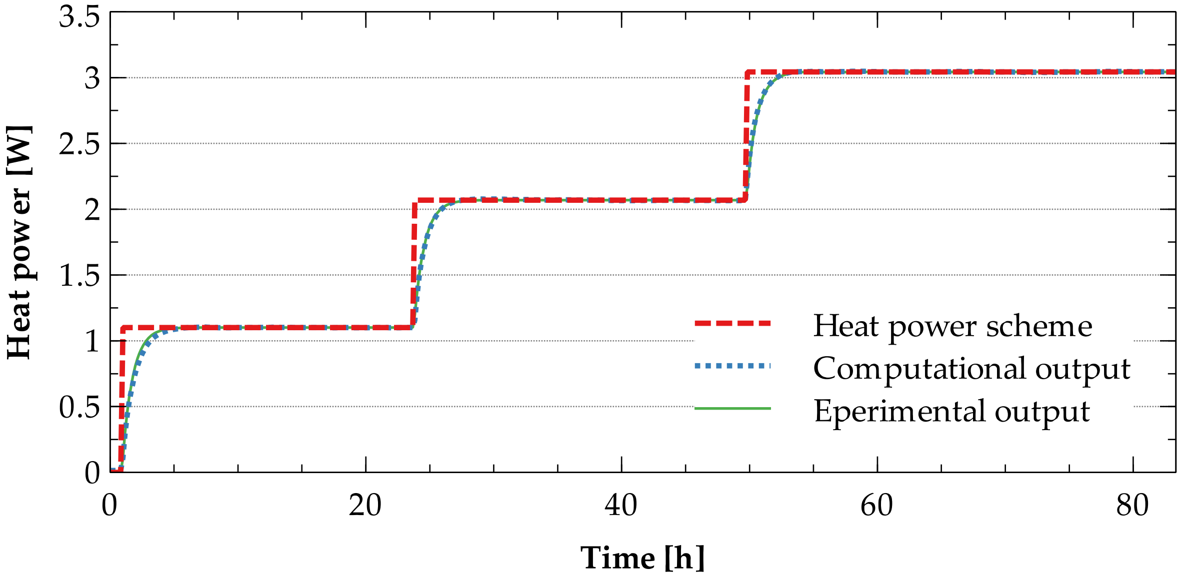

***Figure 4.8.*** *Comparison of experimental and computational outputs at the validation procedure.*

The greatest advantage of the computational model after its calibration and validation consists in the fact that all the input parameters entering the modeling process are either known or easy to obtain. This concerns the input heat power, in particular. In practice it means that any experimental output curve from the calorimeter can be simulated using the developed model, while the input heat power curve is fitted as an unknown parameter. Genetic programming, genetic algorithms, or even simplex optimization techniques belong to the group of fitting methods that can be used for that purpose. Such an approach can substitute mathematical corrections of experimental data used so far, that mostly exhibited rather high uncertainties. This was reported by Evju (2003), who tried to apply Tian equation with one or two time constants and the deconvolution method, but failed in reproducing the original heat power pulse from the experimental output. The problem was identified in the pure mathematical nature of this solution that was not able to deal with rapid changes of the current generating a non-smooth shape of the calibration pulse. Therefore, negative values of heat power were obtained in certain periods of time because of the exaggerated use of the second derivative or overcorrections due to the least square fitting (Evju, 2003). There is a good reason for the conclusion that computational modeling could serve much better in that respect, as it was demonstrated on the selected large-volume isothermal heat flow calorimeter in Section 4.1.

## 4.2 Differential scanning calorimeter

### 4.2.1 Model construction

The computational model was constructed based on the personal inspection of the device and the technical specification given by the producer. The model involved the inner parts of the furnace having a controlled heating wire around the inner surface. After the dimensions of particular parts and other specifications had been gathered, the linear model was created with an emphasis put on discretization around the tiny details, such as wires and plates, of which thickness was only 0.3 mm. After the linear model had been drawn, it was further developed using the GiD 13.0 preprocessing software. Here, the NURBS surfaces were assigned to each flat segment defined by particular lines (Fig. 4.9) and after that the volumes were created by means of definition by boundary surfaces. Finally, particular materials were assigned to the volumes. The complexity of the model can be expressed via numbers of entities at this point of processing, as the model consisted of 2255 lines, 1733 surfaces and 410 volumes.

The temperature distribution was modeled using the three-dimensional heat transport equation

$$\rho c \frac{\partial T}{\partial t} = \operatorname{div}\left(\lambda \cdot \operatorname{grad} T\right) = \frac{\partial}{\partial x}\left(\lambda \frac{\partial T}{\partial x}\right) + \frac{\partial}{\partial y}\left(\lambda \frac{\partial T}{\partial y}\right) + \frac{\partial}{\partial z}\left(\lambda \frac{\partial T}{\partial z}\right) \tag{4.1}$$

where $t$ [s] is the time, $T = T(x, y, z, t)$ [K] is the temperature as a function of space and time, $\lambda$ [$\mathrm{W \cdot m^{-1} \cdot K^{-1}}$] is the thermal conductivity, $\rho$ [$\mathrm{kg \cdot m^{-3}}$] is the bulk density, and $c$ [$\mathrm{J \cdot kg^{-1} \cdot K^{-1}}$] is the specific heat capacity.

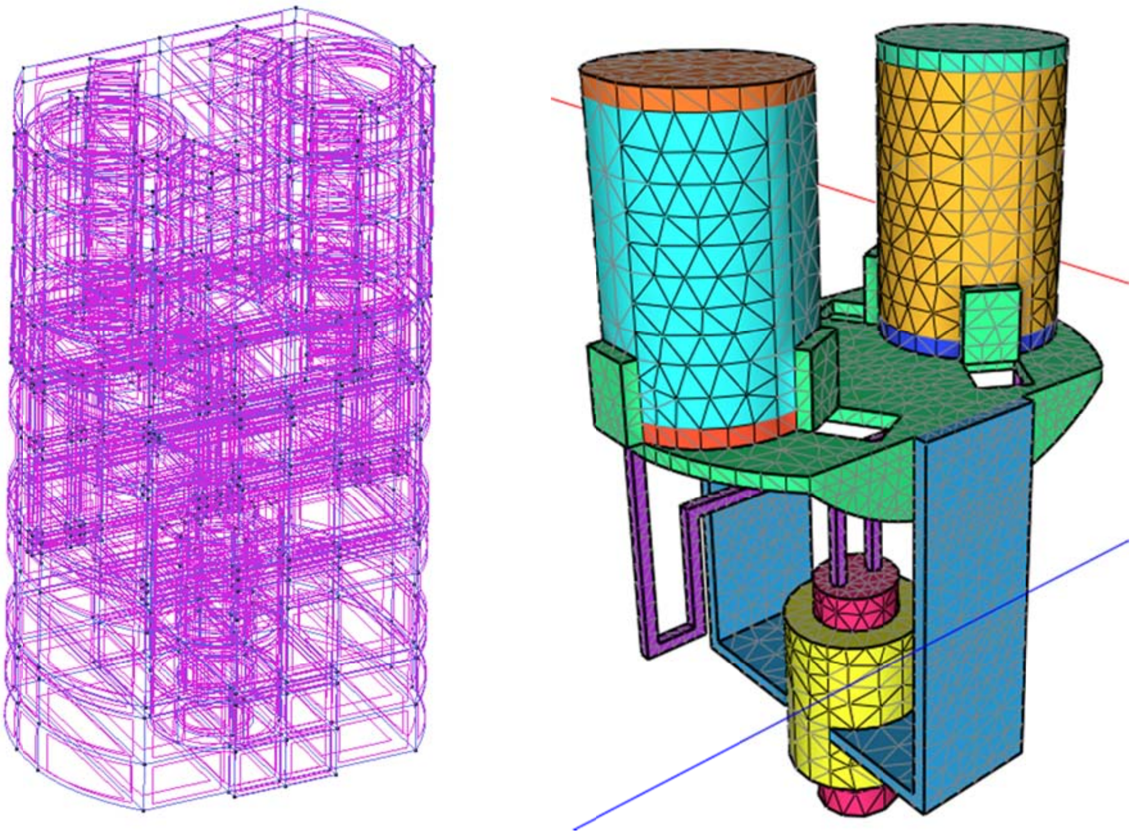

**(a)** **(b)**

***Figure 4.9.*** *The computational model of the DSC rod: Linear model with surfaces assigned **(a)**, Computational mesh with materials assigned **(b)**.*

The computational mesh required for the numerical solution of heat transport using finite element method comprised 121015 nodes and 692071 tetrahedral elements. Such high numbers predisposed the numerical solution to be expensive either on time or on computing power. The high demands were solved by parallelization of the whole problem, meaning that it was solved simultaneously on a cluster of computers (Madera et al., 2017). The mesh with materials assigned is depicted in Fig. 4.9b. The volumes corresponding to the gas surrounding the DSC rod are not shown because of the illustrative nature of the figure.

The temperature dependent thermal properties of materials involved in the model are summarized in Tab. 4.4 (Powell et al., 1966; Shakhtin et al., 1982). The thermal conductivity of the sweeping gas (argon) was assumed in the form of an apparent value that accommodated also convective and radiative transfer modes. Having a direct influence on the output data, its precise value was determined at the calibration procedure.

*Table 4.4.* *Parameters of materials involved in the differential scanning calorimeter.*

| Material (calorimeter part) | Bulk density [kg·m$^{-3}$] | Thermal conductivity [W·m$^{-1}$·K$^{-1}$] | Specific heat capacity [J·kg$^{-1}$·K$^{-1}$] |
|---|---|---|---|
| Platinum–Rhodium10 % (plate) | 20546 | see Fig. 4.10 | 130 |
| Platinum (wires) | 21450 | | 134 |
| Corundum (shaft, crucibles) | 4020 | | 126 – 1255 |
| Argon (steady in crucibles) | 1.661 | 0.00652 – 0.05888 | 520 |
| Argon (sweeping gas) | 1.661 | free parameter for system calibration | 520 |

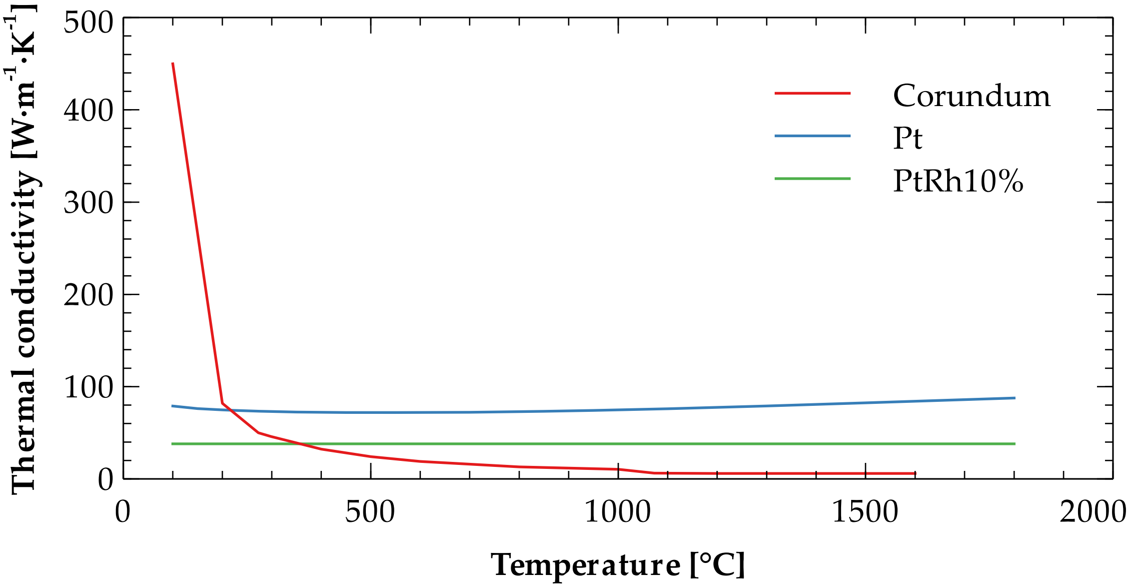

*Figure 4.10.* *Thermal conductivity of involved materials.*

Since the temperature in the furnace is regulated using a control heating wire wounded around the inner furnace periphery, Dirichlet boundary conditions were applied to the lateral sides of the model, complying with the wire placement. The boundary temperature was then set in the same way as in the heating schedule of the experiment, which means the identical heating rate of 5 °C·min$^{-1}$ was applied.

The investigated sample was assigned to the corresponding volume inside the measurement crucible. The thermal processes were then detected in the model like in the real device, i.e., the temperature difference between the thermocouples placed under the crucibles was recorded.

### 4.2.2 Calibration and validation procedures

The calibration procedure comprised two independent steps, the experimental calibration of the device and the calibration of the model. Both techniques were then linked and the validation was performed by means of a comparison of experimental and computational data obtained for independent materials. The scheme of the calibration and validation procedure is captured in Fig. 4.11. The particular procedures are described in Subsections 4.2.2.1 – 4.2.2.3.

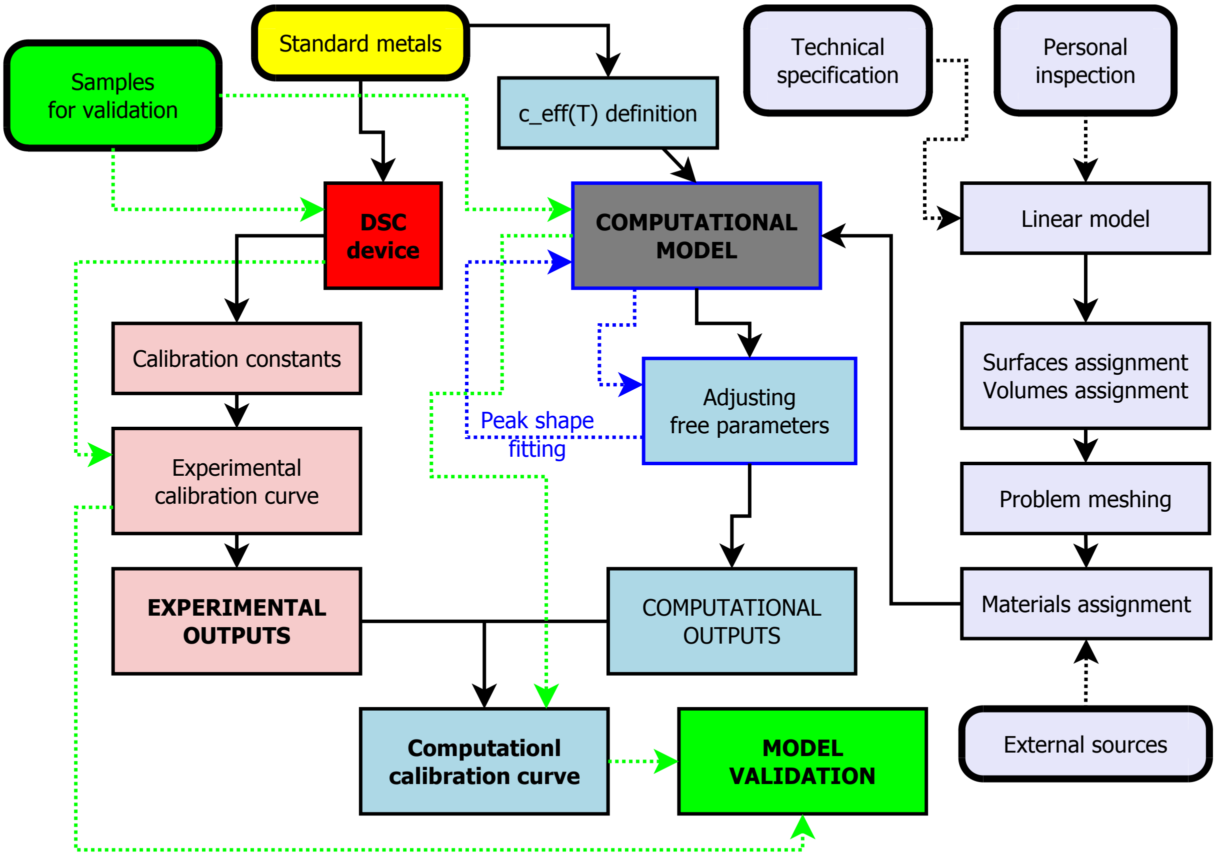

*Figure 4.11. Flowchart of the calibration and validation procedures.*

#### 4.2.2.1 Calibration of the DSC device

The reference standards summarized in Tab. 4.5 were used for the experimental calibration of the device in order to transform the electric voltage, $U$ [μV], into heat power, $P$ [mW]. Since the calibration coefficient varies with temperature, the calibration with a single standard is very rare in the practice. According to the producer at least five standards are recommended. Therefore, indium, tin, silver, gold, and zinc were used for the calibration in this thesis.

***Table 4.5.*** *Standard reference materials for calibration.*

| Material | Melting enthalpy, $H$ [J·g$^{-1}$] | Melting temperature, $T_m$ [°C] | Ref. |
|---|---|---|---|
| Indium | 28.51 ± 0.19 | 156.60 | NIST SRM 2232 (NIST, 2013) |
| Tin | 60.21 ± 0.19 | 231.94 | NIST SRM 2220 (NIST, 2013) |
| Lead | 23.00 ± 0.06 | 327.47 | LGC 2608 (LGC, 2014) |
| Zinc | 107.4 ± 1.60 | 419.56 | NIST SRM 2221A (NIST, 2013) |
| Aluminum | 401.30 ± 1.60 | 660.33 | LGC 2612 (LGC, 2014) |
| Silver | 104.80 | 961.78 | (Emsley, 1998) |
| Gold | 64.50 | 1064.18 | (Sarge et al., 1994) |
| Nickel | 300.00 | 1455.00 | (Richardson and Charsley, 1998) |

The calibration coefficient $K_i$ [μV·mW$^{-1}$] at the melting temperature $T_{m,i}$ [°C] was expressed as

$$K_i = \frac{A_i}{H_i} \cdot \frac{1}{m_i}, \tag{4.2}$$

where $H_i$ [J·g$^{-1}$] is the theoretical melting enthalpy of the standard, $A_i$ [μV·s] is the area of the melting peak, and $m_i$ [g] is the mass of the sample. Subsequently, a regression function was used for the expression of the experimental calibration curve as a function of temperature. At the experimental calibration process the results were subjected to the uncertainty analysis according to GUM (ISO/EIC 98-3, 2008). In case replicate observation had not been applied, the uncertainty was evaluated by means of standard uncertainty of type B which is based on manufacturer's information, calibration certificates of measuring instruments, or expert's estimates. Otherwise, the standard uncertainty of type A was included, being based on statistical evaluation of sets of measured data. Since detailed descriptions of analyses of single measurements would be very space-demanding, only the expanded uncertainties corresponding to 95 % confidence level are presented alongside the measured mean values of particular quantities.

### 4.2.2.2 Calibration of the model

The same standards that had been previously used for experimental calibration were used also at the calibration of the model. Besides the temperature dependent thermal conductivity (Fig. 4.12) (Kaye&Laby Online, 2005; Powell et al., 1966), the calibration standards were described also using the effective specific heat capacity as a function of temperature, $c_{\mathrm{eff}}$ $[\mathrm{J\cdot kg^{-1}\cdot K^{-1}}]$, accommodating the phase change enthalpy as

$$\int_{T_1}^{T_2} c_{eff}\,\mathrm{d}T = H, \tag{4.3}$$

where $T_1$ and $T_2$ [K] are temperatures corresponding to the phase change region. This approach is advantageous in computational modelling as it does not require further re-meshing and can be easily implemented in an existing model. The effective specific heat capacity concept was previously used, e.g., by Mandilaras et al. (2015), Kočí et al. (2016a), or Medveď et al. (2017). Following the principles proposed by Krabbenhoft et al. (2007), the relation between effective specific heat capacity and phase change process is depicted in Fig. 4.13.

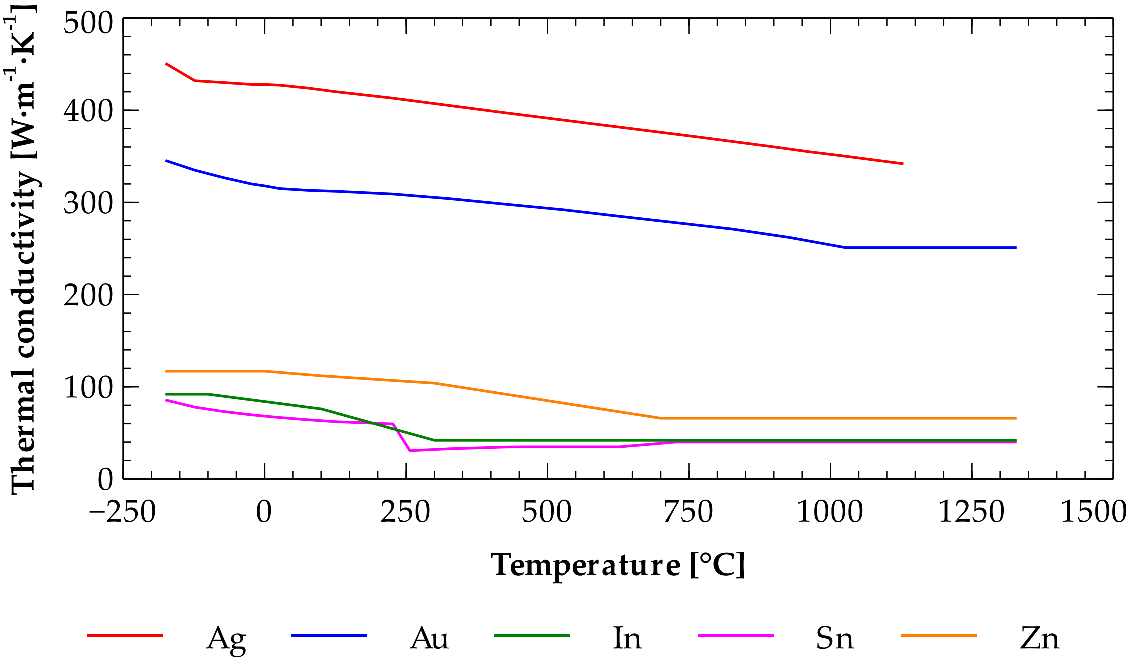

*Figure 4.12. Thermal conductivity of used standards.*

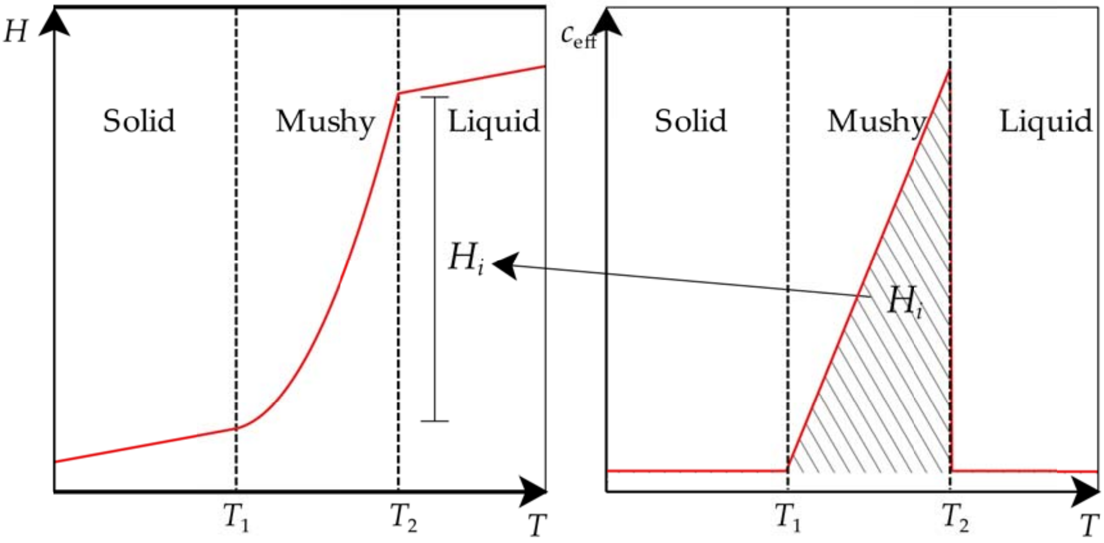

***Figure 4.13.*** *Definition of the effective specific heat capacity.*

The main output of the model was the thermoelectric voltage difference that came out from the temperature readings in the positions of the thermocouples. The conversion between temperature and voltage was done using the standard conversion formula for S-type thermocouples. Harmonizing the peak tops of both experimental and computational outputs, the computational calibration constants, $K_{c,i}$ [mW·μV$^{-1}$], were determined for particular temperatures and the computational calibration curve was constructed using a regression function. During the calibration procedure, the apparent thermal conductivity of the sweeping gas, $\lambda_{sg}$ [W·m$^{-1}$·K$^{-1}$], as the free parameter of the model was adjusted as well, because it was assumed to incorporate all three heat transfer modes.

#### 4.2.2.3 Validation of the model

Validation of the model was performed using two different materials and processes. The first analyzed process was melting of aluminum as one of the standards (Tab. 4.5) which was not used in the calibration procedure. The results obtained using both the calibrated experimental device and the calibrated computational model were compared with the standard data and discussed. The second experiment used for validation purposes consisted in determination of the effective specific heat capacity of quartz as a representative of commonly studied materials which are though not standardized for DSC experiments, including its $\alpha$-$\beta$ transition. In this case, the experimental and computational outputs were compared both each other and with the results published by other researchers in the scientific literature.

### 4.2.3 Results of the experimental calibration procedure

While heated above the melting point, the solid standards are turned into liquids evoking a slight movement inside the crucible as the materials evenly fill the bottom. This might cause a signal distortion. The calibration procedure of each standard therefore consists of three heating and cooling processes, while only the last heating results are taken into account. The raw data used for the device calibration is plotted in Fig. 4.14 and the summary is given in Tab. 4.6. The different voltage for particular samples displayed in Fig. 4.14 can be explained by different inertia of reference and measurement crucibles which can produce temperature shifts and thus also change the thermoelectric voltage on the thermocouples. However, it does not influence the calibration procedure, because only the areas under the peaks are considered and the final results are usually interpreted with the peak baselines being adapted to zero.

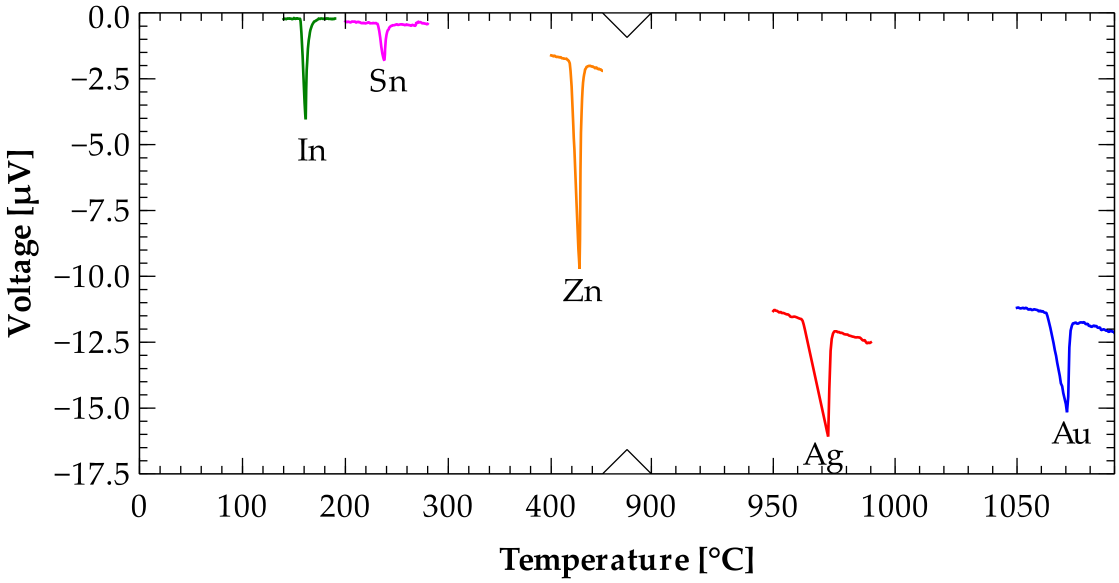

*Figure 4.14. Summary of raw data for the device calibration.*

*Table 4.6. Summary of experimental calibration procedure.*

| Material | $H_i$ [J·g$^{-1}$] | $A_i$ [μV·s] | $m_i$ [mg] | $K_i$ [μV·mW$^{-1}$] |
|---|---|---|---|---|
| Indium | 28.51 ± 0.19 | 190.2888 ± 4.3689 | 23.4 ± 0.3 | 0.285233 ± 0.015475 |
| Tin | 60.21 ± 0.19 | 85.5579 ± 10.8695 | 5.3 ± 0.1 | 0.268111 ± 0.019034 |
| Zinc | 107.40 ± 1.60 | 572.4695 ± 13.3264 | 21.3 ± 0.3 | 0.250247 ± 0.015525 |
| Silver | 104.80 | 298.8401 ± 11.5660 | 13.4 ± 0.2 | 0.212801 ± 0.017654 |
| Gold | 64.50 | 224.3637 ± 6.1262 | 19.8 ± 0.2 | 0.175682 ± 0.010229 |

The experimental calibration curve constructed using $K_i$ values presented in Tab. 4.6 is shown in Fig. 4.15. It is plotted as a polynomial regression function of fourth order.

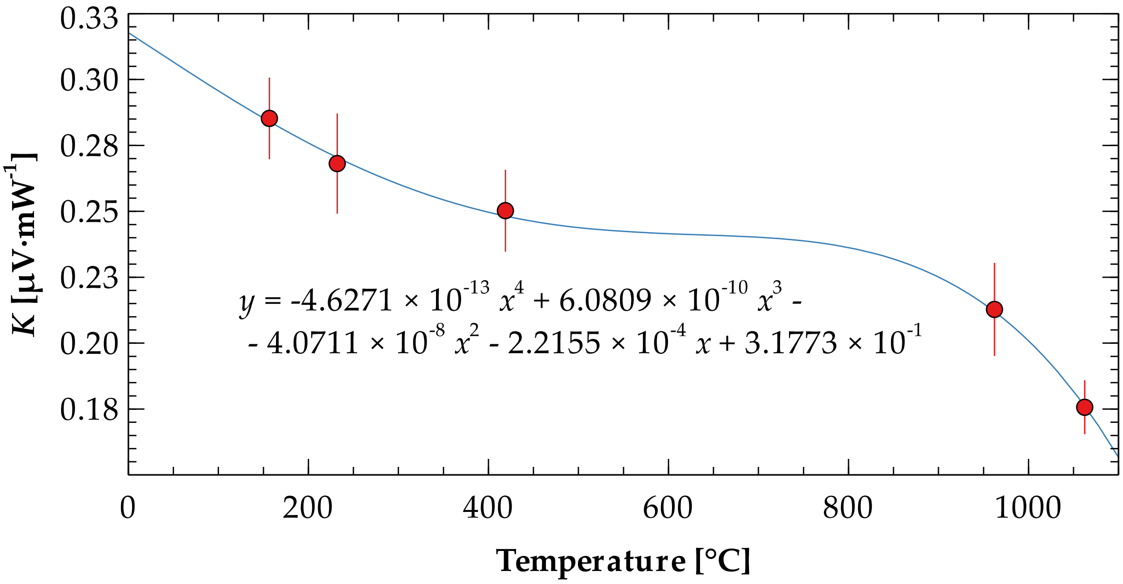

***Figure 4.15.*** *Experimental calibration curve of the DSC device.*

After the analytical expression of the experimental calibration curve had been determined, the new samples of the same materials were tested again. The results are shown in Tab. 4.7. The differences between reference and experimental data after the calibration served as a data source for the calibration accuracy expression. It can be seen that the accuracy of the DSC device was higher when samples were not exposed to more than ~500 °C. In this case the difference between experimental outputs and theoretical values was less than ~8%. On the other hand, when temperature about 1000 °C was reached, the relative deviation reached ~11 – ~16%.

***Table 4.7.*** *Summary of experimental measurement after calibration.*

| Material | $m_i$ [mg] | $T_i$ [°C] | $H_{i,\text{theoretical}}$ [J·g$^{-1}$] | $H_{i,\text{experimental}}$ [J·g$^{-1}$] | Difference |
|---|---|---|---|---|---|
| Indium | 23.5 | 156.60 | 28.51 | 28.48 | 0.105 % |
| Tin | 10.8 | 231.94 | 60.21 | 65.45 | 8.006 % |
| Zinc | 20.8 | 419.56 | 107.40 | 114.30 | 6.037 % |
| Silver | 20.4 | 961.78 | 104.80 | 89.93 | 16.535 % |
| Gold | 19.7 | 1064.18 | 64.50 | 72.68 | 11.255 % |

The calibrated experimental curves with adjusted baselines are shown in Fig. 4.16 including results of uncertainty analysis (the dotted lines). These curves were used for the subsequent fitting of the outputs in the computational modeling procedure.

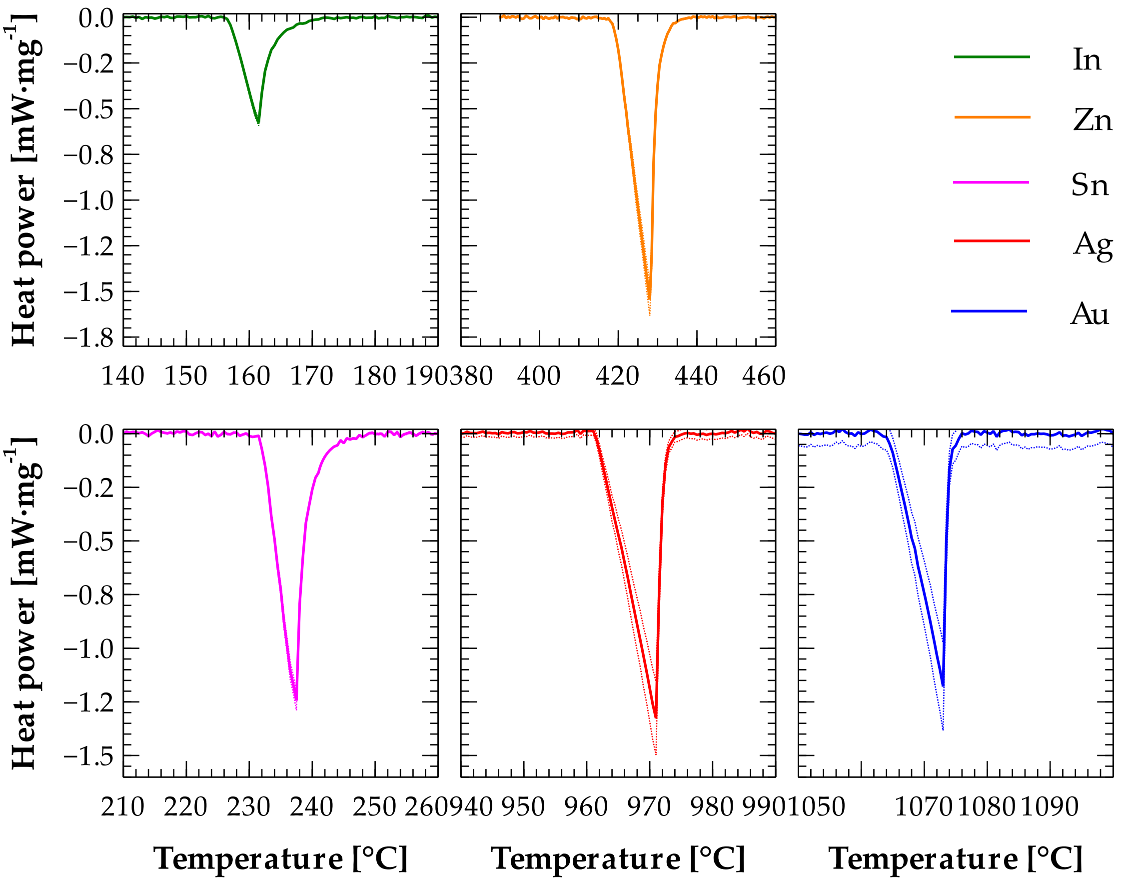

***Figure 4.16.*** *Calibrated experimental outputs from the DSC devices.*

### 4.2.4 Results of the computational calibration of the model

Prior to the computational calibration, effective specific heat capacities as functions of temperature of the analyzed standards were set. Mushy zones were assumed according to Krabbenhoft et al. (2007), where $T_1$ corresponded to the melting temperatures $T_m$ summarized in Tab. 4.5, and $T_2$ to the temperatures of the experimental peak tops. Using Eq. (4.3), the maximal $c_{eff}$ values were calculated. The summary is given in Tab. 4.8.

***Table 4.8.*** *Effective specific heat capacities of the standards in the mushy zones.*

| Material | $T_1$ [°C] | $T_2$ [°C] | $c_{eff,max}$ [kJ·kg$^{-1}$·K$^{-1}$] |
|---|---|---|---|
| Indium | 156.6 | 161.5 | 6.97 |
| Tin | 231.9 | 237.5 | 15.08 |
| Zinc | 419.6 | 428.0 | 21.87 |
| Silver | 961.8 | 971.0 | 20.99 |
| Gold | 1064.2 | 1073.0 | 13.57 |

The free parameter of the computational model, i.e., $\lambda_{sg}$ [W·m$^{-1}$·K$^{-1}$], was fitted during the calibration procedure as it has direct impact on the shape of output curves. Affecting the amount of heat taken away from the crucibles, lower values of $\lambda_{sg}$ result in slower growth of the output curves after the peak towards a baseline. On the other hand, higher values of $\lambda_{sg}$ produce much steeper increase. It can be anticipated, that higher temperatures go along with higher values of $\lambda_{sg}$ as the radiation heat transfer mode is more significant than conduction and convection. Such an assumption is in agreement with the experimental outputs presented in Fig. 4.16, where a slower growth after the peak tops can be observed in case of indium and tin compared to zinc, silver, or gold.

Tab. 4.9 and Fig. 4.17 show that the accuracy of the computational model was very high, especially in the high temperature region, reaching $R^2$ values between 0.999794 and 0.999997. The thermal conductivity of the sweeping gas was expressed as a function of temperature following the polynomial function of the third order, which complies with the theory presented by Modest (2000) who defined the radiative heat flux between two surfaces as

$$-\lambda_{\mathrm{rad}} \frac{\Delta T}{\Delta x} = \varepsilon\sigma\left(T_{\mathrm{a}}^4 - T_b^4\right) \tag{3.4}$$

where $\lambda_{rad}$ [W·m$^{-1}$·K$^{-1}$] is the radiative thermal conductivity, $\varepsilon$ [-] is the emissivity, $\sigma = 5.6704 \times 10^{-8}$ W·m$^{-2}$·K$^{-4}$ is the Stefan-Boltzmann constant, $T_a$ and $T_b$ [K] are surface temperatures, and $\Delta x$ [m] is the distance between the surfaces.

***Table 4.9.** Summary of results of computational calibration procedure.*

| Material | $K_{c,i}$ [mW·μV$^{-1}$] | $R^2$ [-] | $\lambda_{sg}$ [W·m$^{-1}$·K$^{-1}$] |
|---|---|---|---|
| Indium | 8.9317 | 0.999794 | 0.038 |
| Tin | 7.0876 | 0.999916 | 0.052 |
| Zinc | 5.6605 | 0.999958 | 0.103 |
| Silver | 4.6167 | 0.999995 | 0.433 |
| Gold | 6.1132 | 0.999997 | 0.499 |

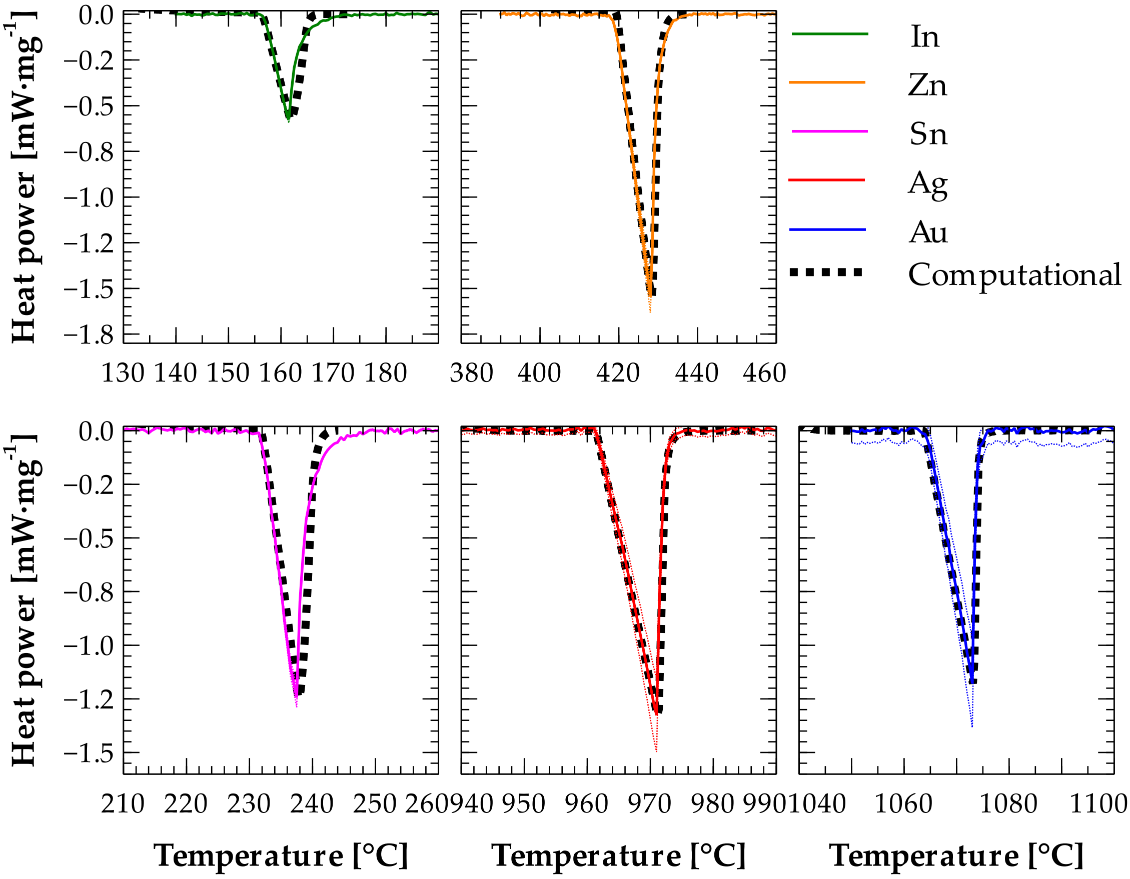

***Figure 4.17.*** *Results of the computational calibration of the model.*

Eq. (4.4) was used for the approximation of the radiative heat transfer in the model, after investigation of its parameters and thermal performance when the system was heated. It was found, that the average distance between DSC sensor parts and the heating wire was 0.018 m, the average temperature difference between the sensor and the boundary surface was 3 K. Together with the standard thermal conductivity of argon (Powell et al., 1966), the values of $\lambda_{sg}$ used as a free parameter of the model are depicted in Fig. 4.18.

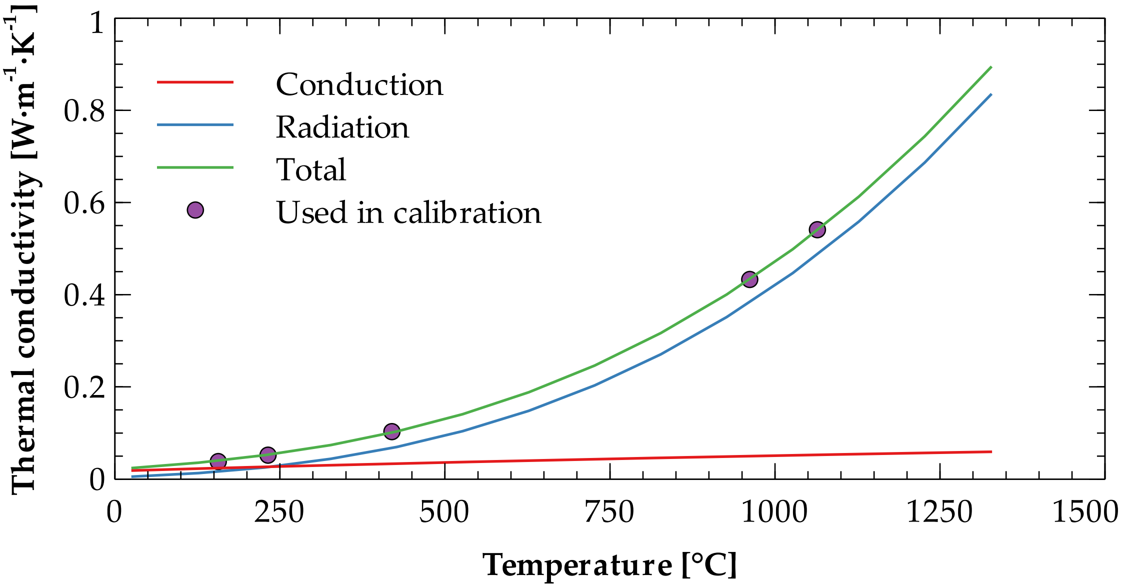

***Figure 4.18.*** *Thermal conductivity of the sweeping gas.*

The computational calibration curve constructed using particular calibration constants given in Tab. 3.9 can be written in the form

$$K_c(T) = 1.009\times10^{-10}T^4 - 2.486\times10^{-7}T^3 + 2.194\times10^{-4}T^2 - 8.428\times10^{-2}T + 17.645 \quad (4.5)$$

### 4.2.5 Model validation

The first step of the model validation was done by means of both experimental and computational analysis of aluminum and the subsequent outputs comparison. The particular results were processed using the experimental calibration function (see Section 4.2.3) or the computational calibration function and the adjusted free parameter of the model (see Section 4.2.4). The material properties of aluminum needed for the computations were taken from (LGC, 2014; Powell et al., 1966), being depicted in Fig. 4.19. The step change of thermal conductivity corresponds to the solid-liquid phase change. The bulk density of 2700 kg·m$^{-3}$ was used.

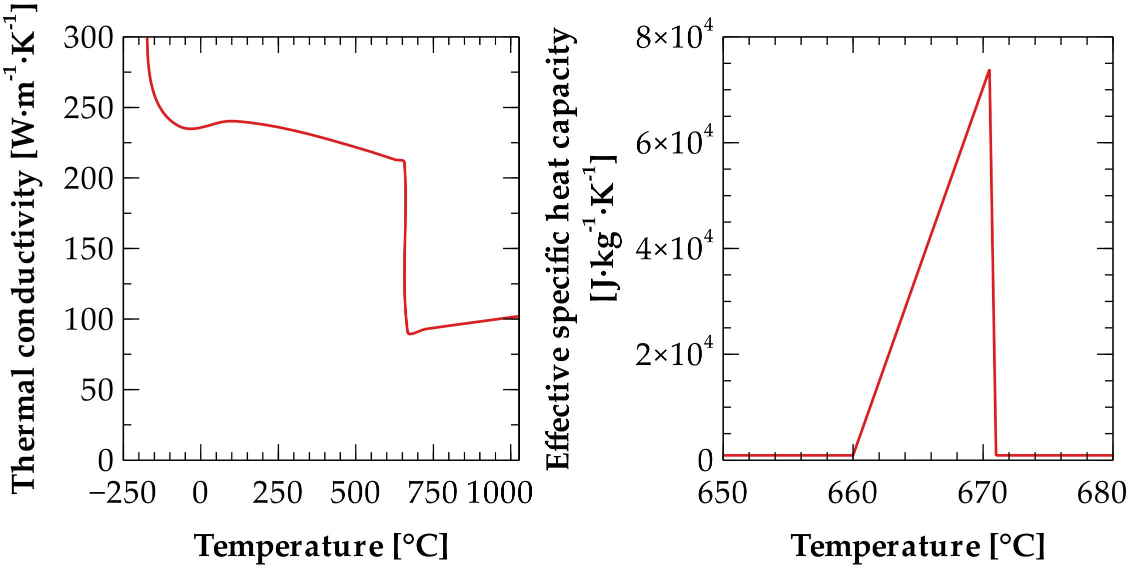

*Figure 4.19. Thermal properties of aluminum used for model validation.*

The comparison of experimental and computational outputs is given in Fig. 4.20. A very good agreement between the particular outputs can be observed and even if there is a difference accounting for 0.279 mW·mg$^{-1}$ on the peak tops, it is still within the uncertainty of the experimental measurement. The results presented in Fig. 4.20 can be therefore considered as an evidence of proper model configuration.

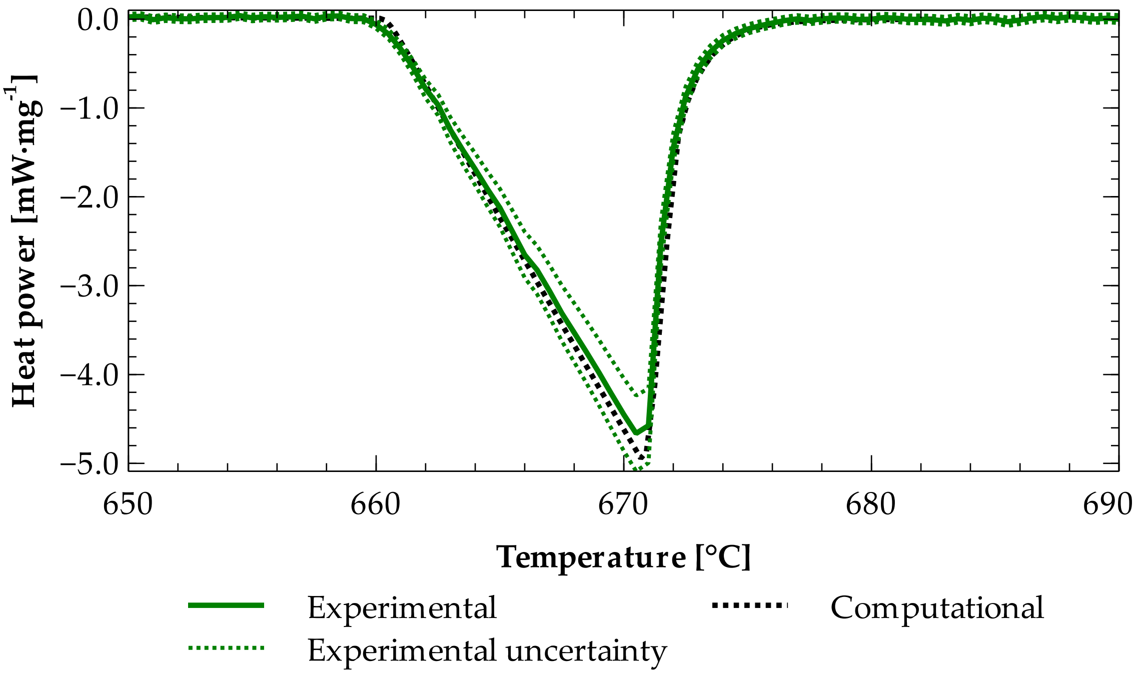

*Figure 4.20. Results of the model validation using the aluminum standard.*

Adjusting the effective specific heat capacity vs. temperature function of quartz, the experimental and computational outputs reached a satisfactory agreement as depicted in Fig. 4.21. The experimental output is provided with results of uncertainty analysis (dotted lines) and it can be observed, that the computational output was within this range. One can also notice that the computational output was smoother than the experimental which was given by the deterministic nature of results which were not affected by any experimental errors. This is one of the advantages of the developed model when compared to the real device.

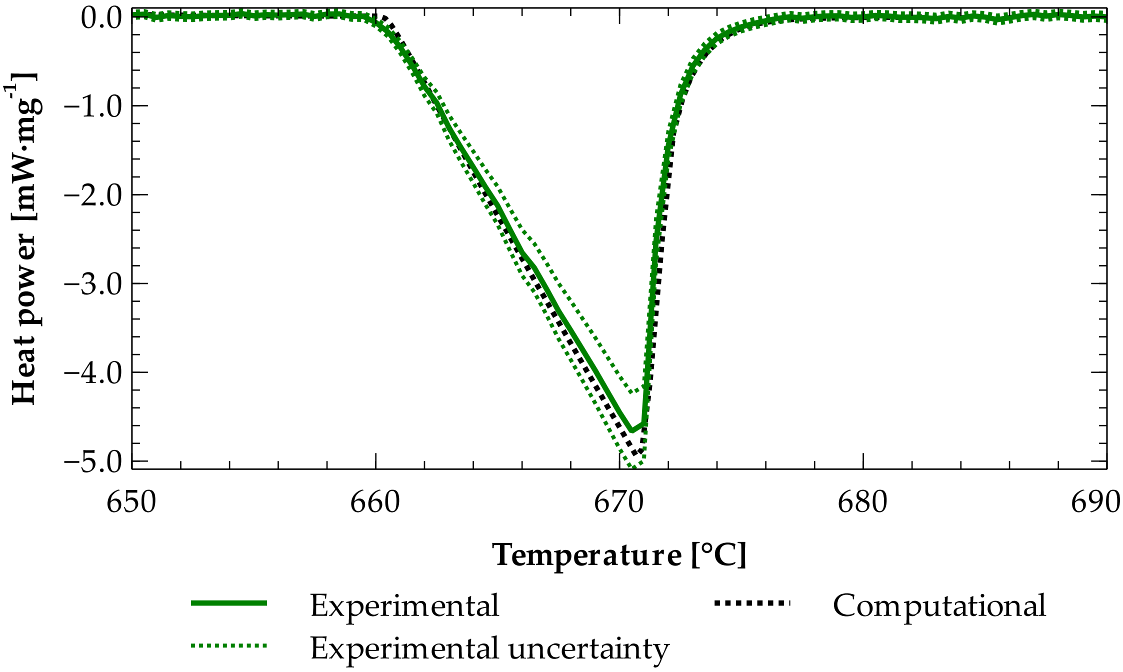

***Figure 4.21.*** *Results of model validation using quartz α-β transition.*

The effective specific heat capacity vs. temperature function applied to fit the experimental output is depicted in Fig. 4.22. Reaching 2550 J·kg$^{-1}$·K$^{-1}$, the top of the effective specific heat capacity peak is positioned at 573.45 °C. There are also results of other researchers included in Fig. 4.22, who investigated effective specific heat capacity of quartz. Hemingway (1987) carried out an analysis of thermodynamic properties of quartz and reported values of effective specific heat capacity between ~67 and 716 °C. A very good match with the results presented in this paper can be observed, even if the peak reached higher values, 4694 J·kg$^{-1}$·K$^{-1}$ or 3928 J·kg$^{-1}$·K$^{-1}$ at 572.75 °C, depending on the measurement series. The results presented by Chase (1998) are also in a very good agreement with the results presented in this paper obtained using the developed computational model. However, Chase (1998) did not investigate the effective specific heat capacity values in the phase change region, so only values for *α*- and *β*-quartz could be compared. Ghiorso et al. (1979) performed specific heat capacity measurements of tens of quartz samples originating from Clear Lake and Cinder Cone, California over the temperature range of 127 to 627 °C.

Similarly to Chase (1998), also Ghiorso et al. (1979) excluded the transition region. Anyway, their data was in a very good agreement with the results obtained in this paper despite of the slight differences for $\beta$-quartz. These differences could be ascribed to the natural origin of investigated samples which might contain some impurities. However, such investigation is beyond the scope of this thesis.

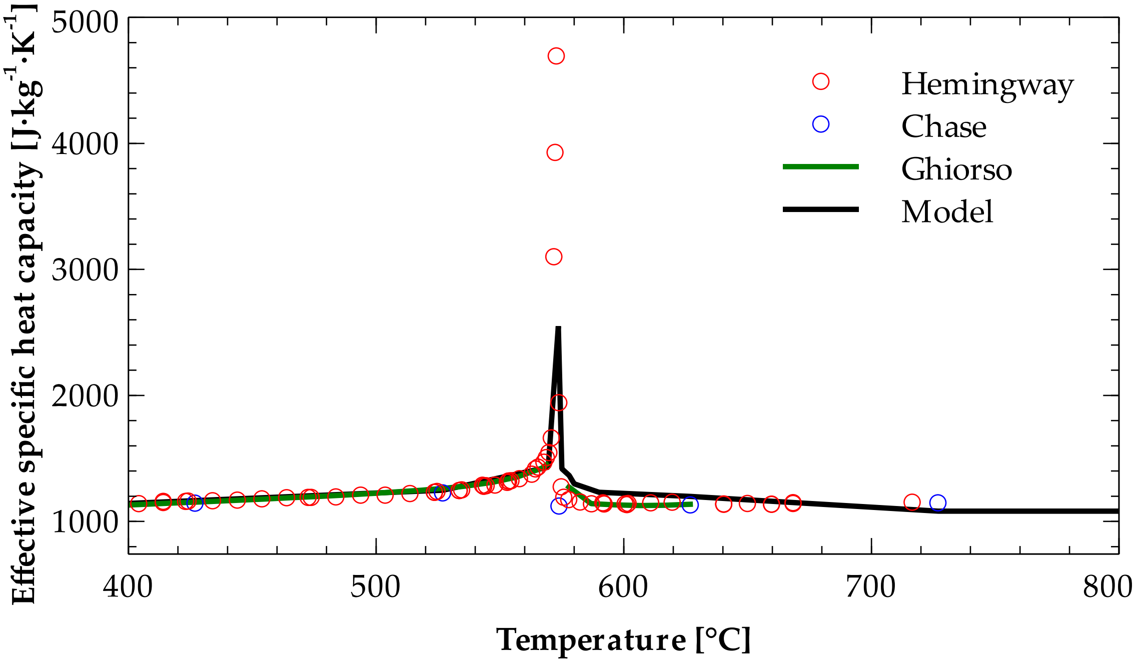

***Figure 4.22.*** *Effective specific heat capacity of quartz.*

Various values of the specific enthalpy of quartz ($H_{1000} - H_{298}$) have been reported in the literature: White (1919) 45.551 kJ·mol$^{-1}$, Wietzel (1921) 45.861 kJ·mol$^{-1}$, Roth and Bertram (1929) 44.727 kJ·mol$^{-1}$, Moser (1936) 44.968 kJ·mol$^{-1}$, Sinelnikov (1953) 45.250 kJ·mol$^{-1}$, Holm et al. (1967) 45.680 kJ·mol$^{-1}$, Ghiorso et al. (1979) 44.705 kJ·mol$^{-1}$, Richet et al. (1982) 45.579 kJ·mol$^{-1}$, or Hemingway (1987) 45.520 kJ·mol$^{-1}$. Integrating the effective specific heat capacity obtained by the computational model developed in this thesis between 298 and 1000 K resulted in the specific enthalpy of 760.297 kJ·kg$^{-1}$ which corresponded to 45.679 kJ·mol$^{-1}$. This value was within the range of specific enthalpy values reported above by the other researchers, which confirmed the proper function of the model.

# 5 Correction of Systematic Errors Using Computational Modelling

So far, two different calorimeters have been introduced in Section 3, being followed by the description of their computational representations that have been presented in Section 4. Once the models have been constructed, calibrated and validated, practical applications of theirs are enabled which is demonstrated in following subsections.

## 5.1 Assessment of fast heat evolving processes

The practical application of the model developed within the Section 4.1 is demonstrated in this subsection by means of an inverse analysis of calorimetric data recorded during a fast heat evolving process, which is typical for ongoing wet processes in building materials. In particular, most binders based on cement, lime, or gypsum generate substantial heat amounts immediately after mixing with water, which is mainly due to wetting, dissolution, or chemical reactions. As described in Section 3.1.2, these processes are barely detectable due to thermal inertia of calorimeters in the initial phase of the measurement.

### 5.1.1 Fast heat evolving processes in building materials engineering

Heat of wetting, which is evolved when water wets a surface of solid matter, is generally very small. However, it can reach significant values in case of binders with high specific surface. Besides the surface area, the amount of released heat depends also on the surface tension of liquid (water) or lyophobic/lyophilic properties of the surface that determine the contact angle. Since the total interface energy is released during wetting, the amount of heat is equal to the change of enthalpy. It is also important to realize that heat of wetting concerns even the insoluble substances. The amount of released wetting heat is higher in cases of mixtures containing fine-grained fillers or microfillers (Scrivener et al., 2015), and their setting may thus be affected (Xi, 2006).

Heat of dissolution represents another source participating on the fast heat evolution after mixing of binders with water. While breaking of bonds within the solute and within the solvent is an endothermic process, the formation of solute-solvent attractions is much more exothermic, so the overall process of dissolution releases a certain amount of heat (Grant, 2003).

Heat of dissolution is usually merged in with heat of wetting as it is practically impossible to use experimental techniques that can distinguish these two sources of heat. Regarding the fact that dissolution processes last longer than processes of wetting, depending on the dissolution/dissociation rate, heat of dissolution may be evolved over a slightly longer period and usually reaches higher values (Shi et al., 2006). However, in spot of global heat processes which occur in binders after mixing with water, these differences are usually not considered.

### 5.1.2 Negative impacts of heat evolution on building materials

The major part of heat is released by binders due to their reaction with water, which is an essential condition for the formation of solid mass with high strength. During the hydration process new products, such as calcium silicate hydrates, calcium aluminate hydrates, or calcium hydroxide, are formed. Reaching up to 500 $J \cdot g^{-1}$ (Snelson et al., 2008), the hydration heat is released slower than heat of wetting or dissolution. Depending on the type of binder and its composition, nevertheless, the heat may be evolved very fast at the early stage of hydration. This is typical, e.g., for gypsum, high-alumina cements, or calcium cements with rapid strength increase (Jansen et al., 2017; Madej et al., 2016).

In case of small-scale structures, such as beams, slabs or columns, the evolved heat dissipates rapidly. On the other hand, the dissipation is slow in massive constructions, which leads to increase of their internal temperature. This results in a substantial temperature gradient between the center and the surface of the mass, inducing thermal stress (Riding et al., 2006) that may even exceed the tensile strength of the material. Thermal cracks are formed subsequently in this case, being accompanied with other negative phenomena, such as reduction of integrity, penetration of various substances, or reduction of service life due to deterioration and corrosion (Mehta and Monteiro, 2006). Therefore, the heat evolving processes are supposed to be monitored before the particular building materials are used in a structure.

### 5.1.3 Methods for quantification of heat evolving processes

The application of calorimetric methods is very extensive in the research practice to quantify these processes. Isothermal calorimetry was used, e.g., by Maheswaran et al. (2016) for a description of hydration kinetics of two types of blended cement at early stage, or by Gu et al. (2016) for investigations of the influence of modified $SiO_2$ nanoparticles on cement hydration at early age. Semi-adiabatic calorimeters were utilized, e.g., by Kong et al. (2016) analyzing the influence of various types of superplasticizers on hydration properties of Portland cement, or Saeed et al. (2016) who tried to quantify the amount of hydration heat of Portland cement with slag and find a link to cracking of concrete blocks. The extensive utilization of calorimetry in relation to cement products can be proven by a number of records in the Web of Science database which provides about two thousand publications based on that search pattern.

Anyway, due to the drawbacks described in Section 3.1.2, computation modelling technique seems to be more efficient tool for this kind of quantification as it is able to deal with the thermal inertia issue. The computational model for the assessment of fast heat evolving processes, described in Section 4.1, is therefore applied for an inverse analysis of transient heat transport phenomena in the calorimeter. The designed procedure utilizes the computational model of heat transport and storage processes in large-volume isothermal heat flow calorimeter which makes possible to calculate temperature fields in the calorimeter-sample system using a three dimensional computational representation of the real device. The proposed computational solution of the inverse problem of heat transport inside the calorimeter can reconstruct any heat evolving process, no matter how fast or intensive, based on experimental outputs which include systematic errors of the known origin. In other words, using the computational modeling it is possible to find such a source heat power vs. time function that generates the same output as the real apparatus. It can be then considered as more precise than the experimental result because it is not distorted by imperfections related to the measurement techniques, such as the heat consumption by device components and signal delay.

### 5.1.4 Principles of the inverse analysis

The main objective of the inverse analysis was to find the heat power vs. time function, $P(t)$, that (after application in the computational model as an input parameter) produced the computer simulated function, $P_x(t)$, which was (within the prescribed limits) the same as the experimentally determined function, $P_e(t)$. The basic scheme of the process of identification of the unknown $P(t)$ function is given in Fig. 5.1.

In the inverse analysis, genetic algorithms were used. This soft computing technique has become very popular over the last decades because of its applicability for a wide range of research tasks in a combination with the ability to produce satisfactory results. Principles of genetic algorithms follow the processes related to living species evolution. It means that by the use of genetic operators, populations in which individuals represent candidate solutions of the sought problem, are evolved in a series of generations toward better solutions. The best solutions can be therefore found much faster than in cases when empirical approaches or trial-and-error methods would be utilized. A detailed description of genetic algorithm techniques was given by Holland (1962). A practical application in the field of materials engineering was demonstrated by Kočí et al. (2016b), who used it for the identification of moisture transport parameters of porous building materials. The flowchart describing the inverse analysis in detail is given in Fig. 5.2.

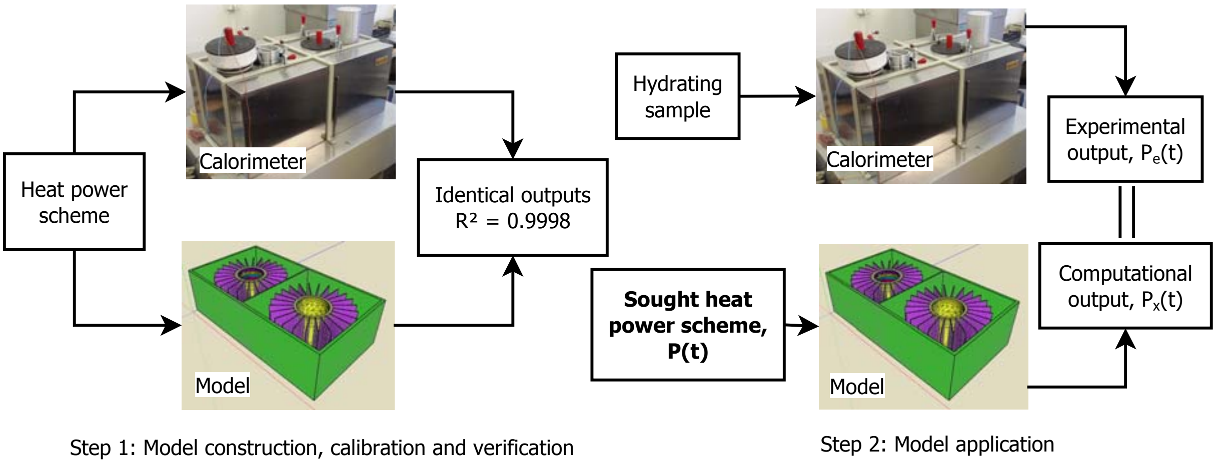

***Figure 5.1.*** *Scheme of identification of unknown heat power vs. time function.*

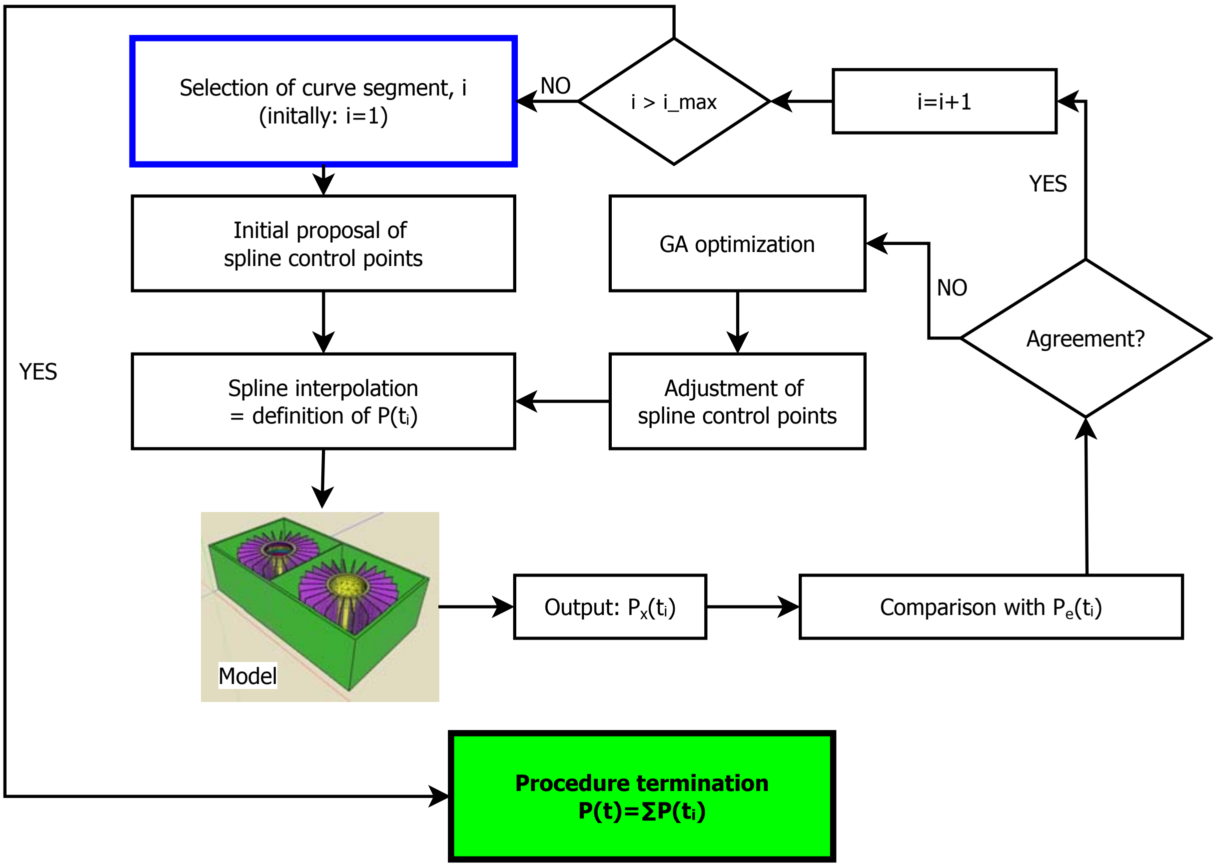

***Figure 5.2.*** *Flowchart of the inverse analysis procedure.*

The inverse problem solution procedure exploited cubic spline curves for smoothing both experimental and simulated heat power vs. time functions. It allowed the control points of the functions to be sought separately instead of all values corresponding to each time step of computations. By the words of genetic algorithms terminology, this measure significantly reduced the size of the population, i.e., the number of unknowns. The seeking procedure was thus much faster. Interlaying values between the control points could be then easily calculated from the analytical expressions of the particular spline segments.

### 5.1.5 Studied fast heat evolving processes

Two different fast heat evolving processes were chosen to demonstrate the practical applicability of the developed computational method for an enhanced assessment of experimental data produced by isothermal calorimeters.

The lime hydrate-water system can be characterized by a fast but relatively simple heat generation process, including only the heat of wetting and heat of dissolution of $Ca(OH)_2$ (Jerman et al., 2016). The Portland cement-water system, on the other hand, presents a more complex case because the heat generation is caused here by several cement components having very different rates of hydration (Černý and

Rovnaníková, 2002). $C_3A$ reacts with water in the fastest way, within the time period of several minutes, although in Portland cement its reaction rate is somewhat reduced by the presence of gypsum. The most significant heat generation at the hydration of $C_3S$ occurs within the range of 10-20 hours, and the reaction of other compounds, such as $C_4AF$ and $C_2S$, with water is even slower.

In the computational analyses, the experimental heat generation curves measured using the large volume isothermal heat flow calorimeter were utilized. Namely, the reactions of CL90-S lime hydrate and CEM I 42.5 R Portland cement with water measured by Jerman et al. (2016) and Tydlitát et al. (2012b), respectively, were analyzed.

### 5.1.6 Results of the inverse analyses

#### 5.1.6.1 Lime hydrate

Fig. 5.3 shows the results of computational reconstruction of the cumulative amount of heat released after mixing lime hydrate with water (the ideal state without heat inertia) in a comparison with the data obtained in the large-volume experiment (affected by the internal heat inertia). The highest differences between the original- and computationally corrected data, up to 2 $J \cdot g^{-1}$, were observed within the first hour of heat evolution; after 7 h the differences were already very small, virtually negligible. The total heat evolved was relatively small, reaching 9.5 $J \cdot g^{-1}$ after 33 h.

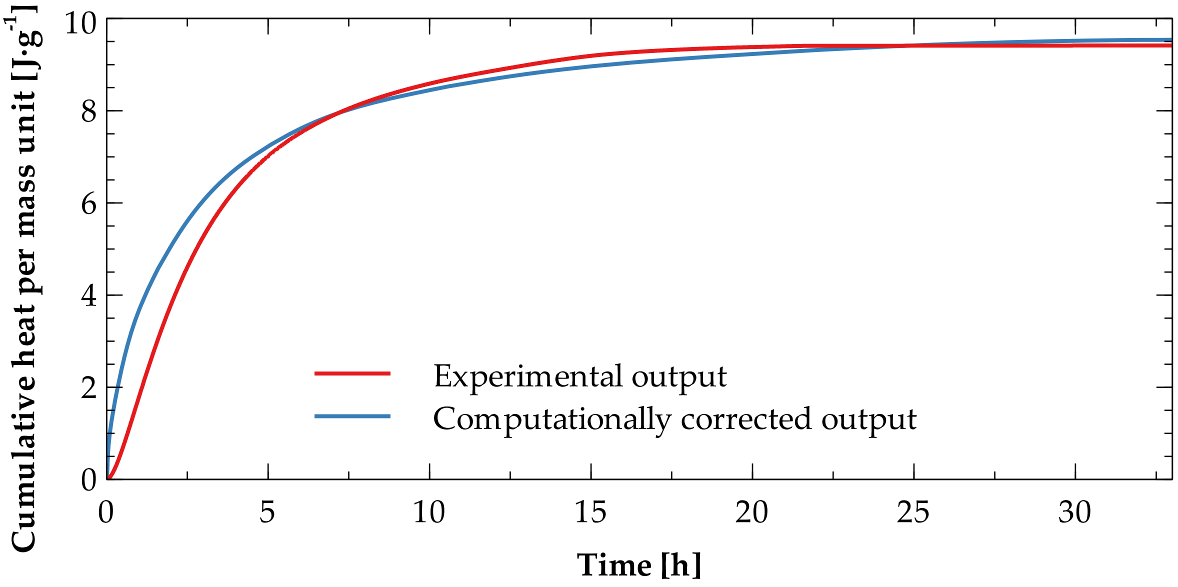

*__Figure 5.3.__ Cumulative heat amount evolved per unit mass in the lime hydrate-water system.*

The heat power vs. time curves captured in Fig. 5.4 illustrate the importance of the computational assessment of experimental data in a more detailed way. Apparently, while in the calorimetric experiment the peak heat power value of 0.64 mW·g$^{-1}$ was observed at 2760 s, in the computational reconstruction it was 4.45 mW·g$^{-1}$ at 120 s. The maximum heat power of the ongoing processes in the lime hydrate-water system could thus be more than seven times higher than detected using the experimental device for large volume applications.

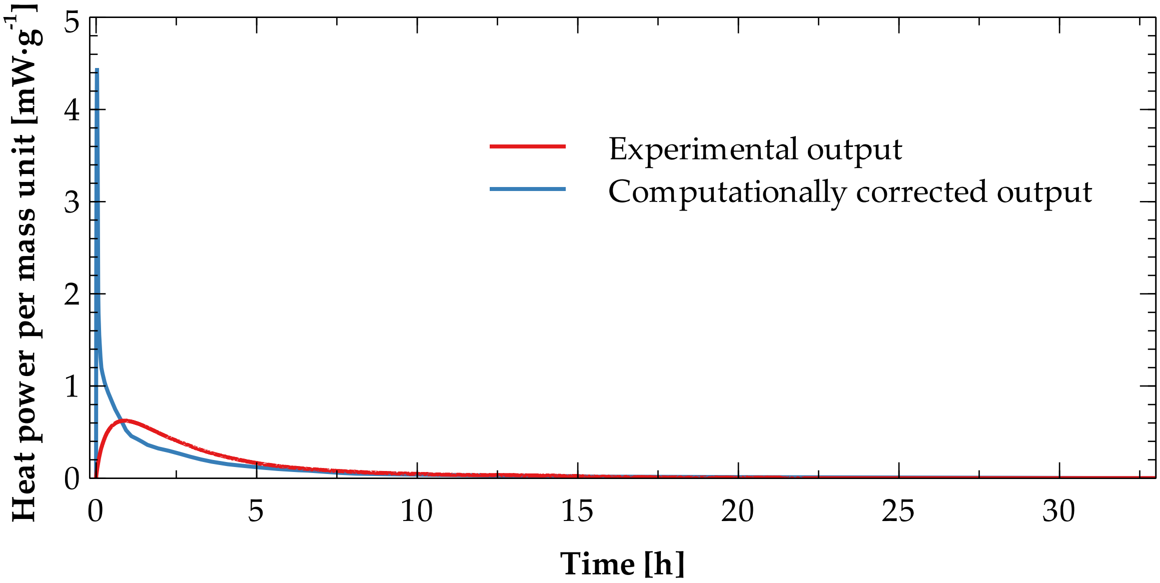

***Figure 5.4.*** *Heat power evolved per unit mass in the lime hydrate-water system.*

In order to verify the results obtained by the computational reconstruction of measured calorimetric data, the calculated time development of heat power (the ideal state without heat inertia) given in Fig. 5.4 was used as input parameter of the computer simulation tool for modeling heat transport and storage processes occurring in the calorimeter. The computational analog of the real experimental output (including the internal heat inertia effects) is presented in Fig. 5.5. Apparently, the agreement of computational and experimental data was very good, with $R^2$=0.9984.

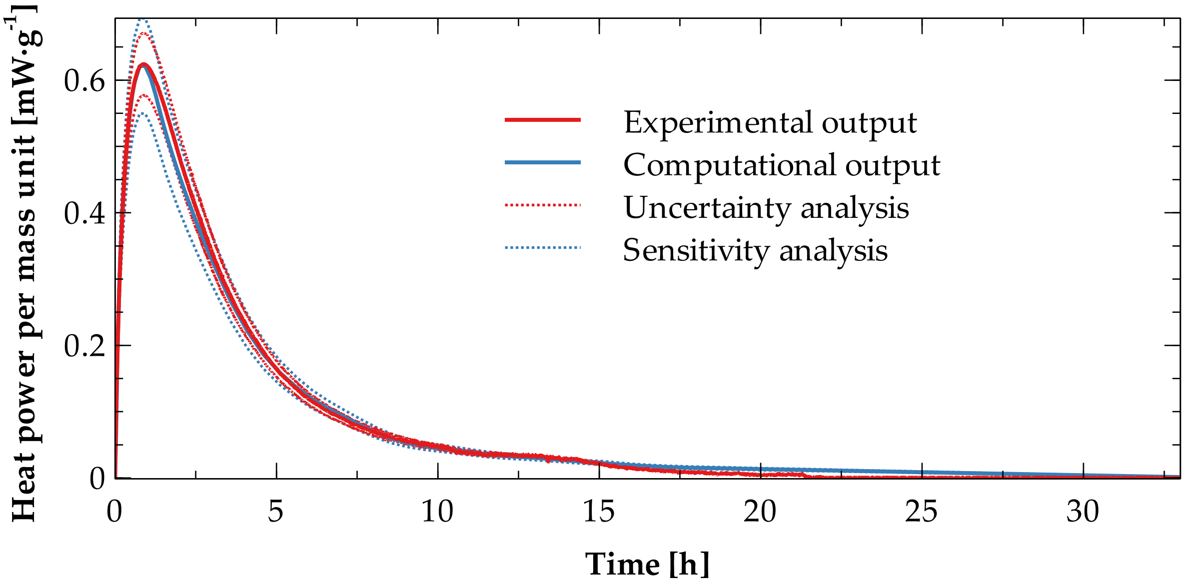

***Figure 5.5.*** *Heat power evolved per unit mass in the lime hydrate-water system: Comparison of experimental and computational results.*

For a more detailed assessment of the developed computational method, an additional analysis of its accuracy was done. The experimental results obtained from Jerman et al. (2016) were provided with an uncertainty analysis (which was not included in the original paper); it was carried out in compliance with ISO/EIC 98-3, known as GUM (ISO/EIC 98-3, 2008), providing the relative uncertainty of 7.51 %. The computational results, on the other hand, were complemented with the results of sensitivity analysis of the computer simulation tool for modeling the heat transport and storage processes occurring in the calorimeter; it was done in accordance with the procedure described by Kočí et al. (2017). The sensitivity analysis revealed that the computationally modelled results may differ up to 11.56 %. Fig. 5.5 shows that the sensitivity range of computational data covered well the experimental outputs over the whole studied time period and, similarly, the computational outputs were within the uncertainty range of experimental data. This further confirmed the suitability of the developed computational method for the enhanced assessment of experimental data produced by isothermal calorimeters.

The heat of wetting and heat of dissolution of $Ca(OH)_2$ in the lime hydrate-water system were generated so fast that even after the computational reconstruction (see Fig. 5.4) they were merged into one initial heat power peak. Nevertheless, it should be noted that the knowledge of the overall amount of the heat evolved presents a useful practical outcome anyway, regardless of its particular constituents. Most researchers therefore did not try to distinguish these two different heat sources until now (Madej et al., 2016; Xu et al., 2015), but few exceptions can be found. For instance

Jerman et al. (2016) numerically distinguished heat of wetting and heat of hydration of ceramic powder, Tydlitát et al. (2012a) used the same method for the separation of hydration heats of $\beta$-calcium sulfate anhydrite III and $\beta$-hemihydrate in the mixture. However, the method used in the mentioned research papers is conditioned by the time sequence of the analyzed processes. Another possibility would be based on the application of Young equation and extraction of heat of wetting. Since it is equal to the change of enthalpy, it can be expressed as

$$\Delta_{\mathrm{w}} H = A \cdot \left[ T \cdot \cos\theta \cdot \left( \frac{\partial \gamma_{\mathrm{lg}}}{\partial T} \right)_{A,p} + T \cdot \gamma_{\mathrm{lg}} \cdot \left( \frac{\partial \cos\theta}{\partial T} \right)_{A,p} - \gamma_{\mathrm{lg}} \times \cos\theta \right] \tag{5.1}$$

where $\Delta_{\mathrm{w}}H$ [J] is the change of enthalpy due to wetting, $A$ [m$^2$] is the area of wetted surface, $T$ [K] is the temperature, $\gamma_{\mathrm{lg}}$ [N·m$^{-1}$] is the surface tension of the liquid, and $\theta$ [-] is the experimentally determined contact angle.

#### 5.1.6.2 Portland cement

Fig. 5.6 presents the computational reconstruction (the ideal state without heat inertia) of the heat power evolved per unit mass in the Portland cement-water system in a comparison with the experimental data obtained in calorimetric measurements (including the internal heat inertia effects).

The fast heat evolving processes within the first minutes can be assigned to the heat of wetting, rapid dissolution of $C_3S$ and $C_3A$, and hydration of free lime (Černý and Rovnaníková, 2002). According to Bensted (1987), also the heat of formation of ettringite may contribute to the initial peak. The experimental output presented in Fig. 5.6 shows that the initial peak was observed at 1680 s and the heat power was only 2.3 mW·g$^{-1}$ here, which was even less than the major heat power peak that corresponded to the hydration of $C_3S$. The computational reconstruction of the initial heat generation process provided much higher value, 27.6 mW·g$^{-1}$ at 120 s.

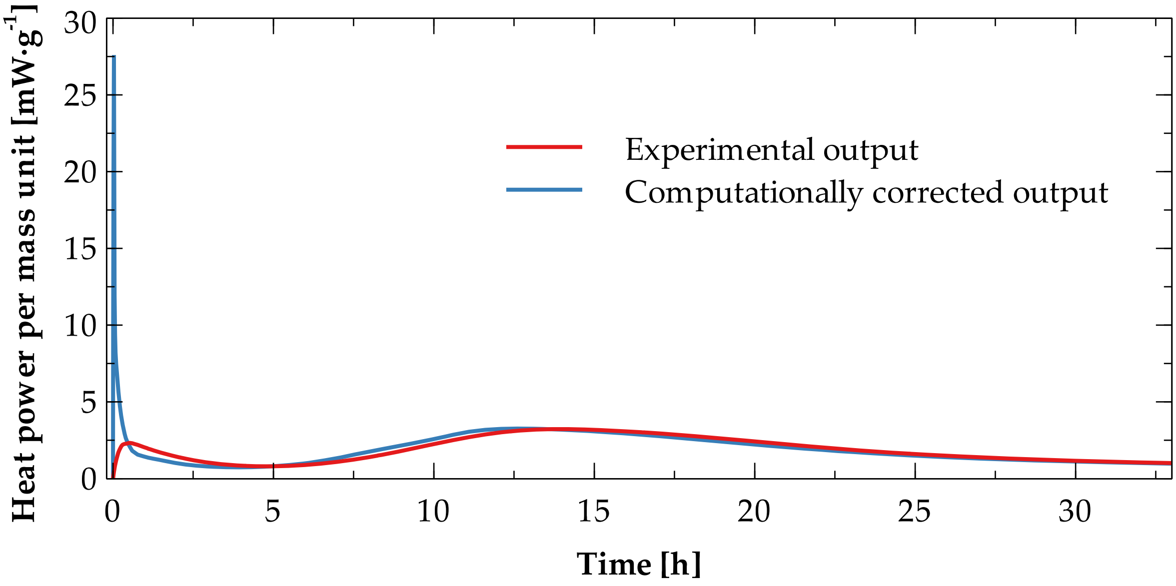

*Figure 5.6. Heat power evolved per unit mass in the Portland cement-water system.*

The results of uncertainty analysis of experimental data and sensitivity analysis of their computational counterparts (obtained after the calculated heat power curve in Fig. 5.6 was applied as input parameter of the model), which was done using the same methods as in the case of the lime hydrate-water system in Section 5.1.6.1, are presented in Fig. 5.7. The average difference between the measured and calculated values was $5.07 \times 10^{-4}$ mW·g$^{-1}$, providing a very good $R^2$ of 0.9992.

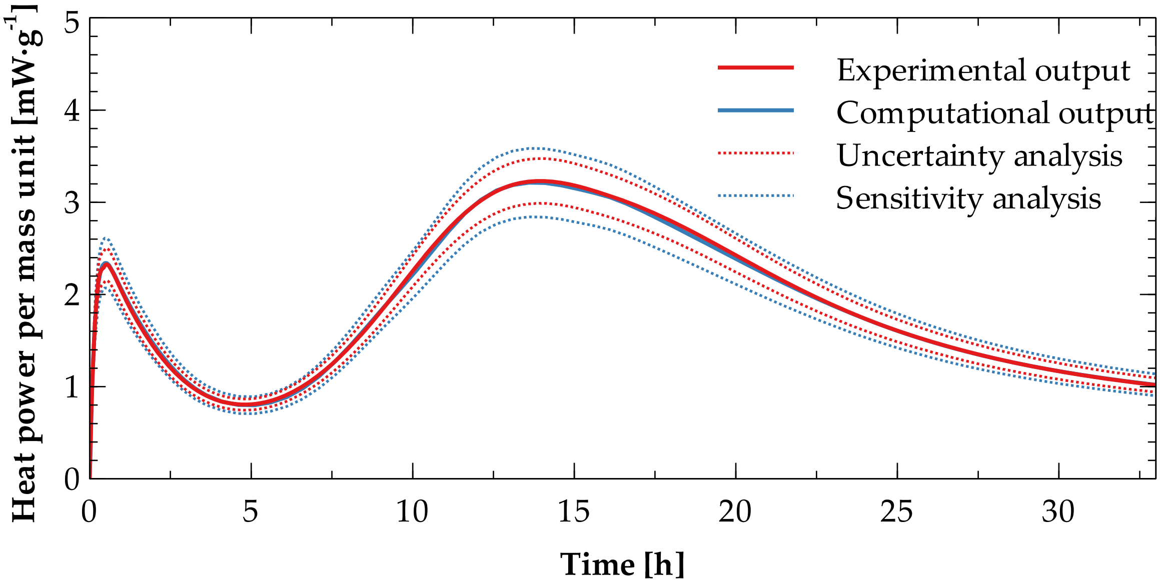

*Figure 5.7. Heat power evolved per unit mass in the Portland cement-water system: comparison of experimental and computational results.*

The cumulative amount of heat released after mixing Portland cement with water is shown in Fig. 5.8. Comparing the experimental and computational results, it is obvious that the disadvantages of the large volume calorimetry were eliminated approximately after 30 hours when both functions became almost identical. The differences observed for earlier times were though relatively high, up to 10.1 J·g$^{-1}$, which further confirmed the usefulness of the applied computational corrections.

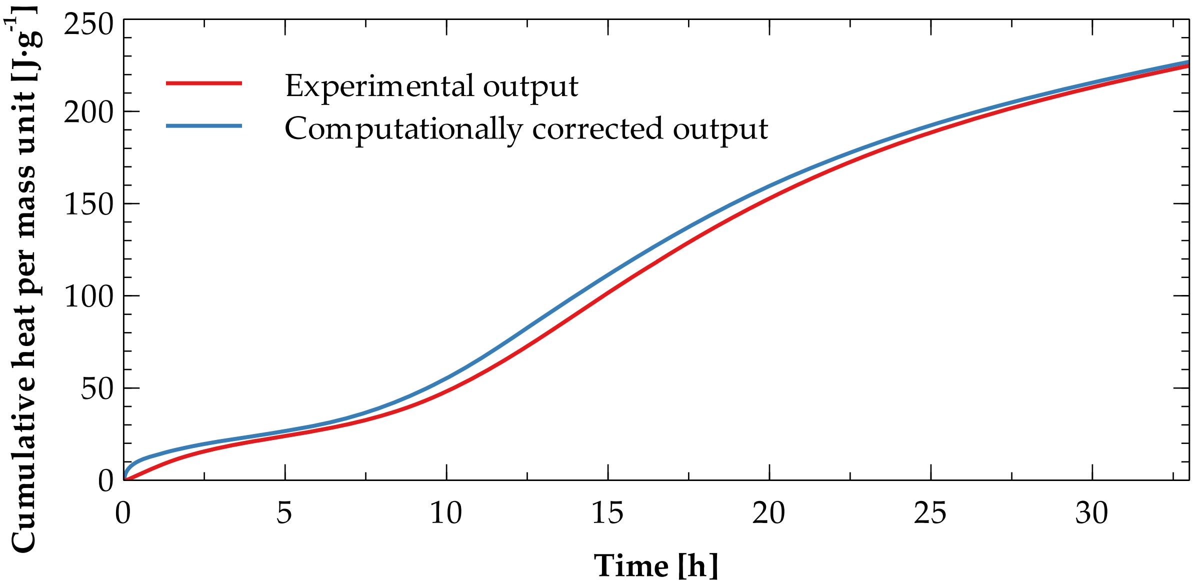

***Figure 5.8.*** *Cumulative heat amount evolved per unit mass in the Portland cement-water system.*

According to the measurement performed for CEM I 42.5 R Portland cement using a small-volume isothermal heat flow calorimeter, see Tydlitát et al. (2012b), the initial heat power peak reached 21 mW·g$^{-1}$. Duong Dinh et al. (2016) reported that the initial heat power peak of Portland cement, as measured by a TAM Air device, can reach 23 mW·g$^{-1}$. They noted though that the results within the first 5 minutes were affected by uncertainties due to the small difference in temperatures between the ambient conditions and inside the calorimeter, which required some finite equilibration time. Additionally, there was a small delay required to introduce the sample into the calorimeter that may have caused a certain heat leak. In the light of the above mentioned findings, the value of 27.6 mW·g$^{-1}$ reported in this paper can be considered as realistic, regarding the ability of the applied computational technique to filter out the experimental inaccuracies reported by Tydlitát et al. (2012b) and Duong Ding et al. (2016).

The calculated heat power in later phases of the Portland cement hydration process corresponded to the results of experimental measurement, except for a slight time delay (see Fig. 5.6). Since a thermal equilibrium was already reached at this moment, most calorimetric methods are able to provide precise data, irrespective of the calorimeter type. The value of the major heat power peak obtained in this paper, 3.3 mW·g$^{-1}$, was in conformity with other researchers, regarding the specifics of their investigations. For instance, Rahhal and Talero (2005) reported the major heat power peak of Portland cement of 3.3 mW·g$^{-1}$, Alhozaimy et al. (2015) measured for concrete mixes based on Portland cement 3.3 – 4.0 mW·g$^{-1}$, depending on the mixture composition.

## 5.2 Elimination of experimental setup influence on calorimetric outputs

This sections follows up the previous parts of this thesis in which the exact computational replica of the real DSC device was developed, i.e., constructed, calibrated and validated using various metal standards (see Section 4.2). Since such a model takes into account the heat storage and transport properties of materials involved in the system and calculates the real temperature distribution, it is supposed to be independent of externalities, such as heating rate or sample size which represent the most common sources of systematic errors. The model is therefore able to identify real thermal processes inside the device, thus filter out the errors from experimental outputs. In the presented analysis, practical benefits of the model are demonstrated by testing various masses of a real sample exposed to different heating rates. Comparing raw and corrected data, the validated model is exploited to identify an optimal experimental setup (heating rate, sample mass) that produces outputs with the lowest experimental errors.

### 5.2.1 Experimental setups investigated

In the experimental work, the influence of heating rate and sample size was investigated. After the experimental calibration of the device for particular heating rates had been done (see Section 4.2.2.1), the rates of 3 K·min$^{-1}$, 7 K·min$^{-1}$ and 10 K·min$^{-1}$ were applied on the sample analyzed. The sample sizes were chosen to fill in different volume of the crucible, namely one quarter, one half, and three quarters. They are labeled as Q1, Q2 and Q3, respectively, in what follows.

At the same time, the identical experimental setups were processed using the computational model described in Section 4.2.

The experimental and computational results obtained for different heating rates and sample masses, namely effective specific heat capacity and enthalpy of the reaction for particular experimental setups, were evaluated, discussed and compared with findings reported by other investigators. Based on that, the most appropriate experimental setup was recommended and the corresponding material properties were used to calculate corrected heat power curves for each combination of heating rate and sample mass. In this case, the temperatures were though not recorded on the thermocouples, but directly inside the sample which eliminated the signal delay. The flowchart of the whole procedure is given in Fig. 5.9.

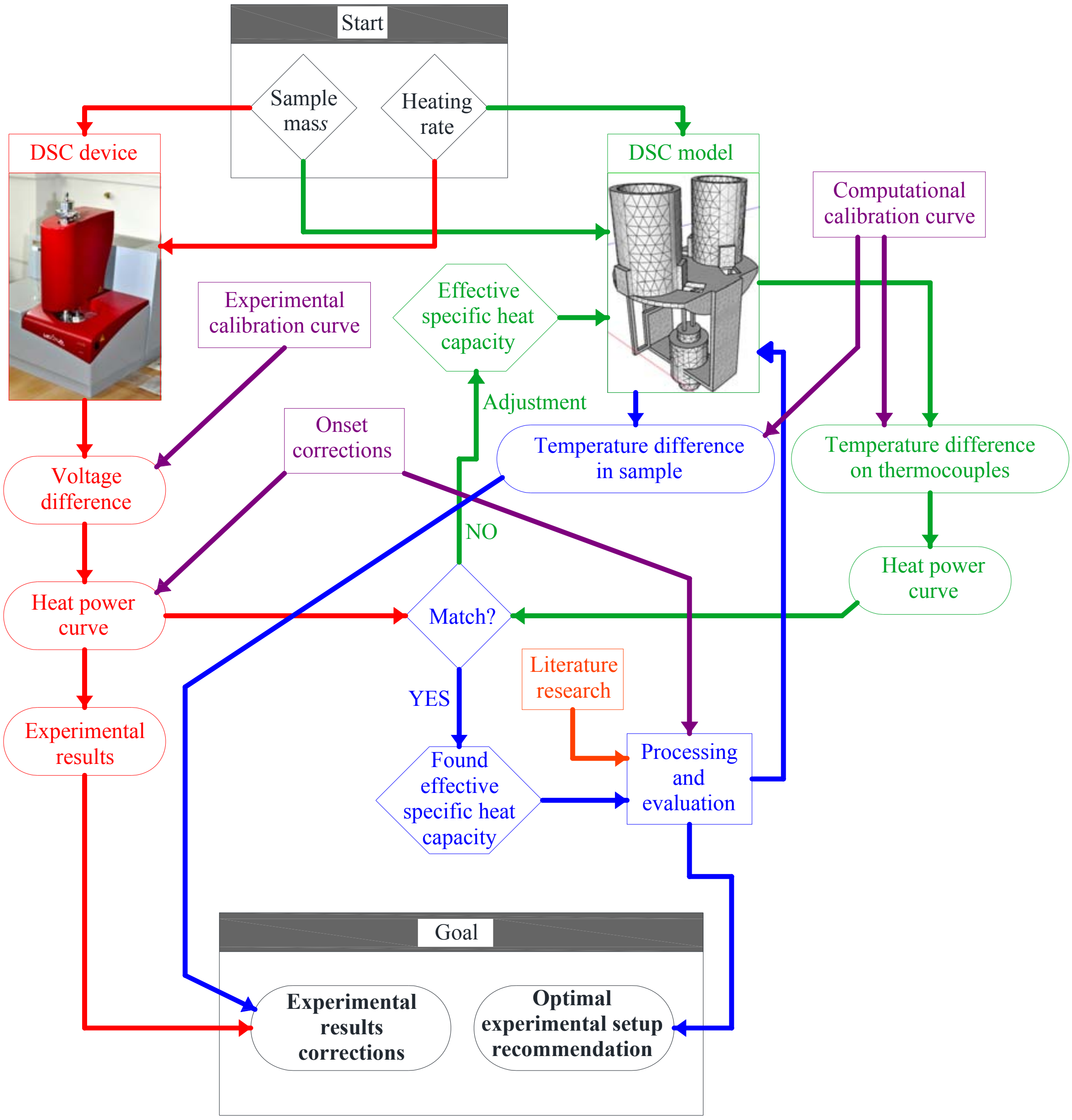

***Figure 5.9.*** *Flowchart of the procedure for the most appropriate setup identification and DSC results corrections.*

### 5.2.2 Analyzed material

A commercially produced CL90-S lime hydrate, $Ca(OH)_2$, was used to illustrate the practical application of the computational method for the correction of systematic errors in DSC measurements. Its Blaine specific surface was 1374 $m^2 \cdot kg^{-1}$, $d_{50}$ was equal to 8.1 μm, and the loose bulk density of the sample in the crucible was 529 kg·m$^{-3}$. The chemical composition of the lime hydrate obtained using the X-ray fluorescence method (Jerman et al., 2016) is given in Tab. 5.1. The particular sample masses were 11.3 mg (Q1), 26.5 mg (Q2), and 41.6 mg (Q3). The thermal decomposition range of $Ca(OH)_2$ is supposed to be within 420 – 510 °C (Zelic et al., 2002).

***Table 5.1.*** *Chemical composition of the lime hydrate.*

| $SiO_2$ | $Al_2O_3$ | $Fe_2O_3$ | CaO | MgO | $K_2O$ | $Na_2O$ | $TiO_2$ | $SO_3$ |
|---|---|---|---|---|---|---|---|---|
| 0.0 | 0.0 | 0.0 | 99.3 | 0.5 | 0.0 | 0.0 | 0.0 | 0.1 |

### 5.2.3 Results of the methodology applied

#### 5.2.3.1 Experimental results

The summary of experimental analyses of thermal decomposition of lime hydrate is given in Fig. 5.10, showing specific heat power as a function of temperature for particular experimental setups. For a better comprehensibility, the axis ranges are kept constant (from 350 to 600 °C and from -5.0 to 0.5 mW·mg$^{-1}$), regardless of values obtained. Such an imaging helps to recognize shifts and values variations that occurred for particular setups. The results in the left column of Fig. 5.10 show the influence of heating rate at given sample mass, while the results on the right column present the effect of different sample mass at given heating rate. All the experimental results are provided with the measurement accuracy analysis (dashed lines). The errors were expressed during the experimental calibration procedure of the device when an experimental calibration function curve as a function of temperature was plotted to convert measured voltage to heat power. Comparing the theoretical values of calibration standards with those obtained experimentally (see Tab. 4.7), one can determine the relative measurement error at a given temperature as (5.2)

$$E = \left(0.0001T + 0.0155\right) \cdot 100\%, \tag{5.2}$$

where $T$ [°C] is the temperature. It means, in the temperature range of 350 – 600 °C applied within this investigation, it accounts for less than 8 %.

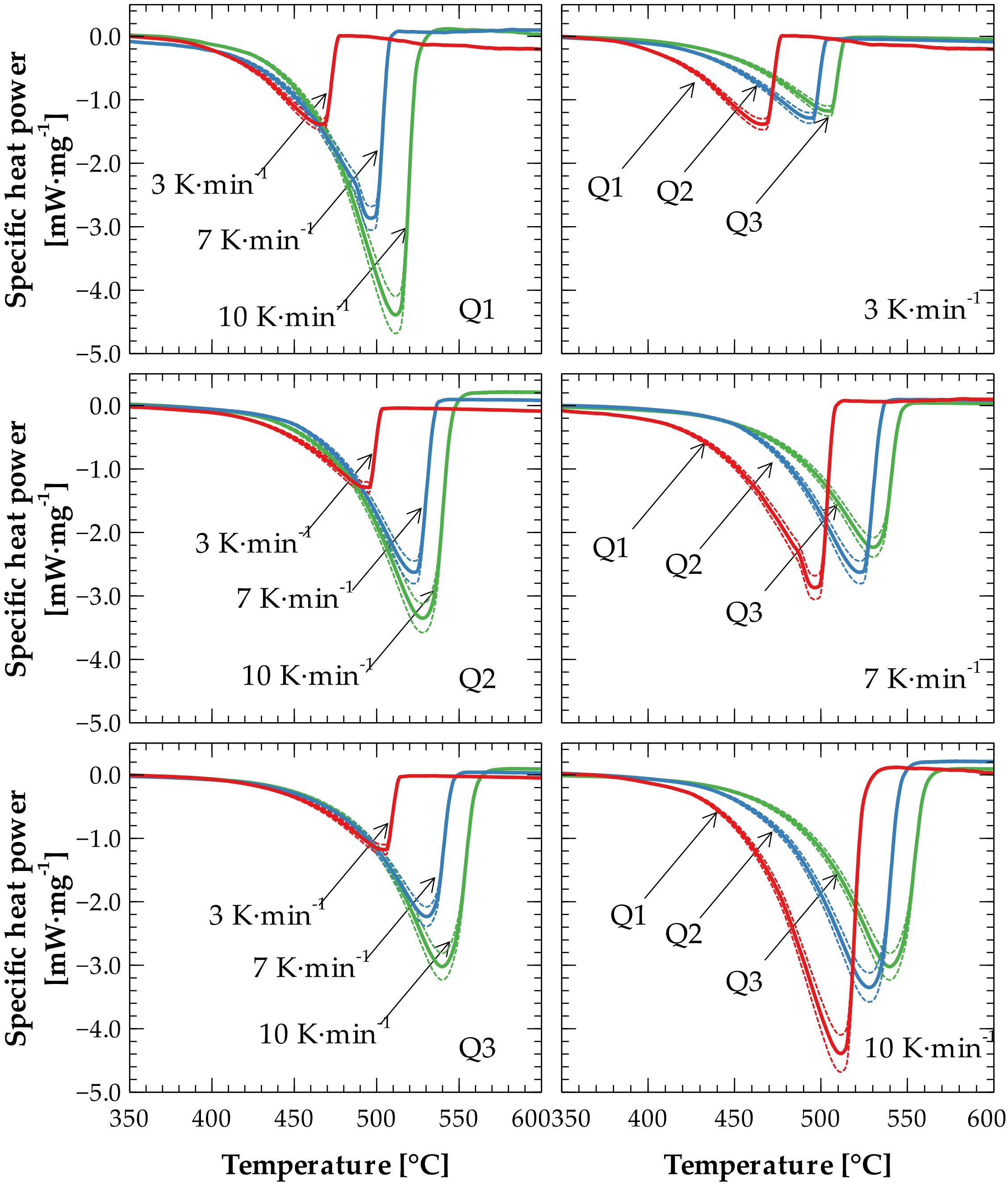

***Figure 5.10.*** *Experimental analysis of thermal decomposition of lime hydrate: left column – the influence of heating rate at given sample mass, right column – the influence of sample size at given sample mass, dashed lines – results of measurement accuracy analysis.*

As it was expected, higher heating rates shifted the peak tops to the right side along the temperature axis. Together with the peak shifting, the peak top values were increased as well. In case of sample that filled approximately one quarter of the crucible (Q1), the peak top temperature was shifted from 466.5 up to 511.5 °C depending on the heating rate, while its absolute value increased from 1.385 up to 4.390 mW·mg$^{-1}$. The same scenarios were observed also in case of Q2 and Q3 samples. Here, the peak top temperature was shifted from 495.0 to 528.0 °C and from 505.5 to 540.0 °C, respectively. The corresponding peak top values increased from 1.292 to 3.349 mW·mg$^{-1}$ and from 1.181 to 3.022 mW·mg$^{-1}$, respectively. The detected specific heat power thus differed by up to ~217 % when compared with the results obtained for the heating rate of 3 K·min$^{-1}$. The temperature shifts could be observed also in case of different sample masses, but the peak top values were decreasing with the increasing mass. The numerical summary is given in Tab. 5.2.

***Table 5.2.*** *Experimentally determined heat power of lime hydrate decomposition process at various sample mass and heating rate.*

| Heating rate [K·min$^{-1}$] | Peak top [mW·mg$^{-1}$] | | | Peak top temperature [°C] | | |
|---|---|---|---|---|---|---|
| | Q1 | Q2 | Q3 | Q1 | Q2 | Q3 |
| 3 | -1.385 ± 0.086 | -1.292 ± 0.084 | -1.181 ± 0.078 | 466.5 | 495.0 | 505.5 |
| 7 | -2.869 ± 0.187 | -2.627 ± 0.178 | -2.234 ± 0.153 | 496.5 | 522.0 | 530.0 |
| 10 | -4.390 ± 0.293 | -3.349 ± 0.229 | -3.022 ± 0.210 | 511.5 | 528.0 | 540.0 |

The behavior of the DSC device observed at the experimental investigation of thermal decomposition of lime hydrate, summarized in Fig. 5.10 and Table 5.2, is in an agreement with other researchers who used DSC devices for investigation of various materials. Dumas et al. (2014) showed that a heat power peak, corresponding to melting of ice, may reach ~2.75 higher values when heating rate is increased from 2 to 15 K·min$^{-1}$. Barz and Sommer (2018) reported heat power of melting/cooling of high density polyethylene to be up to four times higher when heating rates of 0.5 and 10 K·min$^{-1}$ were compared. Besides a peak top value change, Saeed et al. (2016) pointed out at shifting along the temperature axis which occurred when either sample mass or heating rate was increased. Studying fatty acids as phase change materials they reported increasing of melting temperatures with increasing sample mass and heating rate, which was the same DSC behavior as in this paper. Similar shifting based on the heating rate demonstrated Lager et al. (2018) who investigated $Ca(OH)_2$ decomposition at 2, 5 and 10 K·min$^{-1}$ and reported similar values of final temperatures of decomposition.

The observed peak shifting could be attributed to heat capacity of tested samples that were exposed to elevated temperatures. Since the thermocouples that were supposed to record the sample temperature were not directly in the sample, various heating rates led to various signal delays. Even if the heating rates were considered in the experimental calibration procedure, they were subsequently used mainly for corrections of onset temperatures, which can be confirmed by the curves alignment showed in Fig. 5.10 (left column). Different sample masses changed the heat capacity of the system even more, being not considered within the experimental calibration procedure at all. Additionally, the calibration standards (metals) had lower specific heat capacity than the lime hydrate analyzed in this paper. In a combination with the small volume of metals due to their high density, the temperature distribution in the crucible during real experiments was, apparently, far from that at the calibration. The measurements thus always resulted in substantial errors that affected the quality of obtained data.

Besides the differences detected in specific heat power due to the above mentioned errors, also the experimentally obtained specific enthalpy $H$ [J·g$^{-1}$] of the thermal decomposition of lime hydrate was substantially affected by the selection of setup parameters. The $H$ values determined according to Eq. (5.3),

$$H = \int_{t_{\mathrm{onset}}}^{t_{\mathrm{offset}}} P(t)\,\mathrm{d}t \tag{5.3}$$

where $P(t)$ [mW·mg$^{-1}$] is the specific heat power as a function of time, and $t_{\mathrm{onset}}/t_{\mathrm{offset}}$ [s] is the onset/offset time of the decomposition peak, are given in Fig. 5.11.

Apparently, consistent $H$ values were not obtained even though this reaction parameter must be independent on the heating rate as well as on the sample mass. According to the results presented in Fig. 5.11, the measured data differed up to 332 J·g$^{-1}$ at given heating rate or up to 126 J·g$^{-1}$ at given sample mass. In a comparison with the results obtained by other investigators (Azpiazu et al., 2003; Felderhoff et al., 2013; Lander, 1951; Schaube et al., 2012; Schmidt et al., 2014), who reported the reaction enthalpy of $Ca(OH)_2$ decomposition within the range of 94.6 – 104.2 kJ·mol$^{-1}$, i.e., 1276 – 1474 J·g$^{-1}$, the $H$ values of 946 to 1278 J·g$^{-1}$ obtained experimentally in this paper were lower. Therefore, it could be concluded that a part of heat was consumed by the system which subsequently led to results distortion.

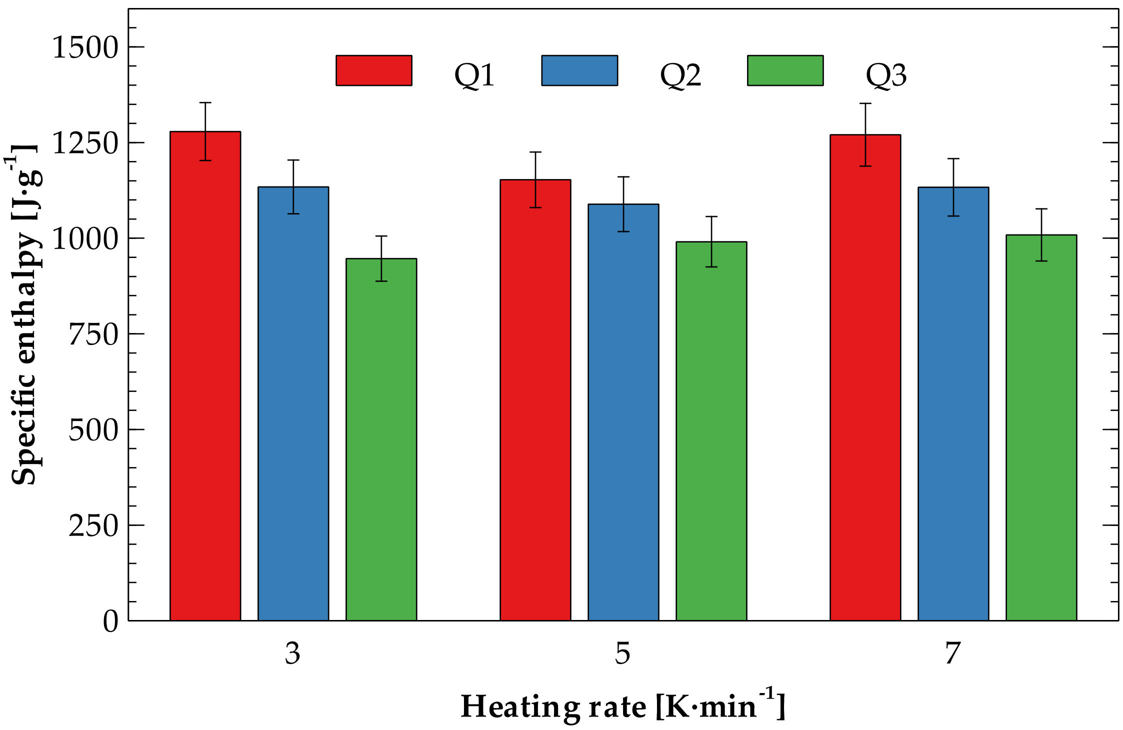

***Figure 5.11.*** *Specific enthalpy of thermal decomposition of lime hydrate as a function of heating rate and sample mass.*

#### 5.2.3.2 Computational results and identification of the most appropriate experimental setup

Fig. 5.12 shows that the computational model was able to reproduce well the experimental data. Despite the fact that there were certain differences between the experimental and the computational outputs, the applicability of the model for the analyzed system was confirmed as these differences were within the measurement error limits. The effective specific heat capacity of the lime hydrate decomposition process, $c_{eff}$, identified by the computational model for particular experimental setups is given in Fig. 5.12 as well. Apparently, the $c_{eff}(T)$ functions were shifted although they were not supposed to be, which indicated some experimental setups were not appropriate.

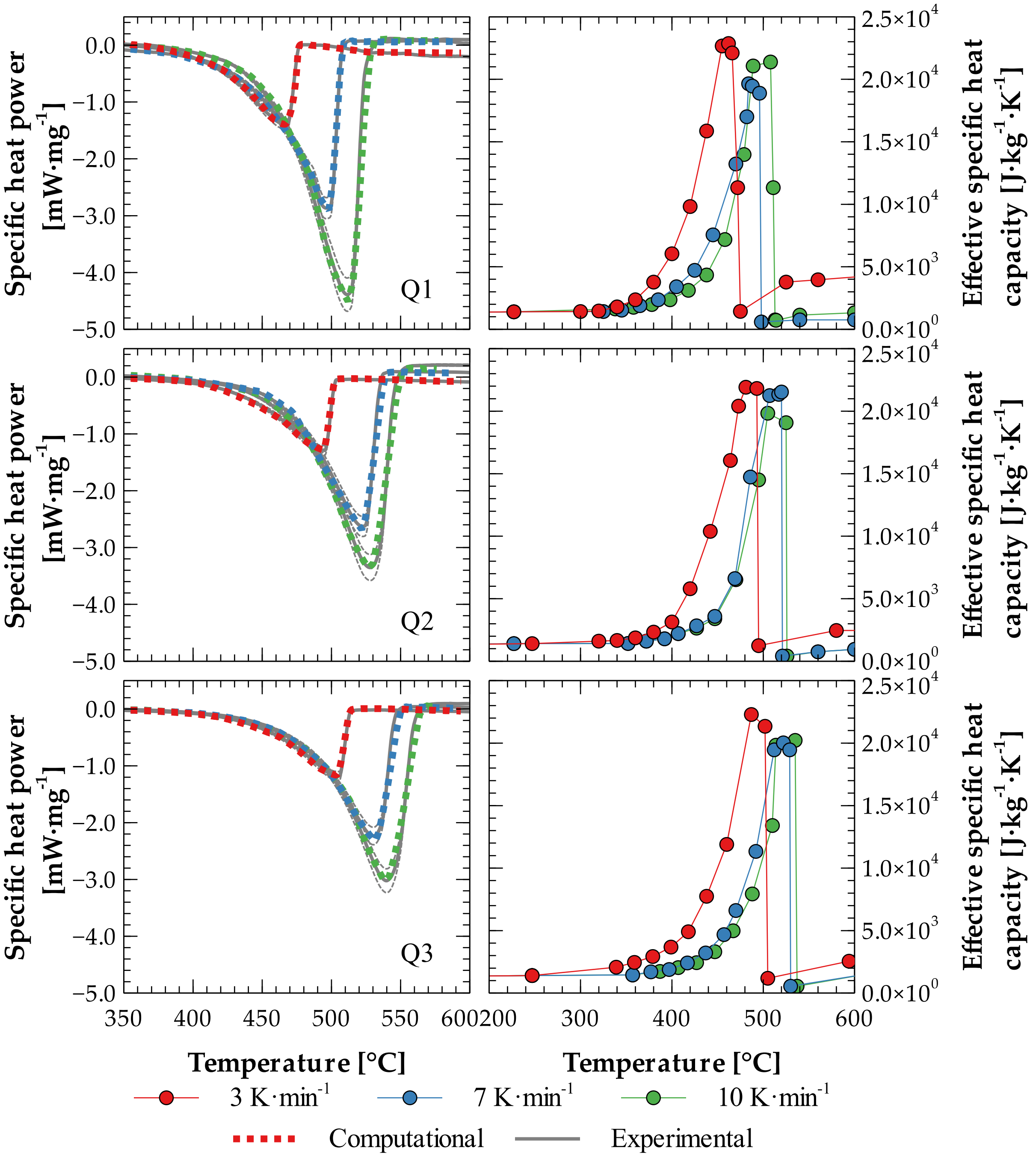

***Figure 5.12.*** *Comparison of experimental and computational DSC data and corresponding effective specific heat capacity vs. temperature functions.*

Principal numerical data on the effective specific heat capacity are summarized in Tab. 5.3. The specific enthalpy showed in the table was calculated as

$$\int_{T_1}^{T_2} c_{eff}\,\mathrm{d}T = H, \tag{5.4}$$

where $T_1$ and $T_2$ [K] are temperatures corresponding to the beginning and end of the decomposition process.

***Table 5.3.*** *Numerical data on effective specific heat capacity and specific enthalpy of lime hydrate decomposition process.*

| Heating rate [K·min$^{-1}$] | Peak top [J·kg$^{-1}$·K$^{-1}$] | | | Peak top temperature [°C] | | | Specific enthalpy [J·g$^{-1}$] | | |
|---|---|---|---|---|---|---|---|---|---|
| | Q1 | Q2 | Q3 | Q1 | Q2 | Q3 | Q1 | Q2 | Q3 |
| 3 | 22480 | 21866 | 21818 | 464 | 487 | 495 | 1588 | 1588 | 1709 |
| 7 | 19551 | 21378 | 20024 | 486 | 514 | 521 | 1371 | 1454 | 1464 |
| 10 | 21222 | 19457 | 20023 | 498 | 515 | 524 | 1526 | 1436 | 1443 |

Although the computational outputs (Tab. 5.3) were more consistent than those obtained experimentally (Fig. 5.11), they still suffered some inconsistencies as, in accordance with the error theory, all measurement errors could not be filtered out even by the detailed computational analysis. Being not able to be included in the model, an insufficient contact of the crucible with the DSC rod, slight mass variations or shape deformations of the crucibles, deviations in sample compression or sample position in the crucible belonged among the most significant sources of random errors affecting the results. The maximum effective specific heat capacity value reached 20869 J·kg$^{-1}$·K$^{-1}$ in average, differing by up to 1611 J·kg$^{-1}$·K$^{-1}$, which represented an acceptable maximum deviation of 7.7 %.

According to the results presented by Azpiazu et al. (2003) and Felderhoff et al. (2013), $Ca(OH)_2$ exhibits thermal decomposition between 510 and 527 °C. The kinetics of the reaction is though not unique as it depends on various factors, such as atmospheric pressure (Schaube et al., 2012), degree of crystallinity, surface area, temperature and relative humidity history of the sample (Beaudoin et al., 2006). For the lime hydrate analyzed in this paper, the results obtained for Q2 and Q3 samples and heating rates of 7 and 10 K·min$^{-1}$ showed the highest consistency and the highest agreement with other researchers, having the peak top temperatures between 514 and 524 °C and specific enthalpy between 1436 and 1464 J·g$^{-1}$. The corresponding effective specific heat capacity vs. temperature curve is shown in Fig. 5.13. It was constructed using a spline approximation of curve segments.

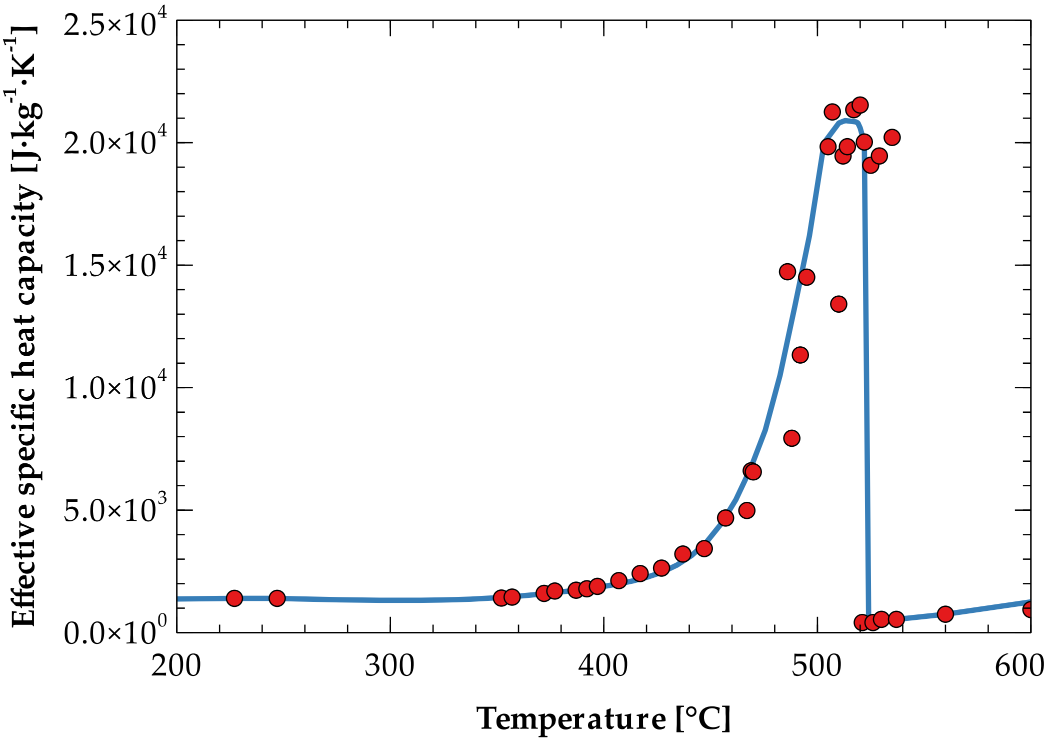

***Figure 5.13.*** *Effective specific heat capacity of* $Ca(OH)_2$ *decomposition process calculated for the most appropriate experimental setup.*

### 5.2.3.3 Correction of inaccuracies in experimental data

The effective specific heat capacity vs. temperature function determined in Section 5.2.3.2 (see Fig. 5.13) was used to calculate corrected specific heat power curves for each experimental setup. Contrary to the experimental data based on temperatures recorded on the thermocouples placed outside the crucibles, the computational outputs were obtained using temperatures in the sample, i.e., the computational model provided data adjusted for the signal delay.

Fig. 5.14 shows that the corrected specific heat power values were higher than those obtained experimentally which could be attributed to internal heat capacity of inner parts of the device that consumed a part of heat. The higher the heating rate was, the higher was the specific heat power difference, reaching up to 0.38 $mW \cdot mg^{-1}$ (~9 %). However, higher sample mass significantly reduced these systematic errors which could be demonstrated on a comparison of Q1 and Q3 related results. The signal delay was most significant in case of small sample mass and low heating rate. The best agreement of experimental and computational results was achieved for Q2 and 7 $K \cdot min^{-1}$ when the temperature shift at the peak top was 4.9 °C and the specific heat power difference of only 0.09 $mW \cdot mg^{-1}$ (3.4 %) was observed. Compared to the results obtained for other experimental setups, which showed temperature shifts up to 52.0 °C and specific heat power difference up to 0.38 mW·mg-1, such small differences can be ascribed to reduction of systematic errors by up to 76.95% in case of the temperature shift and 90.59% in case of the specific heat power, respectively.

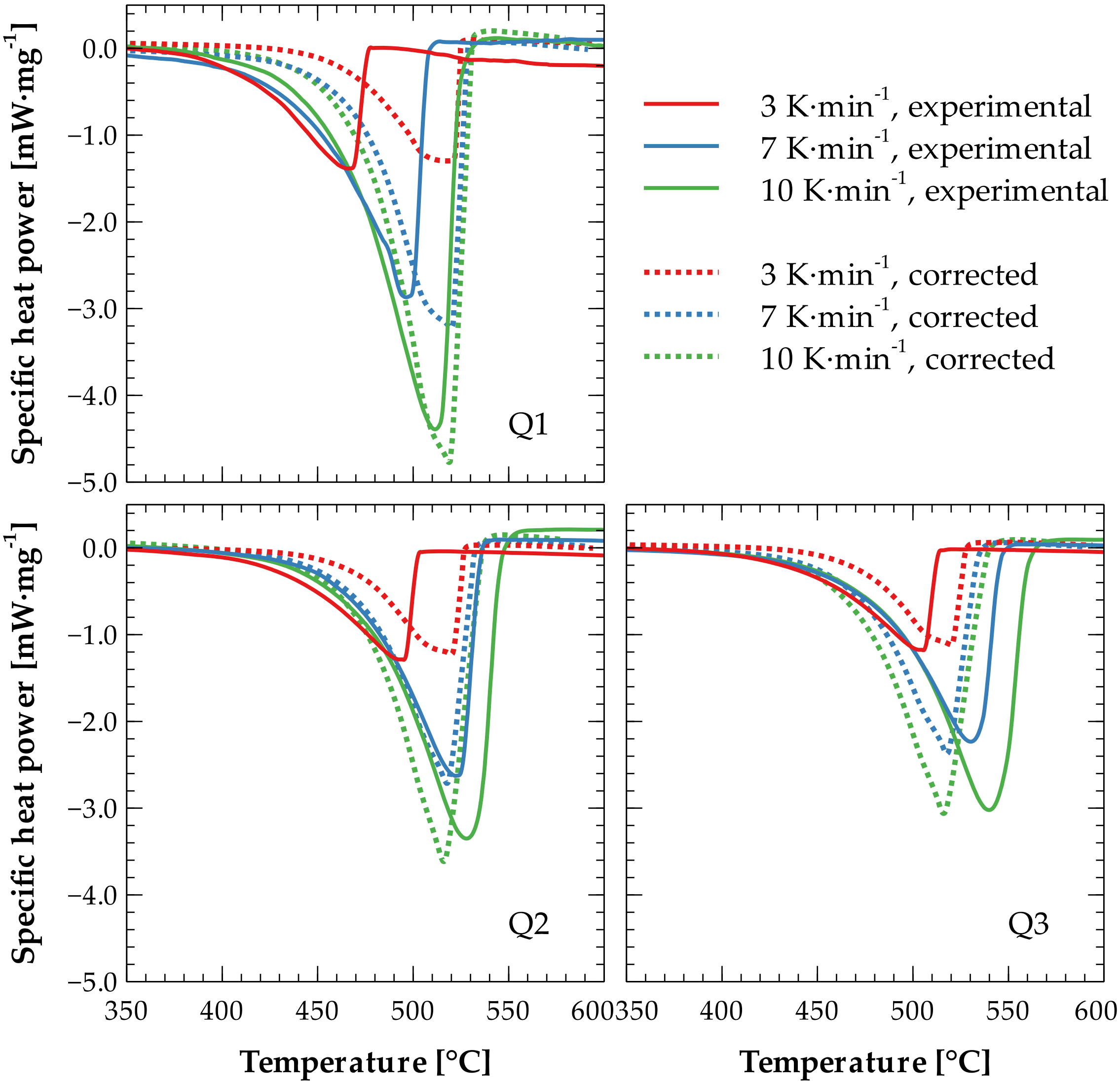

***Figure 5.14.*** *Computational corrections of experimental outputs: solid lines – experimental outputs, dotted lines – corrected outputs.*

# 6 Conclusions

The presented thesis aimed at the investigation of thermal processes in calorimetric experiments in order to eliminate systematic errors that may accompany the measurements. In the introduction, the basic history of calorimetry and types of calorimeters were presented, being followed by a summary of drawbacks that can be assumed as origins of measurement errors. An overview on elimination of these drawbacks was outlined and a computational technique was suggested as the main objective of thesis, that can efficiently eliminate or, at least, reduce the known disadvantages of the calorimetric technique.

For the sake of the demonstration, two types of calorimeters were selected: an isothermal heat flow calorimeter (IC) and a differential scanning calorimeter (DSC). The devices were described in detail including specifics and shortages that go along with the measurements.

A construction of computational representations of particular devices, their calibration and validation was then performed as the first step towards the elimination of the systematic measurements errors. The IC model was constructed as a three dimensional and consisted of 70883 nodes and 366544 finite elements. The model calibration and validation procedures were designed in the form of a complex scheme including a combination of experimental and computational calibration techniques and a validation approach based on using an independent heat power function. The comparison of experimental and computational outputs showed an outstanding level of agreement, $R^2 = 0.9998$, which indicated substantial advantages of the applied modeling approach over the commonly used mathematical corrections of experimental outputs of isothermal calorimeters.

In the calibration process of the DSC model, five standard metals with well-known heat transport and storage properties were used, similarly to the experimental calibration procedure. The standards underwent a melting process while a corresponding heat power was recorded and calculated. Equaling the particular outputs with the reference values, experimental and computational calibration curves were determined as functions of temperature. After the calibration, the accuracy was within the range of 0.1 % to 16 % and the computational model showed a very good agreement with the experimental outputs ($R^2 > 0.999794$). At the model validation procedure, two different materials were used. The analysis of melting of aluminum, as one of the standards which was not used at the calibration, showed that the computational output satisfactorily agreed with the experimental one. The highest difference, 0.279 $\mathrm{mW{\cdot}mg^{-1}}$ at the peak top, was well within the accuracy limits. The investigations of the effective specific heat capacity of quartz, as a representative of commonly studied materials which are though not standardized for DSC experiments, including its $\alpha$-$\beta$ transition revealed a good agreement between the experimental and computational results. The obtained values of effective specific heat capacity and specific enthalpy agreed well also with the results of independent experiments reported by several other researchers. The developed computational model could thus be considered well-calibrated and prepared for practical applications.

The main contribution of the thesis is presented in the last section, demonstrating capabilities of the computational models developed. The IC model was used for the assessment of fast heat evolving processes, making possible to reconstruct experimental results which can face problems of signal distortion and delay, or heat consumption, particularly in the very early stage of a measurement. The proposed technique utilized an inverse analysis of the transient heat transport processes in the computational representation of the calorimeter-sample system. In this way, the applied approach made it possible to identify what had happened inside the calorimeter that produced the particular experimental outputs (affected by the internal heat inertia). The calculated heat power function (the ideal state without heat inertia) was thus not affected by the intrinsic insufficiencies of the experimental technique. The practical application of the method was demonstrated for two characteristic cases of fast heat evolution. In the lime hydrate-water system the large-volume calorimetric experiment provided the peak heat power value of 0.64 $\mathrm{mW{\cdot}g^{-1}}$ at 2760 s, while the computational technique identified the maximum heat power of 4.45 $\mathrm{mW{\cdot}g^{-1}}$ at 120 s. In the Portland cement-water system the experimental initial heat power peak of 2.3 $\mathrm{mW{\cdot}g^{-1}}$ was observed at 1680 s but the calculated value (without the effects of thermal inertia) was 27.6 $\mathrm{mW{\cdot}g^{-1}}$ at 120 s. The computational model was able to reconstruct well the original experimental data, with $R^2 = 0.9984$ for the lime hydrate-water system and $R^2 = 0.9992$ for the Portland cement-water system. The combination of uncertainty analysis of experimental measurements and sensitivity analysis of computer simulated data showed that in both cases the sensitivity range of computational results covered well the experimental outputs over the whole studied time period and, similarly, the computational outputs were within the uncertainty range of experimental data. The proposed computational technique offered, at the same time, the advantages of the large volume isothermal calorimetry and the high time resolution typical for small-volume calorimetric measurements, which is a unique combination. Therefore, it has a good potential for future applications in physics, chemistry, and engineering.

Finally, the DSC model was used for a detailed modeling of thermal phenomena in the calorimeter-sample system to correct inaccuracies in DSC measurements caused by intrinsic factors given by the construction limits of DSC devices. The applied model took into account the position of thermocouples outside the sample, neglected heat capacity of the sample and inner parts of the device, or incomprehensive experimental procedure that did not involve the sample mass. Therefore, its outputs were supposed to be independent on externalities, such as heating rate or sample size. In a practical application of the method, thermal decomposition of commercially produced lime hydrate, $Ca(OH)_2$, was analyzed. Three different sample masses (11.3 mg (Q1), 26.5 mg (Q2), and 41.6 mg (Q3)) and three different heating rates (3 $K·min^{-1}$, 7 $K·min^{-1}$, and 10 $K·min^{-1}$) were selected as representative parameters of the experimental setup. The experimental outputs in the form of specific heat power vs. temperature curves were fitted computationally by means of seeking the effective specific heat capacity of the material involved in the decomposition reaction. The specific enthalpy of decomposition calculated using the effective specific heat capacity presented then a reaction parameter independent on sample mass, heating rate, and other externalities. Based on the analysis of results obtained for $Ca(OH)_2$ decomposition by other investigators, the heating rates of 7 and 10 $K·min^{-1}$ in combination with sample masses Q2 and Q3 were identified as the most appropriate parameters of experimental setup. The computational data averaging provided then the peak top temperature between 514 and 524 °C and the specific enthalpy between 1436 and 1464 $J·g^{-1}$. Finally, the outputs adjusted for the signal delay were extracted from the results obtained using the computational model for particular experimental setups. The corrected specific heat power values were up to ~9 % higher than those obtained experimentally which was attributed to the internal heat capacity of inner parts of the device.

# References

Albrecht, T., Armbruster, S., Keller, S., Strobl, G., 2001. Dynamics of surface crystallization and melting in polyethylene and poly(ethylene oxide) studied by temperature-modulated DSC and heat wave spectroscopy. Macromolecules 34, 8456-8467.

Alhozaimy, A., Fares, G., Alawad, O.A., Al-Negheimish, A., 2015. Heat of hydration of concrete containing powdered scoria rock as a natural pozzolanic material. Construction and Building Materials 81, 113-119.

Alok, A., Das, M., 2019. Multi-objective optimization of cutting parameters during sustainable dry hard turning of AISI 52100 steel with newly develop HSN2-coated carbide insert, Measurement 133, 288-302.

Azpiazu, M.N., Morquillas, J.M., Vazquez, A., 2003. Heat recovery from a thermal energy storage based on the Ca(OH)(2)/CaO cycle. Applied Thermal Engineering 23(6), 733-741.

Barz, T., Sommer, A., 2018. Modeling hysteresis in the phase transition of industrial-grade solid/liquid PCM for thermal energy storages. International Journal of Heat and Mass Transfer 127, 701-713.

Bazinski, S.J., Wang, X., 2015. Experimental study on the influence of temperature and state-of-charge on the thermophysical properties of an LFP pouch cell. Journal of Power Sources 293, 283-291.

Beaudoin, J.J., Sato, T., Tumidajski, P.J., 2006. The Thermal decomposition of Ca(OH)2 polymorphs, 2nd International Symposium on Advances in Concrete Through Science and Engineering. RILEM, Québec City, Canada, pp. 1-15.

Benes, S., Kruis, J., 2015. Efficient methods to visualize finite element meshes. Advances in Engineering Software 79, 81-90.

Bensted, J., 1987. Some applications of conduction calorimetry to cement hydration. Advances in Cement Research 1, 35-44.

Bohac, M., Palou, M., Novotny, R., Masilko, J., Soukal, F., Opravil, T., 2017. Influence of temperature on early hydration of Portland cement-metakaolin-slag system. Journal of Thermal Analysis and Calorimetry 127(1), 309-318.

Brutting, M., Hemberger, F., Vidi, S., Wachtel, J., Mehling, H., Ebert, H.P., 2016. Determination of heat capacity by means of longitudinal guarded comparative calorimeter - Correction methods, International Journal of Thermal Sciences 100, 423-429.

Buchholz, A.C., Schoeller, D.A., 2004. Is a calorie a calorie? The American Journal of Clinical Nutrition 79(5), 899S-906S.

Calvet, E., Prat, H., 1963. Recent Progress in Microcalorimetry. Pergamon Press, London.

Carpenter, K., Janssens, M., 2005. Using heat release rate to assess combustibility of building products in the cone calorimeter. Fire Technology 41(2), 79-92.

Černý, R., Rovnaníková, P., 2002. Transport Processes in Concrete. Spon Press, London.

David, D., Johannes, K., Kuznik, F., 2017. Quantification of the natural convection perturbations on differential scanning calorimetry measurements of PCMs. Thermochimica Acta 655, 145-154.

Dumas, J.-P., Gibout, S., Zalewski, L., Johannes, K., Franquet, E., Lassue, S., Bedecarrats, J.-P., Tittelein, P., Kuznik, F., 2014. Interpretation of calorimetry experiments to characterise phase. change materials. International Journal of Thermal Sciences 78, 48-55.

Duong Dinh, N., Devlin, L.P., Koshy, P., Sorrell, C.C., 2016. Effects of acetic acid on early hydration of Portland cement. Journal of Thermal Analysis and Calorimetry 123(1), 489-499.

Emsley, J., 1998. The elements, 3rd edition ed. Oxford Press, Oxford.

Evju, C., 2003. Initial hydration of cementitious systems using a simple isothermal calorimeter and dynamic correction. Journal of Thermal Analysis and Calorimetry 71(3), 829-840.

Felderhoff, M., Urbanczyk, R., Peil, S., 2013. Thermochemical Heat Storage for High Temperature Applications – A Review, Green. p. 113.

Gao, W.Y., Wang, Y.W., Dong, L.M., Yu, Z.W., 2006. Thermokinetic analysis of the hydration process of calcium phosphate cement. Journal of Thermal Analysis and Calorimetry 85(3), 785-789.

Garcia-Cuello, V., Moreno-Pirajan, J.C., Giraldo-Gutierrez, L., Sapag, K., Zgrablich, G., 2009. Adsorption micro calorimeter. Journal of Thermal Analysis and Calorimetry 97(2), 711-715.

Ghiorso, M.S., Carmichael, I.S.E., Moret, L.K., 1979. Inverted high-temperature quartz - unit-cell parameters and properties of the alpha-beta inversion. Contributions to Mineralogy and Petrology 68(3), 307-323.

Grant, S.A., 2003. Extension of a temperature effects model for capillary pressure saturation relations. Water Resources Research 39(1).

Gu, Y., Ran, Q., Shu, X., Yu, C., Chang, H., Liu, J., 2016. Synthesis of nanoSiO(2)@PCE core-shell nanoparticles and its effect on cement hydration at early age. Construction and Building Materials 114, 673-680.

Hajra, R.N., Tripathy, H.P., Rai, A.K., Vijayashanthi, N., Raju, S., Saroja, S., 2017. Study of high temperature phase stability and phase transformation kinetics of sigma and parent alpha phase in Fe55Cr45 (wt. %) alloy. Journal of Alloys and Compounds 727, 940-947.

Haloua, F., Ponsard, J.-N., Lartigue, G., Hay, B., Villermaux, C., Foulon, E., Zarea, M., 2012. Thermal behaviour modelling of a reference calorimeter for natural gas. International Journal of Thermal Sciences 55, 40-47.

Han, F., Wang, Q., Liu, M., Mei, Y., 2016. Early hydration properties of composite binder containing limestone powder with different finenesses. Journal of Thermal Analysis and Calorimetry 123(2), 1141-1151.

Hasan, A., McCormack, S.J., Huang, M.J., Norton, B., 2014. Characterization of phase change materials for thermal control of photovoltaics using Differential Scanning Calorimetry and Temperature History Method. Energy Conv. Manag. 81, 322-329.

Hemingway, B.S., 1987. Quartz - heat-capacities from 340-K to 1000-K and revised values for the thermodynamic properties. American Mineralogist 72(3-4), 273-279.

Holland, J.H., 1962. Outline for a logical theory of adaptive systems. Journal of the ACM 9(3), 297-+.

Holm, J.L., Kleppa, O.J., Westrum, E.F., 1967. Thermodynamics of polymorphic transformations in silica - thermal properties from 5 to 1070 degress K and pressure - temperature stability fields for coesite and stishovite. Geochimica Et Cosmochimica Acta 31(12), 2289-&.

Huo, J.H., Peng, Z.G., Feng, Q., Zheng, Y., Liu, X.J., 2018. Controlling the heat evaluation of cement slurry system used in natural gas hydrate layer by micro-encapsulated phase change materials. Sol. Energy 169, 84-93.

Chase, M.W., 1998. NIST-JANAF Thermochemical Tables. American Chemical Society and American Institute of Physics for National Institute of Standards and Technology, Woodbury, New York.

Choinski, D., Wodolazski, A., Skupin, P., Stachanczyk, D., Niedzwiedz, M., 2016. Analysis of the thermal properties of a heat flow chip calorimeter using CFD. Applied Thermal Engineering 96, 508-518.

Delroisse, H., Plantier, F., Marlin, L., Dicharry, C., Froute, L., Andre, R., Torre, J.P., 2018. Determination of thermophysical properties of cyclopentane hydrate using a stirred calorimetric cell. Journal of Chemical Thermodynamics 125, 136-141.

ISO/EIC 98-3, 2008. Guide to the Expression of Uncertainty in Measurement. Joint Comittee for Guides in Metrology, France.

Jansen, D., Goetz-Neunhoeffer, F., Lothenbach, B., Neubauer, J., 2012. The early hydration of Ordinary Portland Cement (OPC): An approach comparing measured heat flow with calculated heat flow from QXRD. Cement and Concrete Research 42(1), 134-138.

Jansen, D., Spies, A., Neubauer, J., Ectors, D., Goetz-Neunhoeffer, F., 2017. Studies on the early hydration of two modifications of ye'elimite with gypsum. Cement and Concrete Research 91, 106-116.

Javdanitehran, M., Berg, D.C., Duemichen, E., Ziegmann, G., 2016. An iterative approach for isothermal curing kinetics modelling of an epoxy resin system. Thermochimica Acta 623, 72-79.

Jerman, M., Tydlitat, V., Keppert, M., Cachova, M., Cerny, R., 2016. Characterization of early-age hydration processes in lime-ceramic binders using isothermal calorimetry, X-ray diffraction and scanning electron microscopy. Thermochimica Acta 633, 108-115.

Kaye&Laby Online, 2005. Tables of Physical and Chemical Constants, Thermal Conductivities. http://www.kayelaby.npl.co.uk/general_physics/2_3/2_3_7.html. (Accessed June 5 2018).

Klemczak, B., Batog, M., 2016. Heat of hydration of low-clinker cements. Journal of Thermal Analysis and Calorimetry 123(2), 1351-1360.

Koci, J., Madera, J., Cerny, R., 2016a. A Laboratory Experiment for Monitoring the Time Development of Water Freezing Processes in Porous Materials and Its Computational Analysis. Int. J. Thermophys. 37(12), 11.

Koci, J., Madera, J., Jerman, M., Keppert, M., Svora, P., Cerny, R., 2016b. Identification of Water Diffusivity of Inorganic Porous Materials Using Evolutionary Algorithms. Transport in Porous Media 113(1), 51-66.

Koci, V., Madera, J., Jerman, M., Cerny, R., 2017. Computational analysis of heat transport and storage processes in large-volume isothermal heat flow calorimeter. Applied Thermal Engineering 121, 547-553.

Kong, F.-r., Pan, L.-s., Wang, C.-m., Zhang, D.-l., Xu, N., 2016. Effects of polycarboxylate superplasticizers with different molecular structure on the hydration behavior of cement paste. Construction and Building Materials 105, 545-553.

Krabbenhoft, K., Damkilde, L., Nazem, M., 2007. An implicit mixed enthalpy-temperature method for phase-change problems. Heat Mass Transf. 43(3), 233-241.

Kruis, J., Koudelka, T., Krejci, T., 2010. Efficient computer implementation of coupled hydro-thermo-mechanical analysis. Mathematics and Computers in Simulation 80(8), 1578-1588.

Kuznik, F., David, D., Johannes, K., Roux, J.J., 2011. A review on phase change materials integrated in building walls. Renew. Sust. Energ. Rev. 15(1), 379-391.

Lager, D., Hohenauer, W., Knoll, C., Weinberger, P., Werner, A., 2018. Methodology to determine the apparent specific heat capacity of metal hydroxides for thermochemical energy storage. Journal of Thermal Analysis and Calorimetry 133(1), 207-215.

Laidler, K.J., 1995. The world of physical chemistry. Oxford University Press, Oxford.

Lander, J.J., 1951. Experimental heat contents of SrO, BaO, CaO, BaCO3 and SrCO3 at high temperatures – dissociation pressures of BaCO3 and SrCO3. Journal of the American Chemical Society 73, 5794-5797.

LGC, 2014. LGC Produced Reference Materials Catalogue. Laboratory of the Governement Chemist, Middlesex, UK.

Liu, L., Yang, P., Qi, C.C., Zhang, B., Guo, L.J., Song, K.I., 2019. An experimental study on the early-age hydration kinetics of cemented paste backfill. Construction and Building Materials 212, 283-294.

Madej, D., Ortmann, C., Szczerba, J., Jacewicz, M., 2016. Calorimetry and other methods in the studies of reactive magnesia-hydratable alumina-microsilica hydrating mixtures. Journal of Thermal Analysis and Calorimetry 126(3), 1133-1142.

Madera, J., Koci, J., Koci, V., Kruis, J., 2017. Parallel modeling of hygrothermal performance of external wall made of highly perforated bricks. Advances in Engineering Software 113, 47-53.

Maheswaran, S., Kalaiselvam, S., Palani, G.S., Sasmal, S., 2016. Investigations on the early hydration properties of synthesized beta-belites blended cement pastes. Journal of Thermal Analysis and Calorimetry 125(1), 53-64.

Mandilaras, I.D., Kontogeorgos, D.A., Founti, M.A., 2015. A hybrid methodology for the determination of the effective heat capacity of PCM enhanced building components. Renew. Energy 76, 790-804.

Marison, I., Linder, M., Schenker, B., 1998. High-sensitive heat-flow calorimetry1Presented at the Twelfth Ulm-Freiberg Conference, Freiberg, Germany, 19–21 March 19971. Thermochimica Acta 310(1), 43-46.

Medina, C., Saez del Bosque, I.F., Asensio, E., Frias, M., Sanchez de Rojas, M.I., 2016. New additions for eco-efficient cement design. Impact on calorimetric behaviour and comparison of test methods. Materials and Structures 49(11), 4595-4607.

Medved, I., Trnik, A., Vozar, L., 2017. Modeling of heat capacity peaks and enthalpy jumps of phase-change materials used for thermal energy storage. International Journal of Heat and Mass Transfer 107, 123-132.

Mehta, P.K., Monteiro, P.J.M., 2006. Concrete: microstructure, properties, and materials. McGraw-Hill, New York.

Modest, M.F., 2000. Radiative heat transfer. McGraw-Hill, New York.

Moon, H., Ramanathan, S., Suraneni, P., Shon, C.S., Lee, C.J., Chung, C.W., 2018. Revisiting the Effect of Slag in Reducing Heat of Hydration in Concrete in Comparison to Other Supplementary Cementitious Materials. Materials 11(10), 17.

Moser, H., 1936. Messung der wahren spezifischen Wärme von Silber, Nickel, β - Messing, Quartzkristall and Quartzglas zwischen +50 und 700 °C nach einer verfeinerten Methode. Physikalische Zeitschrift 37, 737-753.

NIST, 2013. Standard Reference Materials Technical Catalog. National Institute of Standards and Technology, Galthersburg, MD, USA.

Overdeep, K.R., Weihs, T.P., 2015. Design and functionality of a high-sensitivity bomb calorimeter specialized for reactive metallic foils. Journal of Thermal Analysis and Calorimetry 122(2), 787-794.

Posern, K., Kaps, C., 2008. Humidity controlled calorimetric investigation of the hydration of MgSO4 hydrates. Journal of Thermal Analysis and Calorimetry 92(3), 905-909.

Powell, R., Ho, C.Y., Lilly, P.E., 1966. Thermal Conductivity of Selected Materials. US Government Printing Office, Washington, DC.

Rahhal, V., Talero, R., 2005. Early hydration of portland cement with crystalline mineral additions. Cement and Concrete Research 35(7), 1285-1291.

Randzio, S., Suurkuusk, J., 1980. Interpretation of Calorimetric Thermograms and their Dynamic Corrections in Biological Microcalorimetry. Academic Press, London.

Riding, K.A., Poole, J.L., Schindler, A.K., Juenger, M.C.G., Folliard, K.J., 2006. Evaluation of temperature prediction methods for mass concrete members. Aci Materials Journal 103(5), 357-365.

Richardson, M.J., Charsley, E.L., 1998. Chapter 13 - Calibration and Standardisation in DSC, in: Brown, M.E. (Ed.) Handbook of Thermal Analysis and Calorimetry. Elsevier Science B.V., Amsterdam, pp. 547-575.

Richet, P., Bottinga, Y., Denielou, L., Petitet, J.P., Tequi, C., 1982. Thermodynamic properties of quartz, cristobalite and amorphous SiO2 - drop calorimetry measurements between 1000-K and 1800-K and a review from 0-K to 2000-K. Geochimica Et Cosmochimica Acta 46(12), 2639-2658.

Roth, W.A., Bertram, W., 1929. Messung des spezifischen Wärmen von metallurgish wichtigen Stoffen in einem grösseren Temperaturintervall mit Hilfe von zwei neuen Calorimetertypen. Zeitschrift für Elektrochemie 35, 297-308.

Saeed, M.K., Rahman, M.K., Baluch, M.H., 2016. Early age thermal cracking of mass concrete blocks with Portland cement and ground granulated blast-furnace slag. Magazine of Concrete Research 68(13), CP3-663.

Saeed, R.M., Schlegel, J.P., Castano, P., Sawafta, R., 2016. Uncertainty of Thermal Characterization of Phase Change Material by Differential Scanning Calorimetry Analysis. International Journal of Engineering Research & Technology 5(1), 405-412.

Sarge, S.M., Gmelin, E., Hohne, G.W.H., Cammenga, H.K., Hemminger, W., Eysel, W., 1994. The caloric calibration of scanning calorimeters. Thermochimica Acta 247(2), 129-168.

Sari, A., Karaipekli, A., 2008. Preparation and thermal properties of capric acid/palmitic acid eutectic mixture as a phase change energy storage material. Mater. Lett. 62(6-7), 903-906.

Sarier, N., Onder, E., 2007. Thermal characteristics of polyurethane foams incorporated with phase change materials. Thermochimica Acta 454(2), 90-98.

Scrivener, K.L., Juilland, P., Monteiro, P.J.M., 2015. Advances in understanding hydration of Portland cement. Cement and Concrete Research 78, 38-56.

Sen, M.A., Kowalski, G.J., Fiering, J., Larson, D., 2015. A continuous flow microfluidic calorimeter: 3-D numerical modeling with aqueous reactants. Thermochimica Acta 603, 184-196.

Shakhtin, D.M., Pechenezhskii, V.I., Karaulov, A.G., Kvasman, N.M., Kravchenko, V.P., Kabakova, II, Ustichenko, V.A., Kalita, G.E., Shcherbenko, G.N., Yakobchuk, L.M., 1982. Thermal-conductivity of corundum, high-alumina, magnesia, zirconium, and chromate refractories in the 400-1800-degrees-C range. Refractories 23(5-6), 223-227.

Shi, C., Krivenko, P.V., Roy, D., 2006. Alkali-Activated Cements and Concretes. Taylor & Francis, London.

Schaube, F., Koch, L., Worner, A., Muller-Steinhagen, H., 2012. A thermodynamic and kinetic study of the de- and rehydration of Ca(OH)(2) at high H2O partial pressures for thermo-chemical heat storage. Thermochimica Acta 538, 9-20.

Schmidt, M., Szczukowski, C., Rosskopf, C., Linder, M., Worner, A., 2014. Experimental results of a 10 kW high temperature thermochemical storage reactor based on calcium hydroxide. Applied Thermal Engineering 62, 553-559.

Sinelnikov, N.N., 1953. Vakuumnyi adiabaticheskii kalorimetr i nekotorye novye dannye o beta-reversible-alpha-prevrashchenii kvartsa. Doklady Akademii Nauk Sssr 92(2), 369-372.

Snelson, D.G., Wild, S., O'Farrell, M., 2008. Heat of hydration of Portland Cement-Metakaolin-Fly ash (PC-MK-PFA) blends. Cement and Concrete Research 38(6), 832-840.

Sundararajan, S., Samui, A.B., Kulkarni, P.S., 2018. Synthesis and characterization of poly(ethylene glycol) acrylate (PEGA) copolymers for application as polymeric phase change materials (PCMs). Reactive & Functional Polymers 130, 43-50.

Tyagi, V.V., Buddhi, D., 2008. Thermal cycle testing of calcium chloride hexahydrate as a possible PCM for latent heat storage. Sol. Energy Mater. Sol. Cells 92(8), 891-899.

Tydlitat, V., Medved, I., Cerny, R., 2012a. Determination of a partial phase composition in calcined gypsum by calorimetric analysis of hydration kinetics. Journal of Thermal Analysis and Calorimetry 109(1), 57-62.

Tydlitat, V., Tesarek, P., Cerny, R., 2008. Effects of the type of calorimeter and the use of plasticizers and hydrophobizers on the measured hydration heat development of FGD gypsum. Journal of Thermal Analysis and Calorimetry 91(3), 791-796.

Tydlitat, V., Zakoutsky, J., Cerny, R., 2012b. An isothermal heat flow calorimeter for large-volume applications. Journal of Thermal Analysis and Calorimetry 110(2), 1021-1027.

Ubelhor, R., Ellison, D., Pierce, C., 2015. Enhanced thermal property measurement of a silver zinc battery cell using isothermal calorimetry. Thermochimica Acta 606, 77-83.

Velez, C., de Zarate, J.M.O., Khayet, M., 2015. Thermal properties of n-pentadecane, n-heptadecane and n-nonadecane in the solid/liquid phase change region, International Journal of Thermal Sciences 94, 139-146.

White, W.P., 1919. Silicate specific heats, second series. American Journal of Science 47, 1-43.

Wietzel, R., 1921. De Stabilitätsverhältnisse der Glasand Kristallphase des Siliziudioxydes. Zeitschrift für Anorganische und Allgemeine Chemie 116, 71-95.

Xi, Y., 2006. A discussion on causes and mechanism of paste flash setting.

Xu, Q., Wang, K., Medina, C., Engquist, B., 2015. A mathematical model to predict adiabatic temperatures from isothermal heat evolutions with validation for cementitious materials. International Journal of Heat and Mass Transfer 89, 333-338.

Yamane, T., Katayama, S., Todoki, M., 1991. Application of a deconvolution method to kinetic-studies with conduction type microcalorimeters. Thermochimica Acta 183, 329-338.

Zelic, J., Rusic, D., Krstulovic, R., 2002. Kinetic analysis of thermal decomposition of Ca(OH)(2) formed during hydration of commercial Portland cement by DSC. Journal of Thermal Analysis and Calorimetry 67, 613-622.

Zhang, Y.P., Jiang, Y., Jiang, Y., 1999. A simple method, the T-history method, of determining the heat of fusion, specific heat and thermal conductivity of phase-change materials. Measurement Science and Technology 10, 201-205.

# List of Author's Publications

## WoS journal papers

Delgado, J.M.P.Q., Guimaraes, A.S., de Freitas, V.P., Antepara, I., Kočí, V., Černý, R., 2016. Salt Damage and Rising Damp Treatment in Building Structures. Advances in Materials Science and Engineering 2016, Art. ID 1280894.

Jerman, M., Palomar, I., Kočí, V., Černý, R., 2019. Thermal and hygric properties of biomaterials suitable for interior thermal insulation systems in historical and traditional buildings. Building and Environment 154, 81-88.

Kočí, V., Maděra, J., Černý, R., 2012. Exterior thermal insulation systems for AAC building envelopes: Computational analysis aimed at increasing service life. Energy and Buildings 47, 84-90.

Kočí, V., Maděra, J., Černý, R., 2013. Computer aided design of interior thermal insulation system suitable for autoclaved aerated concrete structures. Applied Thermal Engineering 58(1-2), 165-172.

Kočí, V., Bažantová, Z., Černý, R., 2014. Computational analysis of thermal performance of a passive family house built of hollow clay bricks. Energy and Buildings 76, 211-218.

Kočí, V., Maděra, J., Fořt, J., Žumár, J., Pavlíková, M., Pavlík, Z., Černý, R., 2014. Service Life Assessment of Historical Building Envelopes Constructed Using Different Types of Sandstone: A Computational Analysis Based on Experimental Input Data. Scientific World Journal.

Kočí, V., Maděra, J., Jerman, M., Trník, A., Černý, R., 2014. Determination of the equivalent thermal conductivity of complex material systems with large-scale heterogeneities. International Journal of Thermal Sciences 86, 365-373.

Kočí, V., Kočí, J., Korecky, T., Maděra, J., Černý, R., 2015. Determination of Radiative Heat Transfer Coefficient at High Temperatures Using a Combined Experimental-Computational Technique. Measurement Science Review 15(2), 85-91.

Kočí, V., Kočí, J., Čáchová, M., Vejmelková, E., Černý, R., 2016. Multi-parameter optimization of lime composite design using a modified downhill simplex method. Composites Part B-Engineering 93, 184-189.

Kočí, V., Kočí, J., Maděra, J., Černý, R., 2016. Contribution of waste products in single-layer ceramic building envelopes to overall energy savings. Energy 111, 947-955.

Kočí, V., Maděra, J., Jerman, M., Žumár, J., Koňáková, D., Čáchová, M., Vejmelková, E., Reiterman, P., Černý, R., 2016. Application of waste ceramic dust as a ready-to-use replacement of cement in lime-cement plasters: an environmental-friendly and energy-efficient solution. Clean Technologies and Environmental Policy 18(6), 1725-1733.

Kočí, V., Kočí, J., Maděra, J., Černý, R., 2017. Assessment of fast heat evolving processes using inverse analysis of calorimetric data. International Journal of Heat and Mass Transfer 115, 831-838.

Kočí, V., Maděra, J., Jerman, M., Černý, R., 2017. Computational analysis of heat transport and storage processes in large-volume isothermal heat flow calorimeter. Applied Thermal Engineering 121, 547-553.

Kočí, V., Čáchová, M., Koňáková, D., Vejmelková, E., Jerman, M., Keppert, M., Maděra, J., Černý, R., 2018. Heat and Moisture Transport and Storage Parameters of Bricks Affected by the Environment. International Journal of Thermophysics 39(5).

Kočí, V., Kočí, J., Maděra, J., Pavlík, Z., Gu, X., Zhang, W., Černý, R., 2018. Thermal and hygric assessment of an inside-insulated brick wall: 2D critical experiment and computational analysis. Journal of Building Physics 41(6), 497-520.

Kočí, V., Maděra, J., Jerman, M., Černý, R., 2018. Experimental Determination of Frost Resistance of Autoclaved Aerated Concrete at Different Levels of Moisture Saturation. International Journal of Thermophysics 39(6).

Kočí, J., Kočí, V., Černý, R., 2019. A Method for Rapid Evaluation of Thermal Performance of Wall Assemblies Based on Geographical Location. Energies 12(7).

Kočí, J., Kočí, V., Maděra, J., Černý, R., 2019. Effect of applied weather data sets in simulation of building energy demands: Comparison of design years with recent weather data. Renewable & Sustainable Energy Reviews 100, 22-32.

Kočí, V., Maděra, J., Krejčí, T., Kruis, J., Černý, R., 2019. Efficient Techniques for Solution of Complex Computational Tasks in Building Physics. Advances in Civil Engineering 2019.

Kočí, V., Maděra, J., Trník, A., Černý, R., 2019. Heat transport and storage processes in differential scanning calorimeter: Computational analysis and model validation. International Journal of Heat and Mass Transfer 136, 355-364.

Kočí, V., Kočí, J., Maděra, J., Žák, J., Černý, R., 2020. Computational Prediction of Susceptibility to Biofilms Growth: Two-Dimensional Analysis of Critical Construction Details. Energies 13, Article No. 293.

Kočí, V., Petříková M., Fořt, J., Fiala, L., Černý, R., 2020. Preparation of self-heating alkali-activated materials using industrial waste products. Journal of Cleaner Production 260, Article No. 121116.

Kočí, V., Fořt, J., Maděra, J., Scheinherrová, L., Trník, A., Černý, R., 2020. Correction of errors in DSC measurements using detailed modeling of thermal phenomena in calorimeter-sample system. IEEE Transactions on Instrumentation and Measurement 69, 8178-8186.

Kočí, V., Scheinherrová, L., Maděra, J., Keppert, M., Suchorab, Z., Lagód, G., Černý, R., 2020. Experimental and Computational Study of Thermal Processes in Red Clays Exposed to High Temperatures. Energies 13, Article No. 2211.

Kočí, V., Jerman, M., Pavlík, Z., Maděra, J., Žák, J., Černý, R., 2020. Interior thermal insulation systems based on wood fiberboards: experimental analysis and computational assessment of hygrothermal and energy performance in the Central European climate. Energy and Buildings 222, Article No. 110093.

Maděra, J., Kočí, J., Kočí, V., Kruis, J., 2017. Parallel modeling of hygrothermal performance of external wall made of highly perforated bricks. Advances in Engineering Software 113, 47-53.

Ondruška, J., Medveď, I., Kočí, V., Černý, R., 2016. Measurement of the contribution of radiation to the apparent thermal conductivity of fiber reinforced cement composites exposed to elevated temperatures. International Journal of Thermal Sciences 100, 298-304.

Pavlík, Z., Jerman, M., Trník, A., Kočí, V., Černý, R., 2014. Effective thermal conductivity of hollow bricks with cavities filled by air and expanded polystyrene. Journal of Building Physics 37(4), 436-448.

Suchorab, Z., Majerek, D., Kočí, V., Černý, R., 2020. Time Domain Reflectometry flat sensor for non-invasive monitoring of moisture changes in building materials. Measurement 165, Article No. 108091.

Vimmrová, A., Kočí, V., Krejsova, J., Černý, R., 2016. A Method for Optimizing Lightweight-Gypsum Design Based on Sequential Measurements of Physical Parameters. Measurement Science Review 16(3), 160-166.

### Book chapters

Černý, R., Kočí, V, 2015. Traditional fired-clay bricks versus large and highly perforated fired-clay bricks masonry: Influence on buildings thermal performance, Eco-efficient Masonry Bricks and Blocks. Woodhead Publishing, Abington Cambridge, pp. 63-81.